Geophysical Insights into the Histories of Venus, Mercury and the Moon

by

Peter Benjamin James

Sc.B., Brown University (2007)

Submitted to the Department of Earth, Atmospheric and Planetary Sciences
in partial fulfillment of the requirements for the degree of

Doctor of Philosophy in Planetary Science

at the

MASSACHUSETTS INSTITUTE OF TECHNOLOGY

February 2014

Author .....
Department of Earth, Atmospheric and Planetary Sciences
October 28, 2013

Certified by .....
Maria T. Zuber
E. A. Griswold Professor of Geophysics
Thesis Supervisor

Accepted by .....
Robert D. van der Hilst
Schlumberger Professor of Earth Sciences
Head, Department of Earth, Atmospheric and Planetary Sciences

Geophysical Insights into the Histories of Venus, Mercury and the Moon

by

Peter Benjamin James

Submitted to the Department of Earth, Atmospheric and Planetary Sciences
on October 28, 2013, in partial fulfillment of the
requirements for the degree of
Doctor of Philosophy in Planetary Science

Abstract

Gravity and topography data provide a powerful tool for studying the interiors of rocky planetary bodies. In this thesis I study three such bodies - Venus, Mercury and the Moon - and I use the gravity and topography data returned by recent NASA planetary science missions to model their structure and evolution. I calculate geoid/topography ratios on Venus using gravity and topography data from NASA's Magellan mission. These ratios inform models of crustal thickness and mantle density, which in turn have implications for the formation of Venus's highland crust. I perform spatio-spectral localization of gravity and topography on Mercury from the MErcury Surface, Space ENvironment, GEochemistry, and Ranging (MESSENGER) mission, and I perform analytical calculations of two layered mantle flow in order to interpret the high low degree admittances associated with Mercury's domical rises. Finally, I use lunar gravity from the Gravity Recovery And Interior Laboratory (GRAIL) mission along with topography from the Lunar Orbiter Laser Altimeter (LOLA) to quantify the stress state in the nearside maria, thereby placing constraints on the Moon's thermal evolution.

Thesis Supervisor: Maria T. Zuber
Title: E. A. Griswold Professor of Geophysics

Acknowledgments

The quality of my thesis was improved by the feedback and camaraderie of fellow graduate students. Alex Evans, Frank Centinello, Sonia Tikoo-Schantz, Grant Farmer, Mike Sori, Yodit Tewelde, Mattieu Talpe, Anton Ermakov, ZhenLiang Tian, Junlun Li, Roger Fu, Ben Mandler, Di Yang and Stephanie Brown were all valuable peers with whom I discussed planetary science matters, and my early years at MIT benefitted from the mentorship of senior students such as Mike Krawczynski, Einat Lev, Wes Watters, Jenny Suckale, Erwan Mazarico, Jiangning Lu. While my officemates Ruel Jerry, Lucas Willemsen, Jean Arthur Olive, Fuxian Song and Fred Pearce did not readily fit into either of the previous categories, they deserve thanks for enlivening my graduate school experience.

A number of faculty and staff at MIT aided me throughout graduate school. Maria Zuber was my primary advisor, and her enthusiasm for my work motivated me after every one of our meetings. Brad Hager advised my reservoir modeling research, and his input helped flesh out crucial portions of this thesis related to dynamic flow. Tim Grove, Dale Morgan and Roger Phillips, Tom Herring, Margaret Lankow, Roberta Allard and Terri MacLoon were each a source of support for me.

I have my parents to thank for fueling my obsessions with maps and mathematics, and their influence on my career has convinced me that educational outreach should be a priority in any planetary science endeavors. Our home was a better incubator for scientific curiosity than any school could have been.

Finally I would like to thank the entities that funded this work, namely NASA, the Planetary Geology & Geophysics program, the Massachusetts Institute of Technology, and U.S. taxpayers. It is a privilege and it is immensely fulfilling to perform theoretical studies pertaining to the inner workings of distant worlds, and I am personally grateful for the opportunity to do this work.

Contents

List of Figures

List of Tables

Chapter 1

Introduction

Our inner solar system contains five large rocky bodies: Mercury, Venus, the Moon, Earth and Mars. Scores of new exoplanets are discovered every year, and as astronomers search for Earth-like planets orbiting distant stars it is becoming increasingly important to understand the diversity of Earth-like objects in our own Solar System. Beyond merely aiding in the search for exoplanets, though, the study of terrestrial bodies in our solar system helps us understand our own planet better. The paradigm of plate tectonics endemic to Earth has yet to be observed on another planet, which gives motivation to re-examine exactly how the mechanisms of plate tectonics exist on Earth. Flood volcanism on Mercury and Venus are reminiscent of volcanic events such as the one that formed the Siberian Traps and may have caused a mass extinction. The pristine cratering record on the Moon offers our best record of the accretionary environment in the early solar system. Finally, the evidence concerning dynamic evolution of these bodies offers constraints on numerical models, which, though sophisticated, suffer from a dearth of observational data points.

The most successful tool for studying the Earth's interior has been seismic interpretation. Seismologists have used tomographic inversions of time series data in a global network of seismometers to map seismic velocities throughout the interior, which can in turn be used to infer physical quantities such as density, composition and mineral phase. Material interfaces in the Earth often reflect seismic waves, and prominent reflective interfaces have been connected to the interior structure, such as the inferred connection between the Mohorovičić discontinuity and the crust-mantle boundary. Regions of complete or par-

tial melt often result in an observable attenuation of shear waves. Finally, splitting of shear waves inform seismologists of anisotropic mineral structure, such as may result from prolonged mantle flow. Unfortunately seismic data beyond the Earth are extremely limited. Although seismometers were deployed on the Moon during the Apollo missions and on Mars via the Viking landers, these seismometers are generations behind Earth-based seismic networks in sophistication and spatial coverage, so interpretation of these seismic data comes with a certain amount of ambiguity. A seismic lander for Mars called InSight is currently under development by NASA, but again, a single seismometer will be limited in its sampling of the Martian interior.

In the absence of seismic observations, there are a number of means with which to interpret interior structure. Gravitational interactions between a satellite and a planetary body (or interactions between multiple planetary bodies) gives an estimate of the planet's mass, and estimates of volume can consequently give the mean density and bulk composition. Observations of precession can be used to infer moment of inertia, which is determined in part by the size of a metallic core. Along with the degree-2 shape of the body, small changes in the rotation rate of a planetary body (called librations) can give the depth to a liquid portion of the interior. Distortion of the body's shape due to tidal interactions can be measured as Love numbers, and these quantities are dependent on the elastic structure of the planet. Inductance connected with to the solar magnetic field can yield insights into the planet's conductivity and composition.

Arguably more powerful than any of these methods is the recovery of a planetary body's gravity field. Variations in the gravitational acceleration exterior to a planet perturb the trajectory of an orbiting spacecraft, and these perturbations may be observed as Doppler shifts in the returned telemetry. A gravity field is a function of the mass distribution in a planetary body, and as such a gravity field may be used to non-uniquely invert for the mass distribution inside a planet. A downward continuation of the gravity field to the crust-mantle interface produces an estimate of lateral variations in crustal thickness. The constraints on crustal volume resulting from this analysis allows for inferences of bulk composition. Gravity anomalies may also arise from mass variations apart from the crust-mantle interface, so nuanced analysis is required to separate the effects of these mass distributions.

Another important tool for planetary geophysics is topography. Topography data alone may be used to draw conclusions about a planetary body's evolution by identifying regional slopes, using crater depth/diameter ratios to infer infill volumes, etc. However, topography data becomes especially useful when analyzed in conjunction with a planetary gravity field. Ratios of gravity to topography in the spatial and spectral domain are particularly helpful for distinguishing between mechanisms of topographic support such as crustal compensation, dynamic flow, and elastic flexure.

In this thesis, Chapter 2 focuses on the gravity and topography of Venus returned by NASA's Magellan mission. In Chapter 3 we perform spatio-spectral localization of gravity and topography on Mercury using the data currently being returned by NASA's MESSENGER spacecraft, and we use this analysis to interpret the mechanisms of supporting long-wavelength topography. Chapter 4 addresses the stress state of the Moon using free-air gravity returned by NASA's GRAIL mission. Finally, Chapter 5 addresses opportunities for future work using the aforementioned data sets.

Chapter 2

Crustal thickness and support of topography on Venus

2.1 Introduction

In addition to being our nearest planet, Venus is similar to Earth in both size and composition. Rocks sampled by the Venera space probes were determined to be primarily basaltic in composition, although all the Venera landing sites were within smooth volcanic provinces (e.g., *Surkov et al.*, 1984). From bulk density arguments the mantle is assumed to have a peridotite composition (*Fegley*, 2004), similar to Earth. In spite of the similarities between Venus and Earth, however, the two planets have some conspicuous differences. The most striking difference in a geological sense is the apparent absence of plate tectonics on Venus (*Kaula and Phillips*, 1981; *Solomon et al.*, 1992), although tectonic comparisons to Earth have been made (*McKenzie et al.*, 1992; *Sandwell and Schubert*, 1992) amidst some controversy. Ridge spreading and ocean slab subduction are the primary sources of heat loss for Earth, but heat loss on Venus must be facilitated by another mechanism such as volcanism or thermal convection without lithospheric motion.

The majority of the surface consists of low-lying volcanic plains, and the regions of high topography can be classified either as volcanic rises associated with recent hotspot activity (*Smrekar et al.*, 2010), or as shallowly compensated crustal highlands (i.e. crustal plateaus). One significant exception in this classification scheme is Ishtar Terra, which, excluding

its boundaries, is markedly less deformed than the other highland regions (*Phillips and Hansen*, 1994). The origin of the crustal highlands has been attributed to either tectonic thickening of the crust above mantle downwellings (*Bindschadler*, 1992; *Ivanov and Head*, 1996) or massive melting associated with upwelling mantle plumes (*Phillips and Hansen*, 1998). Either of these scenarios represent a significant departure from the plate tectonics paradigm endemic to Earth, and as such Venus serves as an important laboratory for testing geodynamical models.

Because the crust contains a large portion of a terrestrial planet's incompatible elements, the volume of crust on a planet is an important parameter for understanding the extent of melting in the mantle (cf. *Rudnick and Gao*, 2005). In the absence of seismic data collection, gravity is the best geophysical tool for constraining the structure of the interior. In this paper we will use the relationship between global topography and gravity data to model crustal thickness and other parameters in the Venusian interior, first by inferring apparent compensation depths from geoid to topography ratios, and then by performing a two-layered inversion of the gravity field. This two-layered inversion solves for crustal thickness variations and a lateral distribution of mass in the mantle.

2.2 Data

Several robotic missions to Venus have collected gravity and topography data, of which NASA's Magellan mission provides the most complete set to date. Magellan collected topography data via radar altimetry and a relatively high resolution gravitational field via a dedicated gravity acquisition phase. Magellan altimetry (*Ford and Pettengill*, 1992) covered 93% of the surface, but the data gaps can be filled in with altimetry data from Pioneer Venus Orbiter and Venera 15/16 to produce a more complete map of topography. The *VenusTopo719* data product (Figure 2-1) provides to degree 719 the real spherical harmonic coefficients of topography using these altimetry data (*Wieczorek*, 2007). For the gravitational potential we use the degree 180 *MGNP180U* data product (Figure 2-2), which was based on Magellan data and augmented with observations from Pioneer Venus Orbiter (*Konopliv et al.*, 1999). The power of Venusian topography as a function of spherical har-

monic degree l is roughly proportional to l^{-2} due to its approximately scale-invariant shape (*Turcotte*, 1987). At intermediate wavelengths, the *MGNP180U* geoid power fits Kaula's law ($S_{NN}(l) \sim l^{-3}$, (*Kaula*, 1966)), which is produced by a random distribution of density anomalies in the interior (*Lambeck*, 1976).

Since we are interested in the relationship between the two data sets, the topographic data is useful only up to the resolution of the gravity data. The power spectrum of the error in the *MGNP180U* data product surpasses the power of the coefficients above degree 70 (spatial block size ~270 km), so we regard this as the nominal global resolution of the data set. The degree 1 terms correspond to the offset between the center of mass and the center of figure, and we remove these from the spherical harmonic expansion of topography. The actual spatial resolution varies considerably, with a resolution as high as degree 100 near the equator and as low as degree 40 elsewhere on the planet (see *Konopliv et al.* (1999) for a complete resolution map).

When geoid height and topography are plotted with respect to one another (Figure 2-3) we can see that the two data sets have a complicated relationship that is poorly fit by a single linear trend. We will apply potential theory and models of topographic support in order to unravel this relationship between topography and gravitational potential on Venus.

2.3 Methodology

2.3.1 The geoid and topography

It is useful to express a spherical function $f(\Omega)$, where $\Omega \in (\theta, \phi)$ represents position on the surface of a sphere, as a linear combination of real spherical harmonics:

$$f(\Omega) = \sum_{l=0}^{\infty} \sum_{m=-l}^{l} f_{lm} Y_{lm}(\Omega), \tag{2.1}$$

$$f_{lm} = \frac{1}{4\pi} \iint_{\Omega} f(\Omega) Y_{lm}(\Omega) d\Omega \tag{2.2}$$

where f_{lm} denotes the spherical harmonic coefficient at degree l and order m for the func-

tion $f(\Omega)$, and $Y_{lm}(\Omega)$ denotes the real spherical harmonic functions:

$$Y_{lm}(\Omega) = \begin{cases} \overline{P}_{lm}(\cos\theta) \cdot \cos m\phi & m \geq 0 \\ \overline{P}_{l|m}(\cos\theta) \cdot \sin |m|\phi & m < 0 \end{cases} \tag{2.3}$$

Here, θ is the colatitude, ϕ is the longitude, and $\overline{P}_{lm}$ are 4π-normalized associated Legendre polynomials (*Kaula*, 1966). The power spectrum of f is defined to be the sum of the squared spherical harmonic coefficients at each degree l:

$$S_{ff}(l) = \sum_{m=-l}^{l} f_{lm}^2. \tag{2.4}$$

The height of the gravitational equipotential surface $N(\Omega)$ (the "geoid") at the planetary radius R can be calculated from the gravitational potential field, $U(\Omega, r)$, using a first-order Taylor series approximation over the radial coordinate r:

$$U(\Omega, R + \delta r) = U(\Omega, R) + \frac{\partial U(\Omega, R)}{\partial r} N(\Omega) \tag{2.5}$$

Equation 2-6 is sometimes called Bruns' formula, and the radial derivative of potential is the surface gravitational acceleration g, which we will consider to be constant (dominated by $l = m = 0$ term, g_0) over the surface. The static geoid perturbation $N^B(\Omega)$ produced by an interface $B(\Omega)$ at depth d with a density contrast $\Delta\rho_B$ can be calculated using an upward-continuation factor in the spherical wavenumber domain:

$$N_{lm}^B = \tfrac{4\pi G R_B}{g(2l+1)} \left(\tfrac{R_B}{R}\right)^{l+1} \Delta\rho_B B_{lm}, \quad R_B \leq R \tag{2.6}$$

where the subscript "lm" on N_{lm}^B indicates the spherical harmonic coefficients of N^B (likewise for B_{lm}), G is the gravitational constant, R is the planetary radius, and the radial position of the interface B is $R_B = R - d$. In spherical geometries it is mathematically succinct to work with radii rather than depths, so we use notation of this form. Some deep-seated topographic compensation sources, such as thermal density anomalies or dynamic support, are not associated with relief on an interface. Therefore when we characterize mantle compensation in section 3.2, it is more physically appropriate to replace the prod-

uct $\Delta\rho_B B_{lm}$ in equation 2-6 with a load term Ψ_{lm}, signifying anomalous mass per unit area. In the case where surface topography is supported exclusively by relief on the crust-mantle interface $W(\Omega)$ (the "Moho"), the observed geoid is equal to the sum of the geoid contributions from planetary shape $H(\Omega)$ ("topography") and from W:

$$N^{Airy} = N^H + N^W \tag{2.7}$$

where N^H and N^W refer to the static contributions to the geoid at $r = R$ from H and W, respectively.

The ratio of geoid height N to topography H is frequently used to characterize the compensation of topography; in the spectral domain this non-dimensional ratio is known as the "admittance spectrum", and in the spatial domain it is called the "geoid-to-topography ratio" (GTR). When a compensation model is assumed, a GTR can be used to calculate the isostatic compensation depth at which the amplitude of the observed geoid is reproduced. In the Airy crustal compensation model, the weight of topography is balanced by the buoyancy associated with Moho relief W:

$$\rho_c g\bar{H} = -\left(\frac{R_W}{R}\right)^2 \Delta\rho g\bar{W} \tag{2.8}$$

where R_W is the radius of the Moho, $\bar{H} = H - N$, $\bar{W} = W - N^{r=R_W}$, and $N^{r=R_W}$ is the local equipotential surface at $r = R_W$. If the gravitational acceleration does not change with depth and if we ignore the contributions of equipotential surfaces, this reduces to a requirement that mass is conserved in a vertical column. We note a subtle distinction between H and $\bar{H}$. While we have been referring to the planetary shape H as "topography", it is common in geophysics literature to reserve the term "topography" for the planetary shape in excess of the geoid (e.g. *Smith et al.* (1999)). Therefore, what we now call $\bar{H}$ is, by some conventions, true topography.

The degree dependent ratio of geoid height to topography (the admittance spectrum, Z_l), can be found by assuming a compensation mechanism and a depth of compensation d. We calculate the admittance spectrum for Airy isostatic compensation by inserting equations 2-6 and 2-8 into equation 2-7, neglecting the depth dependency of gravitational ac-

celeration and the contributions of local equipotential surfaces:

$$Z_l^{Airy} = \frac{N_{lm}}{H_{lm}} \approx \frac{4\pi G R \rho_c}{g(2l+1)} \left[1 - \left(\frac{R-d}{R} \right)^l \right]. \tag{2.9}$$

The superscript label "Airy" indicates that this admittance function Z corresponds to Airy isostatic compensation. When the depth d is inferred from the observed geoid and topography, it is called the "apparent depth of compensation" (ADC). For crustal compensation, d is the Moho depth $R - R_W$.

Since the ratios of geoid to topography resulting from Airy isostasy have a linear and quadratic dependence on finite-amplitude topographic height (*Haxby and Turcotte*, 1978), it is possible in some situations to distinguish between Airy isostatic compensation and Pratt isostatic compensation, which assumes compensation via lateral density variations and depends only linearly on topography. In particular, *Kucinskas and Turcotte* (1994) and *Kucinskas et al.* (1996) systematically tested Airy and Pratt compensation models for various Venusian highland regions. For topographic heights less than a few kilometers the quadratic term for Airy isostasy is small, making it difficult to reliably distinguish between the two compensation mechanisms over a majority of the planet's surface. However, we will note that ideal Pratt compensation is unlikely on Venus: a relatively large density contrast of 400 kg m^{-3} between the lowest and highest points on the surface would require a global compensation depth ($\sim$mean crustal thickness) of about 100 km, but this compensation depth is likely precluded by the granulite/eclogite phase transition (see section 3.4). Therefore we will not address the possibility of significant density variations within the crust other than to say that the results of previous studies do not broadly contradict our assumption of Airy crustal compensation.

Wieczorek and Phillips (1997) showed that if a compensation mechanism is independent of position, the GTR associated with that mechanism can be represented by a sum of spectrally weighted admittances:

$$GTR = \frac{\sum_l S_{HH}(l) Z_l}{\sum_l S_{HH}(l)}. \tag{2.10}$$

If the unknown topography resulting from a compensation mechanism is assumed to have

a scale-invariant distribution (i.e. $S_{HH}(l) \propto l^{-2}$) then the GTR can be approximated for an arbitrary configuration of the compensating source:

$$GTR = \frac{\sum_l l^{-2} Z_l}{\sum_l l^{-2}}. \tag{2.11}$$

We can measure GTRs on the surface of Venus by performing minimum variance fits of the observed geoid and topography. This requires sampling the geoid and topography at equally spaced points over the surface of the planet; e.g. $H_i = H(\Omega_i)$. After sampling the geoid and topography on an octahedrally projected mesh at about 100,000 points (i.e. a sample spacing much finer than the resolution of the spherical harmonic data set) we minimize the sum of the squares of the windowed residuals, denoted by Φ:

$$\Phi = \sum_i \omega_i (GTR \cdot H_i + y - N_i)^2 \tag{2.12}$$

where y is the geoid offset and ω_i is a windowing function. We use a simple cosine-squared window in order to provide a localized fit with a sampling radius a centered at $\mathbf{x}_0$:

$$\omega_i = \begin{cases} \cos^2\left(\frac{\pi}{2a} \parallel \mathbf{x}_i - \mathbf{x}_0 \parallel\right) & \parallel \mathbf{x}_i - \mathbf{x}_0 \parallel \leq a \\ 0 & \parallel \mathbf{x}_i - \mathbf{x}_0 \parallel > a \end{cases} \tag{2.13}$$

where $\mathbf{x}_i$ is the cartesian location of the i^{th} sample. By minimizing Φ with respect to GTR and y we can solve for GTR at a point $\mathbf{x}_0$ on the surface:

$$GTR = \frac{\sum_i H_i N_i \omega_i \cdot \sum_i \omega_i - \sum_i H_i \omega_i \cdot \sum_i N_i \omega_i}{\sum_i H_i^2 \omega_i \cdot \sum_i \omega_i - \left(\sum_i H_i \omega_i\right)^2}, \tag{2.14}$$

where all the summations cycle through i. Note that when ω_i is defined to be a step function of unit magnitude, equation 2-14 reduces to the ratio $Cov(H_i, N_i)/Var(H_i)$.

An admittance function such as the one given in equation 2-9 predicts the ratio of geoid to topography as a function of spherical harmonic degree, but doesn't accommodate information about spatially varying compensation. On the other hand, a GTR calculated with a spatial regression is a function of position but loses any spectral information. Both of these mathematical tools have been used to characterize depths and mechanisms of com-

pensation (e.g., *Kiefer and Hager*, 1991; *Smrekar and Phillips*, 1991), but there will always be a tradeoff between spatial resolution and spectral fidelity. Spatio-spectral localization techniques (*Simons et al.*, 1994, 1997; *Wieczorek and Simons*, 2007) blur the line between these two approaches by calculating admittance spectra within a localized taper. This approach retains some information in the wave-number domain while accepting a certain amount of spatial ambiguity. *Anderson and Smrekar* (2006) used spatio-spectral localization to test isostatic, flexural and dynamic compensation models over the surface of Venus. These techniques necessarily exclude the longest wavelengths, which account for the bulk of the power of the geoid and topography due to the red-shifted nature of both data sets. In contrast, our two-layered inversion (section 3.4) incorporates all wavelengths.

2.3.2 Dynamic flow

We have thus far considered only isostatic compensation mechanisms, but we can generalize our analysis to dynamic flow in the Venusian interior. *Richards and Hager* (1984) introduced some depth-dependent kernels in their analysis of dynamic topography, three of which are pertinent to our analysis. The first is the dynamic component of the geoid normalized by the mantle mass load (the "geoid kernel"):

$$G_l^{dyn} = \frac{N_{lm}^{dyn}}{\Psi_{lm}} \tag{2.15}$$

where $N^{dyn}(\Omega)$ is the component of the geoid produced by dynamic flow and $\Psi(\Omega)$ is a sheet mass which drives viscous flow. The second kernel we use is simply the gravitational admittance associated with dynamic flow:

$$Z_l^{dyn} = \frac{N_{lm}^{dyn}}{H_{lm}^{dyn}} \tag{2.16}$$

where $H^{dyn}(\Omega)$ is the component of topography produced by dynamic flow. When considering the effects of self-gravitation, it is sometimes convenient to use an adjusted admittance function:

$$\bar{Z}_l^{dyn} = \frac{N_{lm}^{dyn}}{H_{lm}^{dyn} - N_{lm}^{dyn}} = \left(\frac{1}{Z_l^{dyn}} - 1 \right)^{-1}. \tag{2.17}$$

The third kernel gives the surface displacements normalized by the mantle mass load (the "displacement kernel"):

$$D_l^{dyn} = \frac{H_{lm}^{dyn}}{\Psi_{lm}} = \frac{G_{lm}^{dyn}}{Z_{lm}^{dyn}}. \tag{2.18}$$

These three kernels can be analytically calculated for a loading distribution within a viscous sphere (see Appendix B). We have plotted the kernels in Figure 2-4 for a number of parameters, including elastic thickness, surface boundary conditions, viscosity structure, and loading depth. The geoid and displacement kernels are generally negative, and they approach zero at high spherical harmonic degrees. This means that a positive mass load Ψ is associated with a negative geoid and topography at the surface, and that shorter wavelength mass loads have relatively subdued surface expressions. The admittance kernel is significantly red-shifted, with higher geoid-to-topography ratios at longer wavelengths. We can also use Figure 2-4 to qualitatively understand the effects of parameter values on the dynamic kernels. A free-slip surface boundary condition results in a slightly reduced admittance at the lowest degrees, and a thicker elastic lithosphere decreases the admittance at high degrees. Viscosity profiles that increase with depth result in complicated dynamic kernel plots, but generally decrease the admittance spectrum. A deeper loading depth increases the admittance spectrum across all degrees, but results in a subdued surface expression of the geoid and topography at short to intermediate wavelengths.

Given that strain rates on Venus are likely to be small (*Grimm*, 1994), the surface can be modeled as a no-slip boundary, and a free slip boundary condition approximates the coupling between the mantle and the liquid outer core at radius $r = R_C$. Other authors (e.g., *Phillilps*, 1986; *Phillips et al.*, 1990; *Herrick and Phillips*, 1992) have examined the appropriateness of various viscosity structures and concluded that Venus lacks a low-viscosity zone in the upper mantle. Other studies have suggested that Venus may have a viscosity profile that increases with depth, similar to Earth's viscosity structure [Pauer et al., 2006]. For the sake of limiting the parameter space, we assume an isoviscous mantle

and only qualitatively consider the effects of more complicated radial viscosity profiles.

The spherical harmonic coefficients for dynamic topography are given by $H_{lm}^{dyn} = D_{lm}^{dyn}\Psi_{lm}$, and if the distribution of the load Ψ is assumed to be scale-invariant then the power of dynamic topography is proportional to $\left(D_l^{dyn}\right)^2 l^{-2}$ and the observed GTR for a dynamic model can be calculated:

$$GTR = \frac{\sum_l D_l^{dyn^2} l^{-2} Z_l^{dyn}}{\sum_l D_l^{dyn^2} l^{-2}}. \tag{2.19}$$

Various theoretical curves quantifying the relationship between GTR and compensation depth are summarized in Figure 2-5 for dynamic and Airy isostatic compensation. The GTR associated with Airy isostatic compensation calculated in a Cartesian coordinate system is linear with depth, but *Wieczorek and Phillips* (1997) showed that this calculation will underestimate the true compensation depth in a sphere. In contrast, the GTR associated with dynamic flow (equation 2-19) is much larger for a given loading depth. However, these relationships assume a global sampling of geoid topography, and a windowing of N and H such as the one given in equation 2-13 will invariably under-sample the longest wavelengths of the admittance spectrum. The relationship between the power of windowed data and spherical data for Slepian tapers is stated explicitly in equation 2.11 of *Wieczorek and Simons* (2007). Since the dynamic flow kernel is largest at low degrees (see Figure 2-4), a windowed measurement of a dynamically compensated GTR will be smaller than a global measurement for the same compensation mechanism. In order to quantify the effect of window size on the observed GTR, we created synthetic data sets by randomly generating topography spectrally consistent with Venus's and calculating geoids for dynamic compensation in the wavenumber domain according to equation 2-16. We then performed regression fits of geoid to topography using windows with sampling radii of a = 600, 1000, and 2000 km. The expectation values of these windowed dynamic GTRs as a function of loading depth are listed for select compensation depths in Table 2-2, and plotted in Figure 2-5.

2.3.3 Support of topography

The excess mass from surface topography must be supported through a combination of crustal thickness variations, a laterally heterogeneous distribution of density, dynamic flow, and stresses in the lithosphere. We can constrain the interior structure of Venus by requiring that the loads provided by these mechanisms cancel the load of topography at the surface of the planet.

Topography and the crust-mantle boundary both produce loads where they depart from the local gravitational equipotential surface. While the surface geoid is observable, the equipotential surface at a given depth is dependent on the planet's internal structure. This potential field can be approximated by including contributions from topography, from relief on the crust-mantle interface $W(\Omega)$ with a density contrast $\Delta\rho$, and from a mantle load $\Psi(\Omega)$ with units of kg m^{-2}. The resulting equipotential surface at $r = R_W$ is calculated by applying equation 2-9 for the three interfaces:

$$N_{lm}^{r=R_W} = \frac{4\pi G}{g_W(2l+1)} \left[R \left(\frac{R_W}{R} \right)^l \rho_c H_{lm} + R_W \Delta\rho W_{lm} + R_\Psi \left(\frac{R_\Psi}{R_W} \right)^{l+1} \Psi_{lm} \right]. \tag{2.20}$$

We neglect the contribution from relief on the core-mantle boundary (the "CMB"), as it has a second-order effect here (an *a posteriori* check confirms that flow-induced CMB relief contributes less than one meter to $N^{r=R_W}$).

Stresses in the lithosphere can also support topography under the right conditions. While a variety of stress distributions are possible, we will assume a simple model in which loads are supported by flexure of a thin elastic lithosphere. The lithosphere of Venus can be modeled as a shell of thickness T_e, and we define $F(\Omega)$ to be the deflection of the shell from its undeformed configuration. *Bilotti and Suppe* (1999) observed a geographical correlation between compressional wrinkle ridges and geoid lows, along with a similar correlation between rift zones and geoid highs. While a number of regions are well fit by top loading admittance models (*Anderson and Smrekar*, 2006), the tectonic patterns observed by *Bilotti and Suppe* (1999) are broadly consistent with the stress distribution produced by bottom loading of an elastic shell. For simplicity, we define the flexural deflection $F(\Omega)$ to be the

component of topography produced by dynamic flow:

$$F = \delta H^{dyn}. \tag{2.21}$$

In other words, we invoke an elastic lid that resists deformation of the surface by dynamic flow. By necessity, this model assumes a globally-uniform elastic thickness T_e. We assume T_e = 20 km, slightly less than the elastic thicknesses inferred at some volcanic rises (*McKenzie and Nimmo*, 1997). However, is not clear if these estimates of elastic thickness are globally representative (*Anderson and Smrekar*, 2006), so we acknowledge significant uncertainty in T_e.

Since the magnitude of flexure is coupled to the unknown mantle load Ψ it must be incorporated into the dynamic flow kernels (see Appendix B). We can then represent the spherical harmonic coefficients of topography in excess of the geoid by assuming a normal stress balance, with superimposed contributions from $\bar{W}$ and dynamic flow:

$$\bar{H}_{lm} = -\frac{\Delta\rho}{\rho_c}\left(\frac{R_W}{R}\right)^2 \bar{W}_{lm} + \frac{G_l^{dyn}}{\bar{Z}_l^{dyn}}\Psi_{lm} \tag{2.22}$$

where the kernels G_l^{dyn} and $\bar{Z}_l^{dyn}$ come out of the dynamic flow calculation.

2.3.4 Two-layered inversion

A single-layer inversion of gravity data is performed by downward-continuing observed gravity anomalies to an interface at some depth below the surface. Assuming that all Bouguer gravity anomalies come from relief on the crust-mantle interface, versions of equation 2-6 have been used to solve for crustal thickness distributions on the Moon (*Zuber et al.*, 1994; *Wieczorek and Phillips*, 1998), Mars (*Zuber et al.*, 2000; *Neumann et al.*, 2004) and Venus (*Wieczorek*, 2007). However, we have argued that crustal thickness variations on Venus cannot be solely responsible for the observed geoid (cf. Figure 2-3). For mean thicknesses of 10-50 km the GTRs associated with crustal thickness variations are 1-6 m km^{-1}, and with a globally sampled GTR of 26 m km^{-1} it is clear that the observed geoid must be in large part produced by a deep compensation source. To isolate the portion

of the geoid corresponding to crustal thickness, we will simultaneously invert for crustal thickness and mantle mass anomalies.

Previous studies have similarly endeavored to remove high-GTR trends from the geoid: two-layered gravity inversions have been performed for Venus by *Banerdt* (1986), to solve for two mass sheets in the presence of an elastic lithosphere, and by *Herrick and Phillips* (1992), to characterize dynamic support from mantle convection. However, these studies did not have access to Magellan gravity models, which limited their analyses to spherical harmonic degrees less than 10 and 18, respectively. Although a follow-up study by *Herrick* (1994) did incorporate some gravity data from Magellan, resolution of the gravitational potential had only been improved to degree 30 by that point. Since the current gravity data has a resolution of $\sim$70 degrees, our model provides the highest-resolution map of spatial variations in crustal thickness.

We remove the high-GTR trends from the geoid by performing an inversion for relief on the crust-mantle interface $W(\Omega)$ and for the mantle load $\Psi(\Omega)$. This means that there are two unknowns, W_{lm} and Ψ_{lm}, for each spherical harmonic degree and order, and we can invert uniquely for these coefficients by imposing two sets of equations. We use a crustal density of ρ_c = 2800 kg m^{-3} and a crust-mantle density contrast of $\Delta\rho$ = 500 kg m^{-3}, although neither of these quantities are well-constrained due to uncertainties in the composition of the crust and mantle.

Our first set of equations, given by 2-22, constrains topography to match the topography produced by crustal isostasy and by dynamic flow in the presence of an elastic lid. This is equivalent to a normal stress balance at the surface of the planet. The second set of equations requires the observed geoid to equal the sum of the upward-continued contributions from H, W, Ψ, and the CMB. This can be posed more succinctly by invoking kernel notation and separating the geoid into its Airy component N^{Airy} and its dynamic component N^{dyn}:

$$N_{lm} = N_{lm}^{Airy} + N_{lm}^{dyn} = -Z_l^{Airy}\frac{\Delta\rho}{\rho_c}\left(\frac{R_W}{R}\right)^2\left(W_{lm} - D_l^{dyn}\Psi_{lm}\right) + G_l^{dyn}\Psi_{lm} + N_{lm}^{finite} \tag{2.23}$$

where N_{lm}^{finite} is a correction for finite amplitude relief (see Appendix A). Using equations 2-22 and 2-23 we can solve for the unknowns W_{lm} and Ψ_{lm}. N_{lm}^{finite} incorporates powers of H and W, and since the shape of the crust-mantle interface and its local equipotential surface are not known a priori the solution is iterative. We first solve for W_{lm} and Ψ_{lm} without $N^{r=R_W}$ or finite amplitude corrections for W or H (no finite amplitude corrections are applied for the mantle load). Then, we calculate $N^{r=R_W}$ and the finite amplitude terms using the current inversion solutions. The equations are solved again with these new estimates for the finite amplitude corrections, and this process is repeated until convergence (factor of $\leq 10^{-6}$ change for all coefficients) has been reached.

2.4 Results

2.4.1 Geoid-to-topography ratios

Venusian geoid-to-topography ratios are plotted for sampling radii a = 600, 1000, and 2000 km in Figure 2-6 along with the corresponding dynamic ADCs. *Smrekar and Phillips* (1991) calculated geoid-to-topography ratios and apparent depths of compensation for a dozen features on the Venusian surface, but the quality of gravity and topography data has improved significantly since then. In addition, we have improved the theory relating GTRs to compensation depths, so we update previous interpretations of compensation mechanisms on Venus. In particular, we have shown that the observed GTR is dependent on the size of the sampling window, and that a windowed GTR measurement for a given dynamic compensation depth will be smaller than the globally sampled GTR for the same compensation mechanism.

Mean geoid-to-topography ratios are listed in Figure 2-7 for a handful of geographic regions. Uncertainties are given by the spread of GTR estimates within a particular region, and the GTRs measured at the point of highest topography are given in parentheses. Since each sampling radius produces its own measurement of the GTR, we get multiple estimates of the compensation depth at each region. A region compensated by a single mechanism should produce a compensation depth that is consistent across various sampling radii. It

is interesting to note that the GTR measured at the point of highest topography within a region tends to be lower than the mean GTR for the region. This points to a correlation between locally high topography and a shallow compensation mechanism such as a crustal root, and it implies that Venus topography is supported at multiple compensation depths.

As would be expected for topography that is partially compensated by a dynamic mechanism (cf. Table 2-2), the mean GTR increases with sampling radius. For a sampling radius of a = 600 km the globally averaged GTR is 13 m km^{-1}, but the mean global GTR increases steadily for larger sampling radii, up to the globally sampled fit of 26 m km^{-1}. This is in contrast to the results of *Wieczorek and Phillips* (1997) for the lunar highlands, where the means and standard deviations of the GTR histograms were constant. The strong dependence of GTR measurements on sampling radii for Venus can be attributed to the presence of dynamic topography, for which the value of the admittance function is strongly dependent on wavelength (cf. Figure 2-4).

It should be understood that these compensation depths generally do not correspond to thickness of the crust, as most are deeper than the granulite-eclogite phase transition that represents a theoretical upper bound to the thickness of the crust (see the next section for discussion). This suggests that crustal thickening alone cannot explain the observed geoid and topography. *Smrekar and Phillips* (1991) reported a bimodal distribution of compensation depths, and histograms of GTRs as a percentage of surface area show a similar double-peaking for $a > 2000$ km (Figure 2-8). This motivates our two-layered compensation model.

2.4.2 Crustal thickness and mantle mass anomalies

A two-layered inversion is non-unique insomuch as the mean crustal thickness and a representative depth for the mantle load are unknown, and without the benefit of seismic data from Venus it is difficult to accurately infer either of these depths. However, we can place constraints on the depth of the crust-mantle interface. For a lower bound on the compensation depth $R - R_W$ (the mean crustal thickness), it can be noted that the solution for the crust-mantle interface should not produce negative crustal thickness anywhere on the

planet. This constraint was used on Mars to deduce a lower bound of 50 km for the mean crustal thickness (*Zuber et al.*, 2000; *Neumann et al.*, 2004). The lowest topography on Venus is a little more than 2 km below the mean radius, and this zero-thickness constraint results in a lower bound of roughly 8 km for $R - R_W$, depending on the compensation source (see Table 2-3). For an upper bound we refer to the granulite-eclogite phase transition under the assumption that the basaltic compositions measured by the Soviet landers are representative of the crust as a whole (Figure 2-9). Eclogite is $\sim$500 kg m^{-3} denser than basaltic rock, so any crust beyond the eclogite phase transition would be negatively buoyant and prone to delamination. Any eclogite material that is not delaminated will contribute negligibly to the observed geoid or to topographic compensation since its density would be close to that of mantle rock. The existence of stable crust below the solidus depth is also unlikely, so we regard the granulite-eclogite phase transition and the solidus as upper bounds for the thickest crust. The exact depths of these transitions rely on Venus's geothermal gradient, another quantity that has not been directly measured. However, the maximum depth for stable basalt crust will occur for a geothermal gradient between 5 and 10 °C km^{-1}. For any reasonable choice of inversion parameters the thickest crust is always found under Maxwell Montes on Ishtar Terra, so we will consider 70 km (cf. Figure 2-9) to be an upper bound for the thickness of the crust at Maxwell Montes. With this constraint, upper bounds for mean crustal thickness can be determined (see Table 2-3).

It is more difficult to constrain the dynamic loading depth, especially since the driving mass sheet is a simplification of a physical mechanism not confined to a particular depth (e.g. distributed density anomalies; see section 5.2 for discussion). However, we can inform our choice of loading depth by attempting to minimize the combined power spectra of H^W and H^Ψ. A slightly more subjective criterion for choosing the loading depth $R - R_\Psi$ involves the correlation of crustal thickness and the loading function. If we introduce the crustal thickness $T(\Omega) = H(\Omega) - W(\Omega)$, we can define the cross power spectrum for T and Ψ:

$$S_{T\Psi}(l) = \sum_{m=-l}^{l} T_{lm}\Psi_{lm} \tag{2.24}$$

A correlation function for crustal thickness and dynamic loading can then be calculated:

$$\gamma_{T\Psi}(l) = \frac{S_{T\Psi}(l)}{\sqrt{S_{TT}(l)S_{\Psi\Psi}(l)}}. \tag{2.25}$$

This degree-dependent function will equal zero where T and Ψ are uncorrelated. While it is not obvious that these two quantities should be completely uncorrelated, large positive or negative values of the correlation function are likely characteristic of a poor choice of model parameters: if a true compensation mechanism has an admittance spectrum significantly different from the admittances produced by both crustal thickening and dynamic flow, a two-layered model will produce solutions for T and Ψ that are either correlated or anti-correlated in an attempt to match the observations. We choose a loading depth of $R - R_\Psi$ = 250 km, noting that the combined power of H^{Airy} and H^{dyn} is minimized for large mantle loading depths. A larger chosen value of $R - R_\Psi$ reduces the power of H^{Airy} and H^{dyn} slightly but results in a stronger anti-correlation of T and Ψ at low spherical harmonic degrees. This depth also corresponds to the upper end of the regional GTR spread for a = 2000 km (cf. Figure 2-8) and to the upper cluster in the double-peaked histogram (Figure 2-8 in conjunction with Table 2-2).

We calculated solutions to equations 2-22 and 2-23 using the parameters listed in Table 2-4. Our smoothing filter for crust-mantle relief W is modified from *Wieczorek and Phillips* (1998), and is defined to have a value of 0.5 at the critical degree l_c:

$$\lambda_l^W = \left[1 + \frac{(2l+1)^2}{(2l_c+1)^2}\left(\frac{R}{R_W}\right)^{2(l-l_c)}\right]^{-1}. \tag{2.26}$$

We use l_c = 70 for our crustal thickness solution. A similar filter is used for mapping the mantle load Ψ, with l_c = 40.

Crustal thickness is plotted in Figure 2-10 and the mantle load is plotted in Figure 2-11; these plots emphasize crustal plateaus and volcanic rises, respectively. The addition of bottom-loaded flexure does not appreciably change the magnitude of crustal thickness, but finite amplitude corrections changed the calculated crustal thicknesses by as much as 6 km. A plot of the power of H^{Airy} and H^{dyn} (Figure 2-12) shows that dynamic loading is responsible for most of the long wavelength ($l < 27$) topography and that the crustal

thickness variations tend to support the shorter wavelengths.

In a number of highland regions (e.g. Alpha and Ovda Regiones) crustal thickness is well correlated to topography, while in other regions (e.g. Atla and Eistla Regiones) dynamic loading is the dominant contributor to topography. Other regions such as Thetis Regio appear to have superimposed contributions from crustal thickening and dynamic loading. The center of Thetis Regio features thickened crust, while the exterior topographic swell is supported by dynamic loading and has no thickening of the crust. The central region of crustal thickening within Thetis Regio is correlated to SAR-bright terrain (*Pettengill et al.*, 1991) as well as high-emissivity (*Pettengill et al.*, 1992).

2.5 Discussion

2.5.1 Mean crustal thickness

In the process of performing our two-layered crustal thickness inversion we have constrained the mean thickness of the crust to be 8-25 km for a reasonable range of physical parameters. The upper limit of this crustal thickness range is somewhat less precise than the lower limit due to uncertainties in the geothermal gradient and the kinetics of metamorphism. *Namiki and Solomon* (1993) argue that if Maxwell Montes was formed tectonically in the geologically recent past, a crustal root may have grown too quickly for the basalt-eclogite phase transition to limit crustal thickness. If we therefore exempt Maxwell Montes from our requirement that no crust should exceed 70 km thickness, the mean crustal thickness can be as large as 45 km for a geothermal gradient range of 5-10 °C km^{-1}.

Previous measurements of mean crustal thickness have been made using observations of crater relaxation states, characteristic spacing of tectonic features, and spectral gravity arguments. Noting that craters on Venus are relatively unrelaxed, *Grimm and Solomon* (1988) used viscous relaxation models to argue that the mean thickness of the crust should be less than 20 km for a geothermal gradient dT/dz = 10 °C km^{-1}. These conclusions were made under the assumption that the lower crust is very weak, but the experiments by *Mackwell et al.* (1998) have since shown that a dry lower crust can maintain relatively high

differential stresses. New relaxation calculations are needed, and the updated constraints on crustal thickness may be somewhat looser than those proposed by *Grimm and Solomon* (1988).

Zuber (1987) also constrained the mean crustal thickness to a range of 5-30 km by noting that the surface expressions of tectonic deformation often have two characteristic wavelengths. If these features can be interpreted as the result of a weak lower crust, the shorter wavelength may correspond to deformation of the upper crust while the longer wavelength would correspond to deformation of the rigid upper mantle. As with the constraints from crater relaxation, the *Zuber* (1987) models will need to be updated with the dry crust rheology of *Mackwell et al.* (1998), which is less distinguishable from ultramafic rheologies.

Previous gravity studies have provided estimates for the thickness of the crust by producing a fit to the observed admittance spectrum. *Konopliv et al.* (1999) notes that at high degrees the global admittance function is best fit by an Airy compensation model with 25 $< R - R_W <$ 50 km, and *Grimm* (1997) use the *Konopliv et al.* (1999) type of analysis to inform a choice of 30 km for the mean crustal thickness. Estimates of mean crustal thickness from the global admittance function are premised on the assumption that all high-degree topography is supported by crustal compensation. While this assumption may be true in many cases, we note that most exceptions involve mechanisms with higher GTRs (in particular, shallow mantle heterogeneities and flexurally-supported topography). Therefore we believe it is possible for a crustal thickness estimate produced by global admittance analysis to be an over-estimation. Regional crustal thickness estimates can similarly be made for localized spectral analysis (see Table 2-5 for a comparison of our crustal thicknesses with the results of *Anderson and Smrekar* (2006)), although spatio-spectral techniques do not produce global estimates for the mean crustal thickness. Our crustal thicknesses match those of the *Anderson and Smrekar* study at the crustal plateaus (where their crustal thickness estimates are most reliable) if we choose a global mean thickness of about 15 km.

2.5.2 Interpretation of the mantle load function

The function $\Psi(\Omega)$ represents anomalous mass in the mantle that drives flow, but thus far we have not speculated on the source of anomalous mass. One potential source for the observed mass anomalies is thermal density variations. We observe a number of roughly circular regions of mass deficit in the mantle along with broadly interconnected downwellings, and this distribution is consistent with models of a thermally convecting mantle (*Schubert et al.*, 1990; *Herrick*, 1994). The two largest regions of mass deficit, found at Atla and Beta Regiones, likely represent upwelling mantle plumes (*Smrekar et al.*, 2010). Assuming a volume thermal expansion coefficient of α = 3 x 10^{-5} C^{-1} and a maximum temperature contrast ΔT = 300 °C, density variations of $\rho_0 \alpha \Delta T$ = 30 kg m^{-3} might be reasonably expected due to thermal variations in the mantle. With this density contrast, thermally buoyant material would have to be distributed through ~450 kilometers of the vertical column in order to account for the mass deficits predicted at Atla and Beta Regiones.

Mass anomalies can alternatively be interpreted as compositional density anomalies, particularly those that arise from chemical differentiation. The Mg-rich mantle residuum left behind by fractional melting of a mantle parent rock has a reduced density due to a depletion of iron oxides. Globally, there is a long-wavelength ($l < 40$) correlation between the mantle load Ψ and the crustal thickness T, which is consistent with a parallel production of crustal material and Mg-rich residuum. We can test the plausibility of residuum as a source for the mantle load Ψ by comparing the mass of modeled crustal material to the anomalous mass in the mantle. Following the analysis of *Phillips et al.* (1990), the density of mantle residuum, ρ_r, can be modeled as a function of the melting mass fraction f and the density drop $\delta\rho_r$ from a mantle parent rock, ρ_m, to Mg-pure forsterite:

$$\rho_r = \rho_m - f\delta\rho_r. \tag{2.27}$$

Consider the fractional melting of a mantle parcel with an original mass M_0. Assuming all of the melt is extracted, the mass and volume of the resulting residuum material are, respectively, $M_r = (1 - f)M_0$ and $V_r = M_r/\rho_r$, and the extracted melt mass is equal to fM_0. The observable mass anomaly, δM, can be calculated as the difference between the

mass of residuum material and an equivalent volume of unmelted mantle:

$$\delta M = (1 - f) M_0 \left(1 - \frac{\rho_m}{\rho_r} \right). \tag{2.28}$$

Note that the residuum volume V_r will typically be smaller than the volume of the original parcel, and that primitive mantle material fills the space created by such a volume change. If all of the melt recrystallizes into the crust, we can represent the ratio of crustal mass, M_c, to the observable residuum mass deficit as:

$$\frac{M_c}{\delta M} = -\frac{\rho_r}{(1 - f)\delta\rho_r}. \tag{2.29}$$

Assuming densities of 3500 kg m^{-3} for primitive mantle material and 3250 kg m^{-3} for forsterite, and assuming a melt fraction $f = 0.1$, we would expect a ratio of crustal mass to anomalous residuum mass of about $M_c/\delta M \approx -15$. Figure 2-13 plots the total accumulation of crustal material in a number of regions of high topography, along with the corresponding mass deficits in those regions. Error bars in Figure 2-13 represent the distribution of mass estimates for a range of model parameters, including mean crustal thicknesses of 10-30 km, dynamic loading depths of 150-400 km, and elastic thicknesses of 0-30 km. The ratios of crustal mass to anomalous mantle mass in a number of regions, including Ishtar Terra and Ovda Regio, are consistent with the accumulation of mantle residuum. As shown in Figure 2-13, this proportionality is robust for a reasonable range of parameters. While Phoebe and Thetis Regiones also have accumulations of crust correlated with mass deficiency in the mantle, they have greater dynamic support than would be expected for a mantle residuum paradigm, so it is likely that they could be supported by thermal buoyancy in addition to the possible accumulation of residuum. The mass deficits at Atla and Beta Regiones are qualitatively different from the mass deficits at other locations on the planet, with larger amplitudes and narrower lateral extents. Atla and Beta also have much more dynamic support than would be expected in these regions from an accumulation of residuum, so it is likely that these mass deficits are primarily thermal in origin.

2.6 Conclusions

We have mapped the spatial variations of crustal thickness and a deep compensation mechanism (Figures 2-9 and 2-10). This inversion predicts that some topographic rises correspond to thickened crust (Ishtar Terra, Ovda Regio, Tellus Regio, Alpha Regio) while others are primarily compensated at depth (Beta Regio, Atla Regio). Mean crustal thickness has been constrained to a range of 8-25 km, so crustal material makes up between 0.2% and 0.7% of the total planetary mass. Basaltic phase constraints on crustal thickness required that the geothermal gradient be less than 15 °C km^{-1}, with an ideal range of 5-10 °C km^{-1}. Assuming a temperature of ~1450 °C at the base of the thermal boundary layer, this range of geothermal gradients predicts a thickness of 100-200 km for the thermal lithosphere. A model depth of 250 km for the mantle load was shown to be ideal for a two-layered inversion, but our mass sheet Ψ is a proxy for a more complicated distribution of mass in the mantle.

Our results allow us to separate provinces into three physiographic classes, defined by low, intermediate, and high GTR values. Provinces of the first class (GTR $<$ 10 m km^{-1}, calculated for a sampling radius a = 2000 km) are not strongly influenced by thermal convection, and high topography in these regions corresponds to thickening of the crust. Crustal plateaus in this class (except for those with the lowest GTRs) are possibly underlain by Mg-rich residuum in quantities that are consistent with a local melting source for crustal material. The intermediate class ($10 \leq$ GTR ≤ 20 m km^{-1}) may also correspond to accumulation of crust and anomalous concentrations of residuum, but the magnitudes of mass anomalies in the mantle are too large to be explained solely by residuum, and we must invoke some amount of likely thermally-driven uplift. These highlands may mark the sites of late-stage plumes, in which case they would be younger than regions of the first class. We conclude that provinces in the third class (GTR $>$ 20 m km^{-1}) are influenced primarily by present-day dynamic flow; this class includes volcanic rises, which are formed by mantle upwellings, and the low-lying plains, which are correlated with mantle downwellings.

This analysis points to a paradigm in which Venus topography is supported through a

combination of dynamic flow, melt residuum buoyancy, and thickening of the crust. While tectonic thickening of the crust has not been excluded, highland crust volumes are consistent with the accumulation of melt over upwelling mantle plumes.

Table 2.1: Summary of the functions and labeling conventions used in this paper.

Spherical functions	
H, $H(\Omega)$, H_{lm}	Shape of Venus (also "topography"). First two notations are interchangeable; third notation refers to the coefficients of the spherical harmonic expansion of H
N	The observed gravitational equipotential surface at the planetary radius $r = R$ (the "geoid")
N^H, N^W, N^Ψ	Static geoid contributions from topography, the Moho, and the mantle load
$N^{r=R_W}$	Gravitational equipotential surface at the radius of the Moho, $r = R_W$
W	Shape of the crust-mantle interface
Ψ	Mantle mass sheet (units of kg m^{-2})
F	Flexural displacement
$\bar{H}$, $\bar{W}$	Topography and Moho relief in excess of their local equipotential surfaces
N^{Airy}, N^{dyn}	The portions of the geoid generated by crustal isostatic and dynamic compensation
H^{Airy}, H^{dyn}	The portions of topography compensated by crustal isostatic and dynamic mechanisms
Degree-dependent parameters and kernels	
$S_{ff}(l)$, $S_{fg}(l)$	Power spectrum of the function f, cross-power spectrum of the functions f and g
Z_l^{dyn}, Z_l^{Airy}	Admittance kernels for dynamic flow and crustal isostasy
$\bar{Z}_l^{dyn}$	Associated dynamic admittance kernel
G_l^{dyn}	Geoid kernel (not to be confused with the gravitational constant, G)
D_l^{dyn}	Displacement kernel (not to be confused with flexural rigidity, D)

Table 2.2: Modeled GTRs for various Airy isostatic and dynamic compensation depths. These were empirically calculated using synthetic models of H and N, windowed using equation 2-13 using sampling radii a, and fit with linear regression (equation 2-14).

Airy Compensation Depth (km)	a = **600 km**	a = **1000 km**	a = **2000 km**
10	1.3	1.3	1.3
15	1.9	1.9	1.9
20	2.5	2.5	2.5
30	3.6	3.7	3.7
40	4.6	4.8	4.9
50	5.6	5.8	6.0
Dynamic Compensation Depth (km)	a = **600 km**	a = **1000 km**	a = **2000 km**
100	10	12	15
150	13	16	20
200	15	19	25
250	17	22	29
300	19	25	32
400	21	28	38

Table 2.3: Bounds on mean crustal thickness (for a maximum depth of 70 km at Maxwell Montes)

Dynamic Compensation Depth	**Lower bound (km)**	**Upper bound (km)**
100 km	22	30
150 km	11	27
200 km	9	26
250 km	8	25
300 km	8	24
400 km	7	23

Table 2.4: Parameter values for the two-layered inversion

Parameter	**Value**
Crustal density, ρ_c	2800 kg m^{-3}
Crust-mantle density contrast, $\Delta\rho$	500 kg m^{-3}
Mean crustal thickness, $R - R_W$	15 km
Mantle mass sheet depth, $R - R_\Psi$	250 km
Effective elastic thickness, T_e	20 km
Poisson's ratio, ν	0.25
Young's modulus, E	60 GPa
Core-mantle density contrast, $\Delta\rho_{core}$	3000 kg m^{-3}

Table 2.5: Comparison of crustal thickness estimates between this study (mean thickness of 15 km) and the spatio-spectral localization study of *Anderson and Smrekar* (2006)

Region	**This study**	**A & S**
Alpha Regio	23	25
Atla Regio	24	25
Atalanta Planitia	15	25
Beta Regio	26	65
Eistla Regio	17	95
Fortuna Tessera	31	25
Lakshmi Planum	41	45
Ovda Regio	37	35
Phoebe Regio	25	45
Tellus Regio	23	25
Thetis Regio	31	25

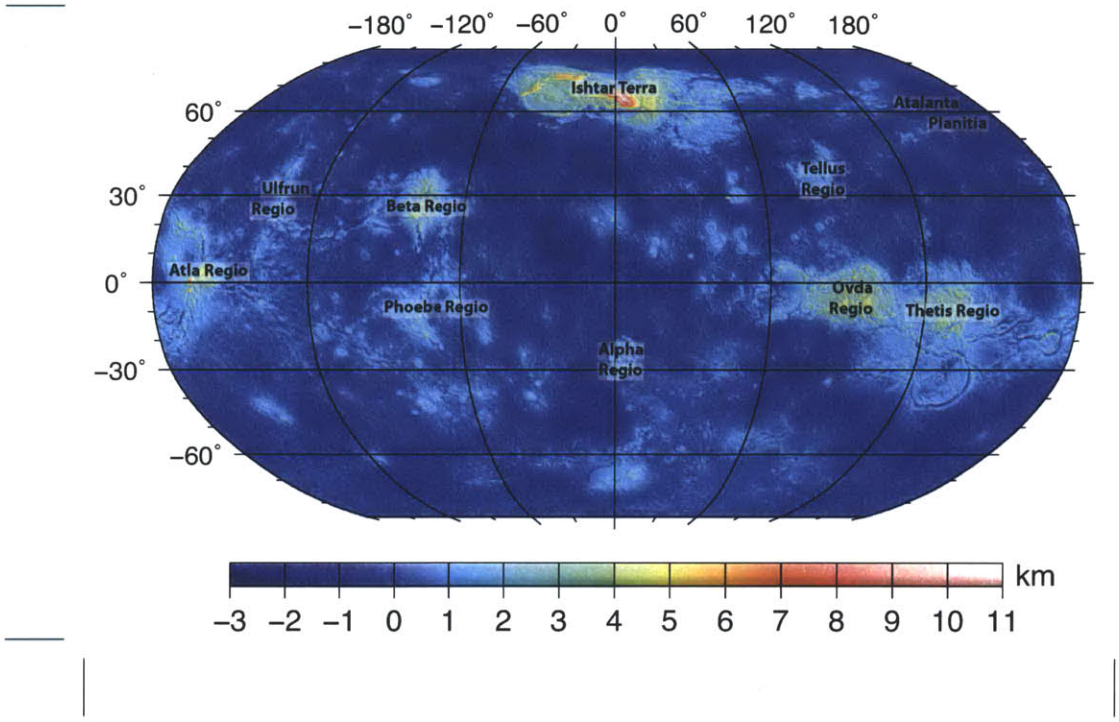

Figure 2-1: Venus topography (scale in km), rendered out to spherical harmonic degree 719. Spherical harmonic topography coefficients from *VenusTopo719*.

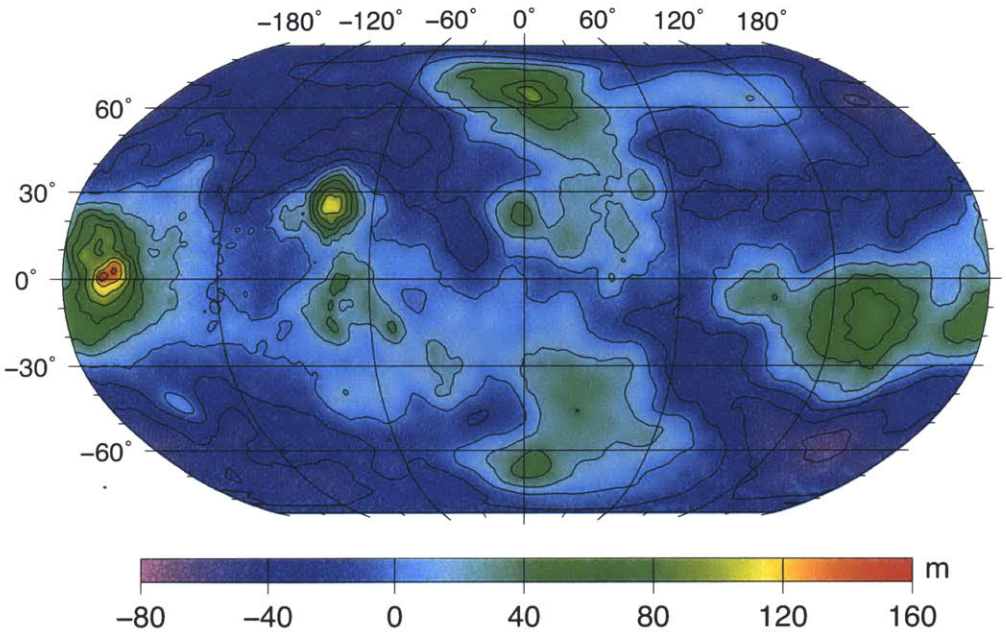

Figure 2-2: Venus geoid (scale in meters) rendered out to spherical harmonic degree 90. Contour spacing is 20 m. Spherical harmonic gravitational potential coefficients from *MGNP180U*.

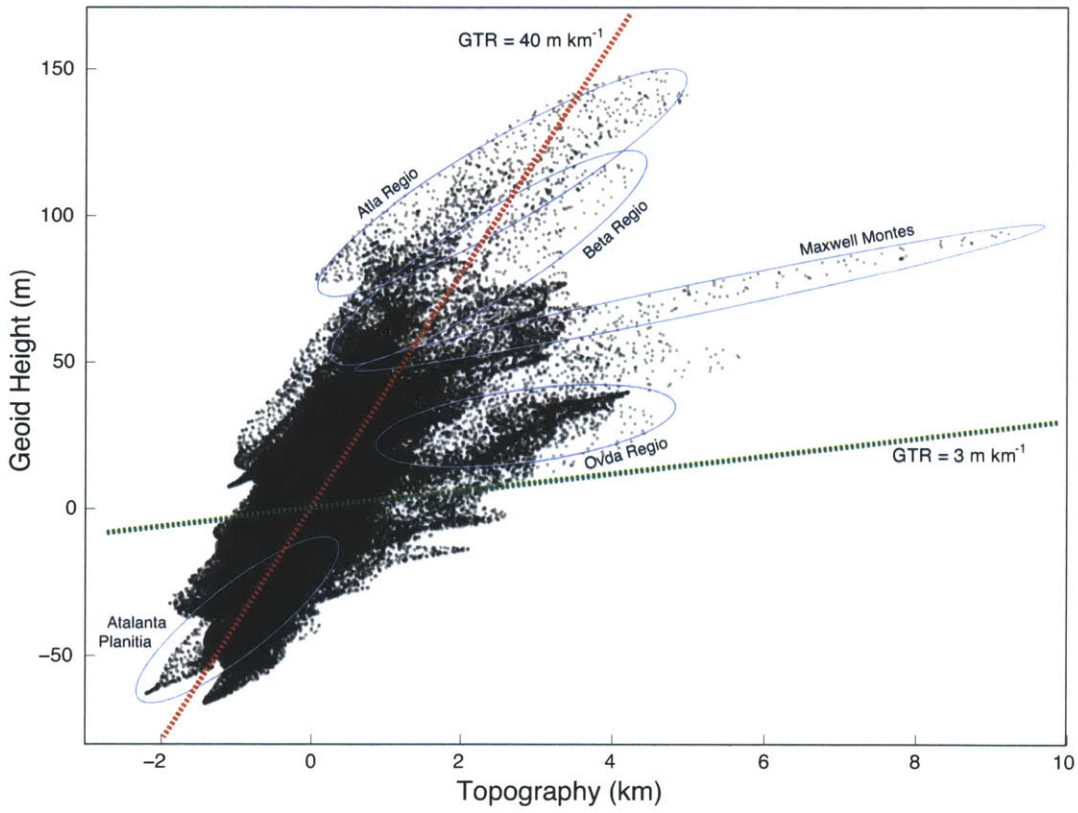

Figure 2-3: Scatter plot of the geoid and topography sampled at 100,000 points on the surface, with two reference slopes. Compensation of topography at the Moho will result in a geoid-to-topography ratio of about 3 m km^{-1} (green line in the plot), and dynamically compensated topography will correspond to higher GTRs.

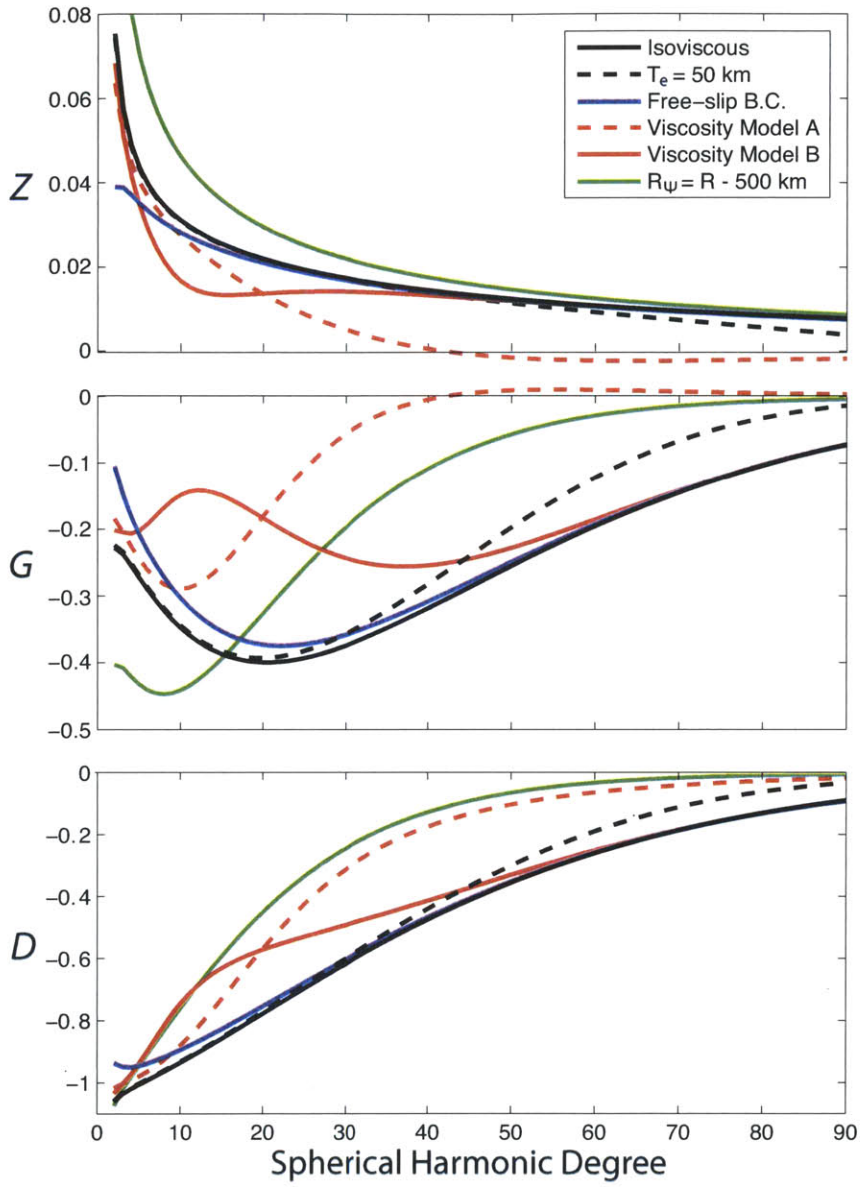

Figure 2-4: Dynamic kernels for five flow scenarios. Unless stated otherwise, models assume an isoviscous mantle loaded at $R_\Psi = R - 250$ km with $T_e = 20$ km and a no-slip surface boundary condition. Viscosity model A incorporates a $10\times$ viscosity increase at a depth of 200 km, and viscosity model B incorporates a $10\times$ viscosity increase at a depth of 400 km.

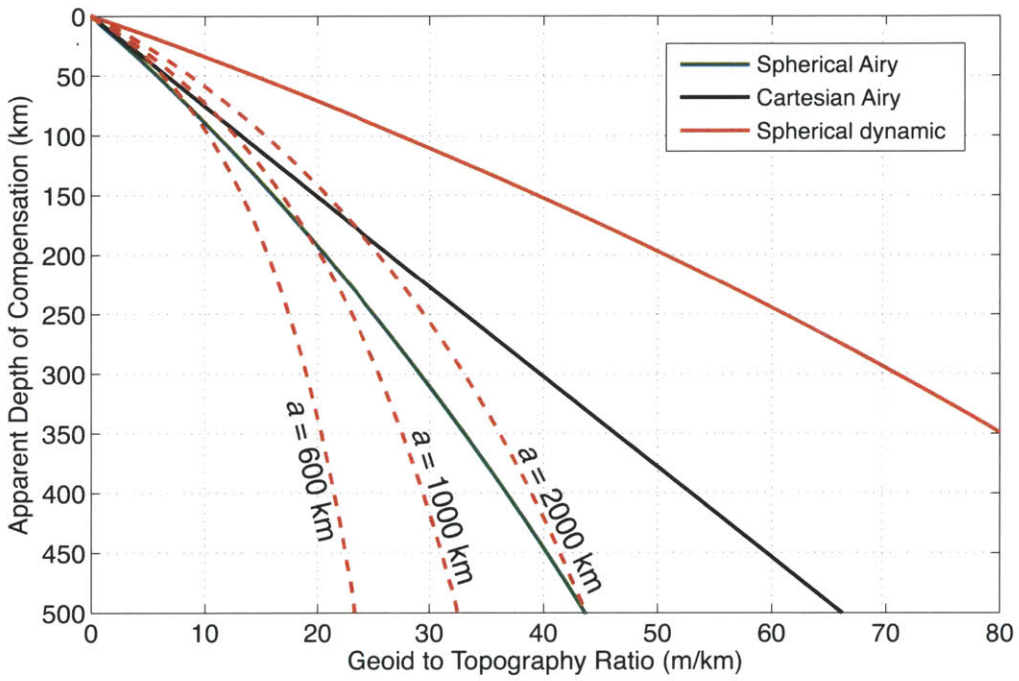

Figure 2-5: Various relationships between apparent depth of compensation and the geoid-to-topography ratio. The traditional Cartesian dipole calculation for Airy isostatic compensation produces the black line, and the spherically corrected calculation produces the green curve (cf. *Wieczorek and Phillips* (1997)). The red curves correspond to dynamic loading calculations, assuming a scale-invariant distribution of Ψ (i.e. $S_{\Psi\Psi}(l) \sim l^{-2}$): the solid line corresponds to a global sampling of topography and the geoid (equation 2-19), and the dotted lines correspond to synthetic models of H and N windowed by the taper in equation 2-13.

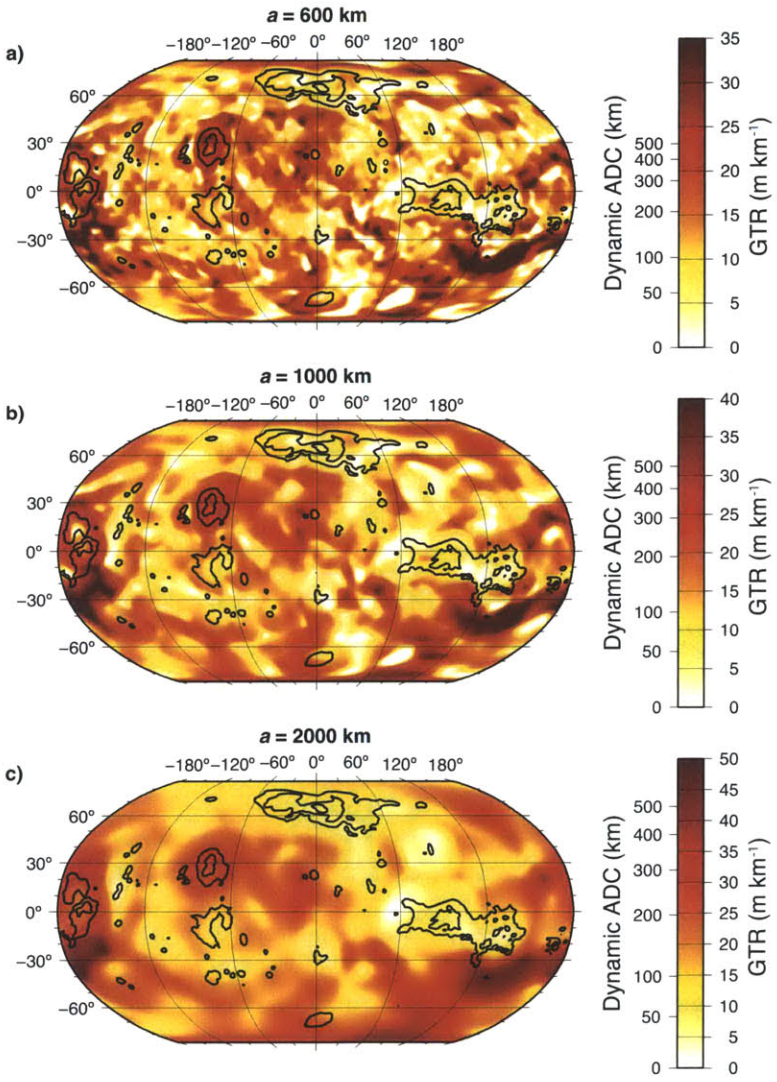

Figure 2-6: Maps of GTRs and Airy compensation depths for various sampling radii a. Black topography contours are overlaid for geographic reference. The poorest resolution in the *MGNP180U* gravity solution is found in the vicinity of (50 °S, 180 °E), so the large GTRs nearby may not have physical significance.

Feature	GTR (a = 600 km)	GTR (a = 1000 km)	GTR (a = 2000 km)	Dynamic ADC (600/1000/2000)	Airy ADC (600/1000/2000)
Alpha Regio	3±2 (5)	4±3 (6)	9±1 (9)	20/30/50	20/30/80
Atalanta Planitia	19±5 (N/A)	20±4 (N/A)	25±3 (N/A)	310/210/200	280/230/270
Atla Regio	18±9 (13)	22±7 (16)	27±4 (23)	270/250/230	250/270/310
Bell Regio	14±7 (10)	15±6 (11)	15±4 (15)	170/130/100	170/160/140
Beta Regio	22±4 (15)	25±3 (21)	28±1 (21)	440/310/240	360/330/320
Dione Regio	13±4 (10)	14±3 (13)	17±2 (20)	150/120/120	150/140/170
Fortuna Tessera	6±5 (12)	7±5 (10)	11±2 (10)	50/50/70	50/60/100
Gula Mons	22±5 (13)	23±5 (16)	24±4 (21)	440/270/190	360/290/260
Imdr Regio	17±4 (12)	19±3 (15)	23±3 (21)	240/190/180	230/220/250
Lada Terra	16±7 (8)	19±6 (11)	24±4 (20)	220/190/190	210/220/260
Lakshmi Planum	8±4 (5)	9±3 (6)	13±1 (12)	60/60/70	70/80/110
Maxwell Montes	6±1 (6)	7±1 (6)	9±1 (8)	40/40/50	50/60/80
Nokomis Montes	20±9 (14)	23±8 (21)	30±4 (31)	210/190/200	190/230/310
Ovda Regio	8±4 (7)	8±3 (7)	9±2 (7)	50/50/50	50/60/80
Phoebe Regio	13±5 (8)	14±4 (11)	16±3 (13)	150/120/110	150/140/150
Tellus Regio	5±3 (1)	5±2 (2)	5±2 (4)	40/30/30	40/40/40
Themis Regio	9±4 (10)	11±3 (12)	15±4 (18)	80/90/100	90/100/140
Thetis Regio	8±7 (5)	9±6 (6)	12±4 (6)	70/70/80	80/80/110
Ulfrun Regio	7±3 (6)	8±3 (5)	10±4 (6)	60/60/60	70/70/90

Figure 2-7: Geoid to topography ratios (m km^{-1}) and apparent depths of compensation (km) for nineteen geographic features on Venus. Each GTR estimate represents the average GTR measured over the region of interest, and the corresponding uncertainty is given by the standard deviation of GTR values within the region. The numbers in parentheses give the GTR localized at the point of highest topography. The corresponding compensation depths are listed for both dynamic and Airy compensation models, using the relationships plotted in Figure 5. Colors correspond to the three physiographic classes described in section 6: red indicates a region with a high GTR, green indicates an intermediate GTR, and blue indicates the lowest GTR, as determined by the a = 2000 km windowing.

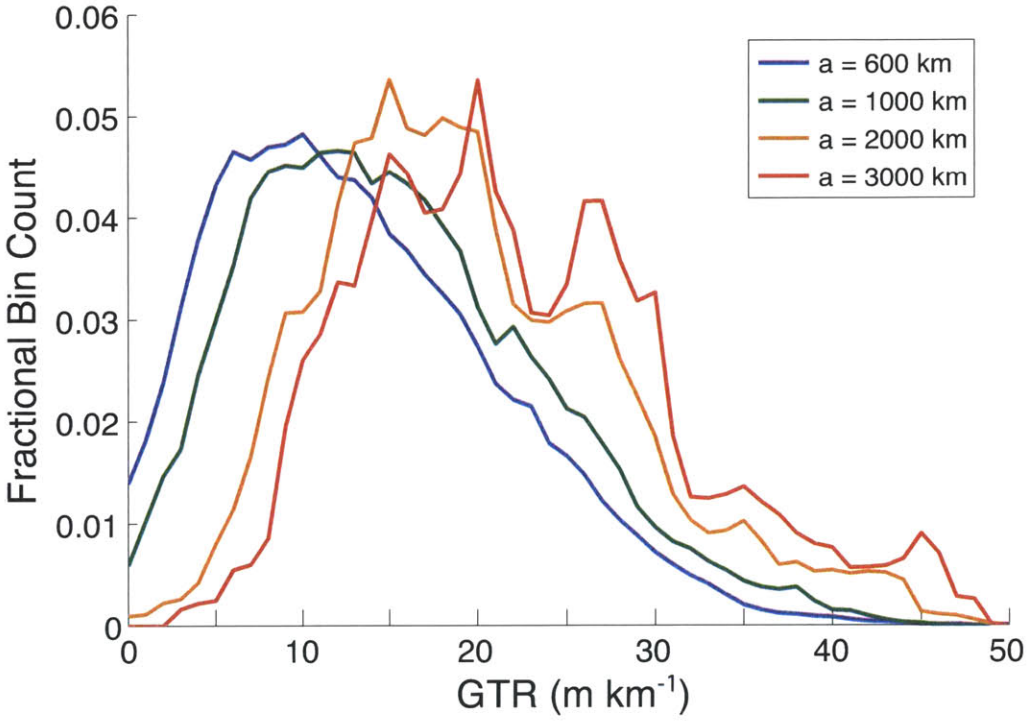

Figure 2-8: Histograms of binned GTR values for different sampling radii.

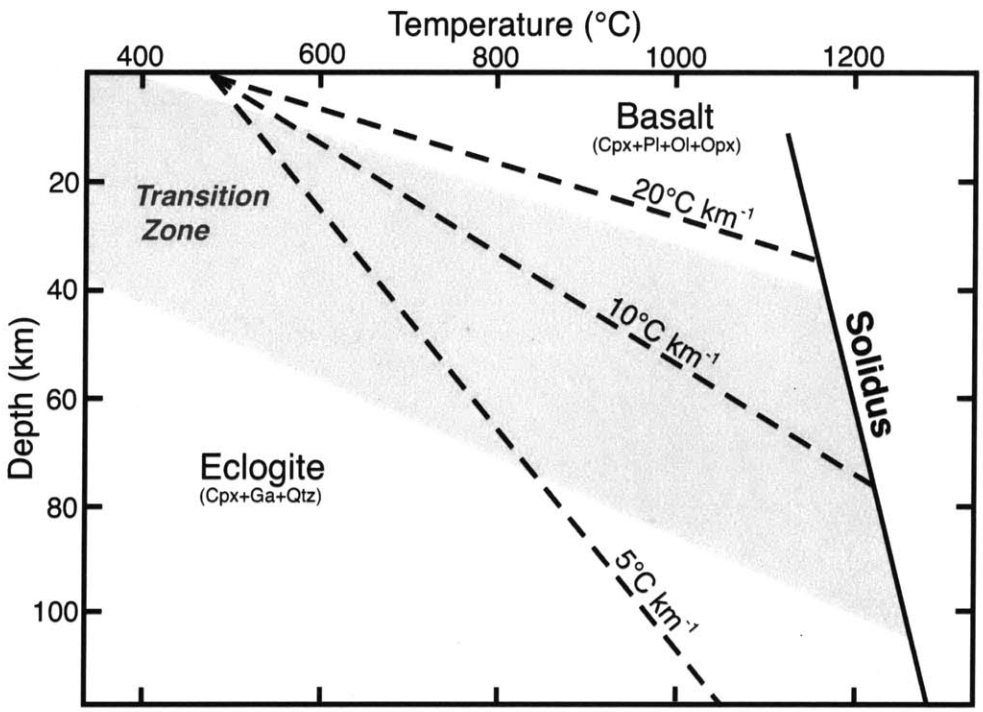

Figure 2-9: Basalt-eclogite phase diagram, adapted after *Ito and Kennedy* (1971) with superimposed geothermal gradients.

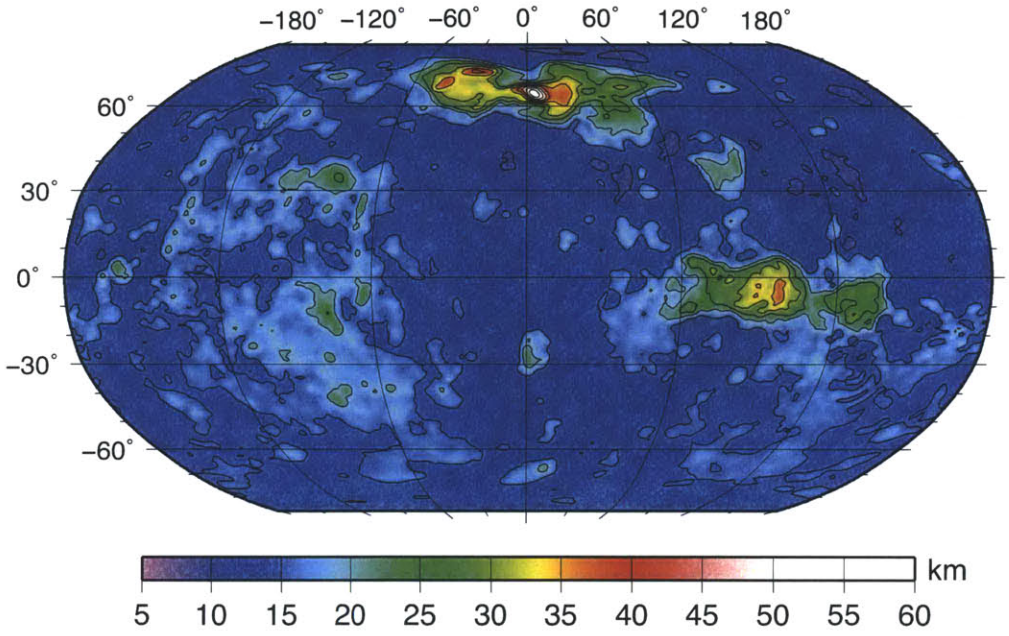

Figure 2-10: Crustal thickness map (in km) for a mean crustal thickness of 15 km and a mantle load depth of 250 km. Contour spacing is 5 km.

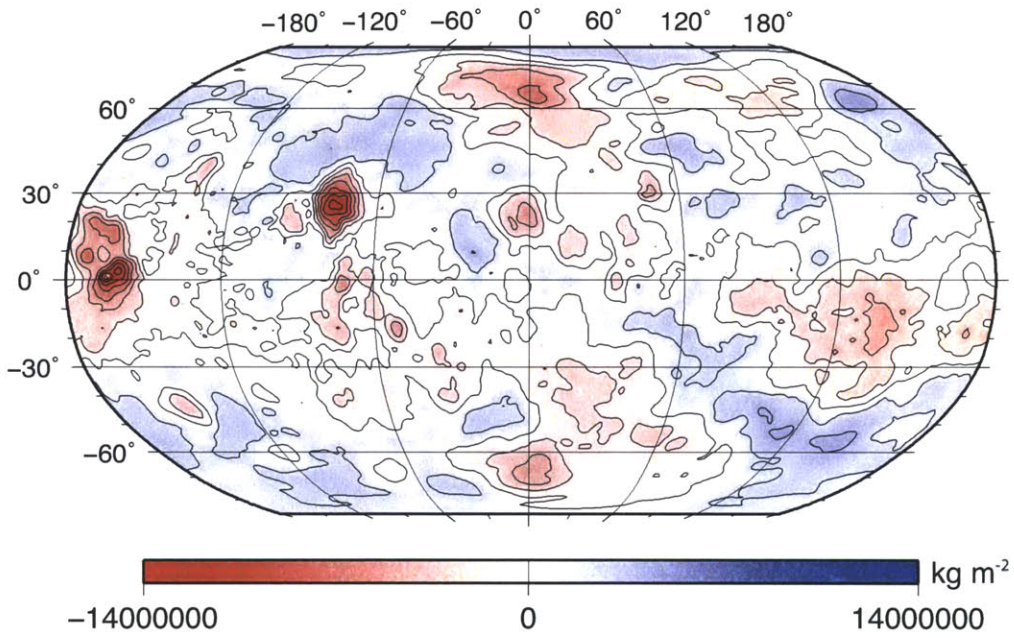

Figure 2-11: Mantle load distribution (in units of kg m^{-3}) for a mean crustal thickness of 15 km and a mantle load depth of 250 km. Warm colors indicate a mass deficit in the mantle and positive buoyancy; cool colors indicate mass excess and negative buoyancy. Contour spacing is 2×10^6 kg m^{-2}.

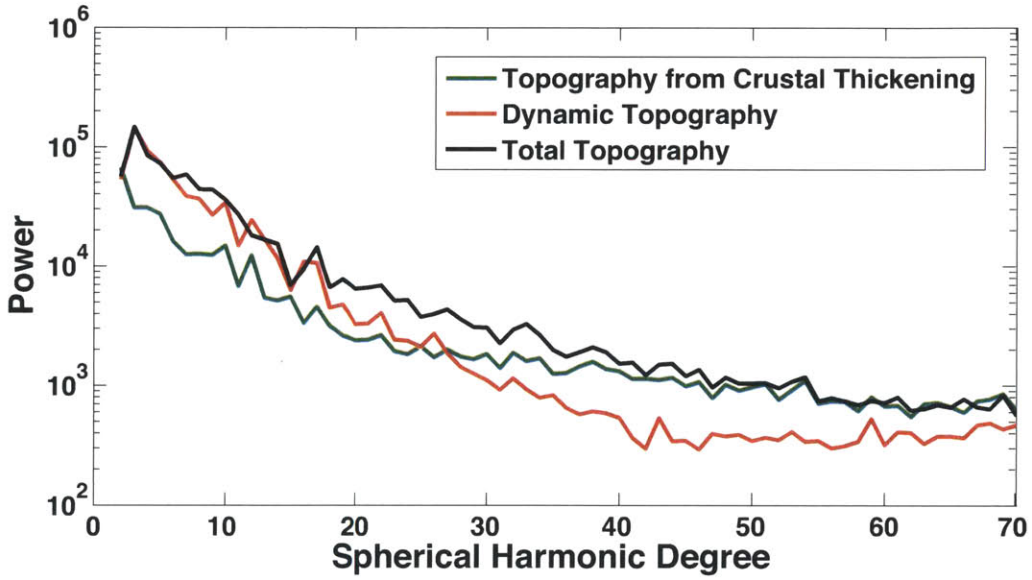

Figure 2-12: Power spectrum for topography, along with the components of topography compensated by crustal thickening (green) and dynamic support (red). Long-wavelength topography is dominated by dynamic loading, while crustal thickening largely compensates short-wavelength features.

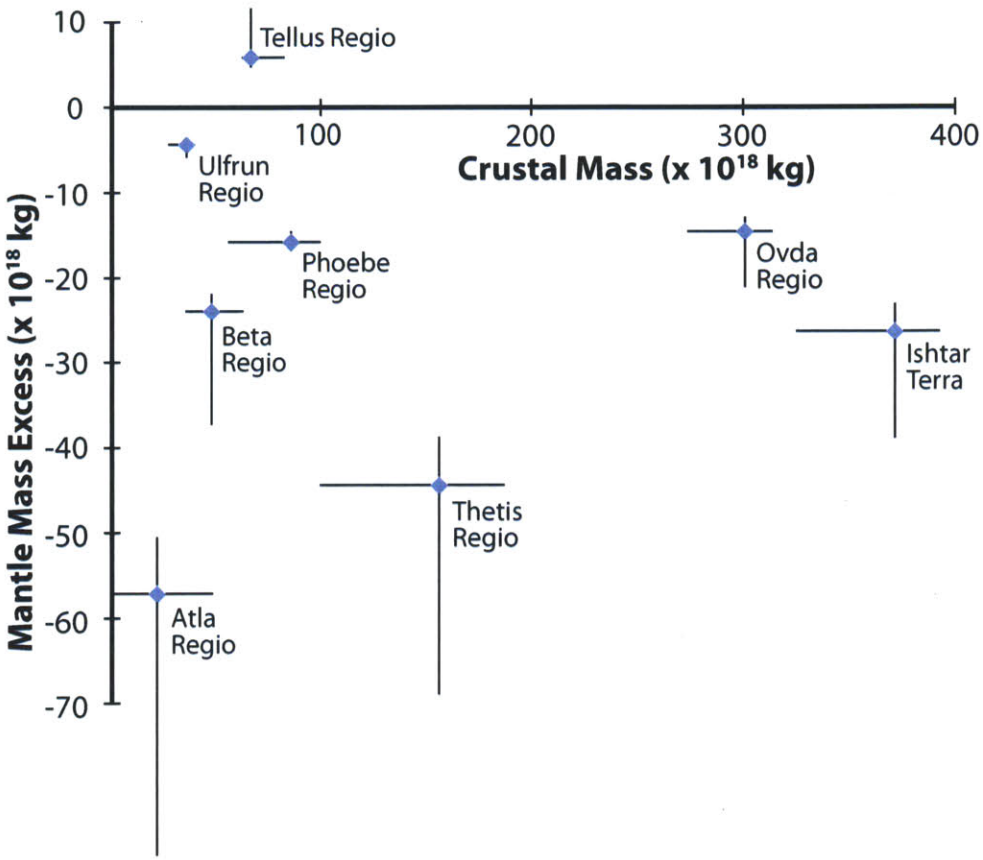

Figure 2-13: Total crustal mass and anomalous mantle mass for selected topographic regions. Crustal mass is measured as the accumulated mass in excess of the mass of a comparably sized region with mean crustal thickness. Error bars represent the distribution of mass estimates for a range of model parameters.

Chapter 3

Support of Surface Topography on Mercury from MESSENGER Gravity and Topography

3.1 Introduction

As an end-member terrestrial body in terms of its composition and dynamics (*Chapman et al.*, 1988), Mercury is a convenient laboratory for studying the formation and evolution of Earth-like planets. Mercury's large core and small silicate portion makes it unique among the terrestrial bodies in the solar system (*Smith et al.*, 2012), but prior to the orbital insertion of NASA's MErcury Surface, Space ENvironment, GEochemistry, and Ranging (MESSENGER) spacecraft (*Santo et al.*, 2001) the evolution history of Mercury's crust and mantle and the mechanisms of topographic support were largely unknown. The gravity and topography data returned by MESSENGER provide a powerful tool for interrogating Mercury's interior. A planet's gravity field is a function of the density distribution inside a planet, and while inversion of a gravity field is non-unique (i.e. a variety of mass distributions can potentially produce the same gravity field) we can characterize a planet's interior by making some simplifying assumptions. The topography associated with various isostatic, dynamic, and flexural compensation scenarios can be theoretically quantified as

well (*Wieczorek*, 2007). A comparison of gravity and topography, along with the length scale dependence of this comparison, consequently improves our knowledge of Mercury's crust and mantle.

Gravity/topography admittances and correlations have been successfully employed in studies pertaining to the Earth (*Forsyth*, 1985; *Watts*, 2001; *McKenzie*, 2003), the Moon (*Wieczorek and Phillips*, 1997; *Wieczorek*, 2013), Venus (*McKenzie*, 1994; *Simons et al.*, 1997; *James et al.*, 2013), and Mars (*McGovern et al.*, 2002; *Wieczorek and Zuber*, 2004; *Belleguic et al.*, 2005). In this paper we perform the first such spectral analysis of gravity and topography on Mercury, although data limitations restrict our analysis to Mercury's northern hemisphere. The results of our spectral analysis motivate a dual inversion of gravity and topography in which we solve for crustal thickness and dynamic mantle flow. Finally, we perform viscous flow calculations for a compositionally stratified mantle, and from that analysis we will address implications for Mercury's structure and evolution, using observations of Mercury's geology and geochemistry as additional constraints.

3.2 Data

The Mercury Laser Altimeter (MLA) (*Cavanaugh et al.*, 2007) onboard the MESSENGER spacecraft is collecting measurements of Mercury's topographic shape $H(\Omega)$ ("topography"), where $\Omega \in (\theta, \phi)$ represents position on the surface of a sphere (figure 3-1a). In conjunction with images from the Mercury Dual Imaging System (MDIS), MLA topography has allowed scientists to characterize geographical provinces (*Zuber et al.*, 2012). Perhaps the most distinctive physiographic feature on Mercury's surface is the Caloris basin, the youngest large impact basin on the planet (*Spudis and Guest*, 1988; *Head et al.*, 2007; *Murchie et al.*, 2008). The basin is filled with smooth volcanic plains, called the Caloris interior plains (CIP), which were visible in camera images prior to MLA measurements. While basin interiors typically feature low-lying topography, MLA confirmed the existence of high long-wavelength topography in parts of the CIP; this long-wavelength topography came as a surprise to many planetary scientists, as evidenced by the hesitancy with which the initial stereo-derived topography results had been presented (*Oberst et al.*,

2010). Caloris basin is surrounded by additional volcanic plains, the circum-Caloris plains (CCP). Parts of the CCP are associated with a hummocky "Odin-type" formation (*Denevi et al.*, 2013). The origin of the CCP is unresolved: color spectra of the smooth plains and the morphology of the Odin-type formation seem to suggest that the CCP is related to impact ejecta, but size-frequency cratering distributions imply that the CCP is younger than the Caloris impact event and therefore volcanic in origin.

The other major volcanic province on Mercury is the northern volcanic plains (NVP). These smooth plains contain a number of wrinkle ridges, which indicate a compressional tectonic environment (*Head et al.*, 2011). The NVP consists mostly of low-lying terrain, but it contains one domical topographic swell at 68 °N, 32 °E, informally known as the "northern rise". The northern rise is not associated with substantially thickened crust or fold and thrust belts (*Smith et al.*, 2012). MLA profiles reveal that ghost craters on the flanks of the northern rise have tilts that roughly match regional topographic slopes, indicating that the northern rise was uplifted at some point after the formation of the NVP (*Klimczak et al.*, 2012; *Zuber et al.*, 2012).

The remainder of the planet is largely characterized by heavily cratered terrain (HCT), and is generally older than the smooth volcanic plains (*Spudis and Guest*, 1988). What we are calling "HCT" contains in reality a diversity of landforms including pockets of smooth volcanic plains, low-reflectance material, and intermediate terrain (*Denevi et al.*, 2009), although most of these features exist at length scales too small for spatio-spectral analysis given the current gravity field resolution. Long-wavelength topography in the HCT is dominated by a number of quasi-linear rises that are associated with thickened crust and are bordered in places by fold and thrust belts (*Zuber et al.*, 2012). However, at least one rise on the periphery of the HCT, the Budh-Sobkou rise at 130 °W, 30 °N, has a more circular shape, similar to the northern rise.

Radio tracking (*Srinivasan et al.*, 2007) is providing information on the free-air gravity anomaly $G(\Omega)$ (figure 3-1b). These data are mostly limited to the northern hemisphere because of MESSENGER's highly eccentric orbit and mid-latitude northern hemisphere periapsis. The $grvfld.MSGR130802.L50$ gravity field of Mercury includes spherical harmonic coefficients out to degree and order 50, but the power of the error surpasses the

signal power above l=48, so we regard this as the nominal resolution of the gravity field. The topography coefficients $fitswp2013\_125$ from MLA are known to a much greater precision, and the topography uncertainty in the northern hemisphere is considered negligible relative to gravity uncertainty. We neglect the degree-1 coefficients of topography (which give the center of mass, center of figure offset) and the degree-2 coefficients of both gravity and topography, since Mercury's tides and possible history of despinning complicate the interpretation of these terms.

Since gravity/topography comparisons on Mercury are limited by the precision of the gravity field, it is imperative to thoroughly quantify the uncertainties in the gravity field using the associated covariance matrix (see Appendix A). We performed eigenvalue decomposition on the full gravity covariance matrix, and we used the first one hundred eigenvectors to produce many random realizations of error (we assumed no error in topography). These random errors were applied to the nominal gravity data and localized with Slepian tapers in order to find the resulting distribution of admittances. We multiplied the nominal errors by a factor of ten to ensure that we do not underestimate the true error.

3.3 Constraints on interior structure

Flyby encounters of Mercury by the Mariner 10 spacecraft revealed a high bulk density and moment of inertia (*Anderson et al.*, 1987) that indicate the presence of a large metallic core (*Solomon*, 1976). Mercury's distance from Earth and proximity to the Sun limit the effectiveness of Earth-based observation, but radar measurements of the forced physical libration in longitude have constrained the moment of inertia of Mercury's solid outer shell (*Margot et al.*, 2007, 2012). The C_{20} and C_{22} components of the gravity field recovered by MESSENGER complemented the existing libration data to constrain the depth of Mercury's liquid core boundary to about 400 km (*Smith et al.*, 2012).

Mercury's surface displays pervasive volcanism, particularly in the northern hemisphere (*Denevi et al.*, 2009). Diffuse flood volcanism, eroded flow channels and a dearth of volcanic edifices point to low magma viscosities (*Byrne et al.*, 2013), which likely result from high degrees of partial melting of the mantle at high temperatures. Major element

abundances inferred from MESSENGERs X-Ray Spectrometer (XRS) and Gamma-Ray Spectrometer (GRS) (*Peplowski et al.*, 2012; *Evans et al.*, 2012) are intermediate between low-Fe basaltic and komatiitic compositions (*Nittler et al.*, 2011; *Charlier et al.*, 2013; *Weider and Nittler*, 2013). These compositions are largely comparable to that of a high-degree melt of enstatite chondrite material, albeit with higher Fe/Si (*Weider et al.*, 2012). Mercury's surface as a whole has lower Al and Ca concentrations than are observed on the Moon, which indicate that Mercury has not retained a flotation crust (*Weider and Nittler*, 2013), but rather has experienced multiple stages of melting and differentiation (*Brown and Elkins-Tanton*, 2009; *Charlier et al.*, 2013).

Mercury's HCT generally has higher Mg/Si, S/Si, and Ca/Si, and lower Al/Si than the younger volcanic plains (*Weider et al.*, 2012). The CIP and the NVP have similar elemental abundances, but the CCP are more similar to the HCT than to the smooth volcanic plains (*Weider and Nittler*, 2013). The CIP and NVP likely crystalized from a mantle source that was more evolved than the source of the HCT, consistent with the relative ages of these terrains (*Weider et al.*, 2012). However, the mantle from which melts were derived cannot have been globally homogeneous, and must have been comprised of at least two different compositional groups (*Charlier et al.*, 2013).

Sulfur abundance 10 times higher that of Earth or the Moon and relatively low Fe abundance indicate that Mercury likely formed in a highly reducing environment (*Nittler et al.*, 2011), which may have allowed for partitioning of S and Si into Mercury's core. In a core of Fe-S-Si composition, a solid FeS layer may form at the top of the core under the right conditions. Orbital parameters are also consistent with but do not demand the existence of such a high-density, solid FeS layer underneath the mantle (*Smith et al.*, 2012; *Hauck et al.*, 2013). With or without this layer the silicate portion of Mercury is thinner than was thought prior to MESSENGER.

3.4 Spatio-spectral localization of gravity and topography

3.4.1 Single Slepian tapers

For the sake of mathematical convenience, topography and gravity were analyzed using their respective spherical harmonic coefficients. For example, Mercury's topography $H(\Omega)$ can be decomposed into weighted a sum of spherical harmonic functions:

$$H(\Omega) = \sum_{l=0}^{\infty} \sum_{m=-l}^{l} H_{lm} Y_{lm}(\Omega), \tag{3.1}$$

and conversely,

$$H_{lm} = \frac{1}{4\pi} \iint_{\Omega} H(\Omega) Y_{lm}(\Omega) d\Omega, \tag{3.2}$$

where Y_{lm} is the 4π normalized spherical harmonic function at degree l and order m, and where negative orders correspond to sine terms.

The free-air gravity anomaly $G(\Omega)$ can be similarly decomposed into its spherical harmonic coefficients G_{lm}. The cross-power spectrum of H and G is defined as the degree-wise sum over the product of H_{lm} and G_{lm}:

$$S_l^{HG} = \sum_{m=-l}^{l} H_{lm} G_{lm}. \tag{3.3}$$

Similarly, the power spectra of H and G are, respectively:

$$S_l^{HH} = \sum_{m=-l}^{l} H_{lm}^2, \tag{3.4}$$

and

$$S_l^{GG} = \sum_{m=-l}^{l} G_{lm}^2. \tag{3.5}$$

The wavelength-dependent ratio of gravity over topography, called the admittance spectrum Z_l, is a diagnostic tool for studying the subsurface of a planet. The observed admittance function can be expressed in terms of power and cross-power spectra:

$$Z_l = \frac{S_l^{HG}}{S_l^{HH}}. \tag{3.6}$$

Another useful quantity is the correlation of gravity and topography, γ_l:

$$\gamma_l = \frac{S_l^{HG}}{\sqrt{S_l^{HH} S_l^{GG}}}. \tag{3.7}$$

Admittances and correlations can be used to distinguish between different mechanisms of supporting surface topography, such as crustal thickness variations, dynamic flow or elastic stresses (e.g., *Forsyth*, 1985; *Richards and Hager*, 1984; *McGovern et al.*, 2002). We want to calculate spectra rather than scalar quantities because these compensation mechanisms often operate at different length scales. We also want to study the spatial variation of these mechanisms, so it is necessary to restrict analysis to a subsection of the sphere. Such localization can be accomplished using Slepian tapers, which maximize the concentration of a spherical function's energy within a region while minimizing the extent to which data at a particular degree is contaminated by data at other degrees (aka "spectral leakage") (cf. *Dahlen and Simons*, 2008).

There is a fundamental tradeoff between spatial localization and spectral fidelity, which depends on the chosen taper bandwidth; a larger bandwidth allows for a more narrowly-windowed data taper, but a smaller bandwidth reduces spectral leakage. Slepian tapers restrict spectral leakage to plus or minus the size of the bandwidth. For our analyses we chose tapers with an 8-degree bandwidth, since this allows us to study the topographic swells that roughly correspond to spherical harmonic degree 10. The resulting localization is imperfect: the first zonal taper for a polar cap concentrates 41% of the total energy within 10° of the center and 90% of the energy within 20° of the center.

In order to get an initial sense for the spatial variation in admittance and coherence, we apply a single zonal taper to the topography and gravity field of Mercury over a latitude/longitude grid. The results are shown in figure 3-2 for spherical harmonic degrees 10, 15 and 20. The hue of the color map represents the localized admittance, while the lightness represents the correlation of gravity and topography. The two most prominent regions of high admittance appear to coincide with domical topographic rises: the northern rise at

(68 °N, 32 °E), and the Budh-Sobkou rise at (130 °W, 30 °N). High admittances are also observed at the north end of the Caloris swell (160 °E, 40 °N), albeit with poor correlation. Large sections of Caloris basin have poor correlations of gravity and topography and/or negative admittances.

3.4.2 Arbitrarily-shaped regions

In order to study geographical regions of arbitrary shape and to quantify uncertainty, we perform multi-taper analysis of gravity and topography. Following the theory of *Dahlen and Simons* (2008), a series of orthogonal Slepian tapers can be calculated so as to maximize energy within in a desired region. We retain only the tapers that localize >80% of their energy within the region.

We partition the northern hemisphere of Mercury into three physiographic regions: the NVP, the Caloris plains (including both the interior and exterior plains), and the HCT, which we define as the remaining area north of 30 °S. The normalized taper energy for each region is plotted in figure 3-3. For a taper bandwidth of 8 degrees, there are 2 tapers well localized to the NVP, 7 tapers well localized to the Caloris plains, and 32 well localized to the HCT. Since the NVP and Caloris plains are not very large relative to the size of the degree 8 tapers, the chosen tapers do not perfectly follow the boundaries of the provinces. The spatio-spectral tapers covering the NVP are relatively insensitive to the northeast section of the plains. In each region the taper is most sensitive to data at the center of the regions, and consequently our analysis of Caloris is more sensitive to the CIP than it is to the CCP.

3.4.3 Uncertainty quantification

We calculate uncertainties in an admittance spectrum as a combination of measurement error and variance among tapered admittances. We produce noisy realizations of the admittance using the gravity covariance matrix from a previous gravity solution (Appendix A), and the variance of these noisy spectra gives us the associated admittance uncertainty. The other source of uncertainty arises from the fact that we have only a single realization

of gravity and topography in a given region. *Wieczorek and Phillips* (1997) show that gravity/topography ratios can be interpreted as a sum of spectrally-weighted admittances, and tapered admittance estimates are similarly a convolution of admittances within the bandwidth of the taper due to spectral leakage. Since theoretical admittances typically vary with spherical harmonic degree the observed admittance spectrum is dependent on the amplitude of topography at different length scales, and any data taper will variably sample a function at different spherical harmonic degrees. Orthogonal Slepian tapers offer nearly independent estimates of gravity and topography spectra within a desired region, so the tapered variance can be estimated with the variance among tapers divided by the total number of tapers (*Wieczorek and Simons*, 2007). Quantifying the effect of this variance for a single taper is more tedious: we estimated single-taper variance by generating many synthetic topography fields with power spectra matching Mercury's power spectrum. We then created synthetic gravity fields by multiplying a range of admittance spectra proportional to $l^{-0.5}$ with topography. We applied single Slepian tapers to the north poles of these synthetic topography and gravity fields and calculated the resulting admittances. We then determined the range of admittances that could produce the observed localized admittance within a confidence interval.

Admittances for the NVP, the Caloris plains, the HCT, and the northern rise are plotted in figures 3-4, 3-5 and 3-6. Theoretical admittance curves from the theory in Appendix B are plotted in blue over the observed spectra. Figure 3-4 compares the admittances spectra for apparent compensation depths, assuming an Airy compensation model. Figure 3-5 shows flexural top-loading admittances for various elastic thicknesses T_e, and figure 3-6 shows admittances for flexural bottom loading. None of these models fit a compensation mechanism well at all wavelengths, but the lower degrees (l<15) have relatively high admittances, which correspond to either greater compensation depths or larger values of T_e. Correlations of gravity and topography (figure 3-7) are significantly less than one almost everywhere on the planet, although the northern rise at low degrees is a notable exception.

3.5 Deep compensation of topography

3.5.1 Viscous flow in a chemically-homogeneous mantle

We have considered case of bottom loading in the context of Airy isostatic compensation, but at depths sufficiently greater than the brittle-ductile transition it is more physically appropriate to consider dynamic flow than Airy isostasy. Incompressible Newtonian flow in a viscous shell can be analytically determined by propagating velocity and stress boundary conditions through the interior of the body (*Hager and Clayton*, 1989). A no-slip boundary condition is appropriate under the assumption that the surface does not participate in mantle flow. We chose a free-slip boundary condition at the liquid core boundary, although other authors have investigated flow with a fixed lower boundary condition (e.g., *Michel et al.*, 2013). The effect of a fixed lower core boundary is to restrict flow and increase relaxation times.

Our model predicts the distribution of flow that results from a mass sheet perturbation Ψ at a radial position R_Ψ in the interior (see appendices B and C of *James et al.* (2013)). A step-wise viscosity structure can be incorporated into the model by combining the appropriate propagator matrices. The amplitude of the mass anomaly can be used along with solutions for the displacements on the upper and lower flow boundaries to forward model the surface geoid and gravity. The degree-dependent admittance spectrum can then be found by dividing surface gravity by the upper boundary perturbation amplitude. The reference viscosity that we choose for our model affects only the velocity solutions, and does not change the interface displacements. Admittance solutions are therefore only dependent on the relative changes in viscosity. The viscosity profiles used in our models are given in Table 3-1.

The l=10 admittance kernels in figure 3-8 show the ratio of gravity over topography as a function of the loading depth $R - R_\Psi$ and the displacement kernel gives the amplitude of surface displacement scaled by Ψ/ρ_c. In order to match the l=10 admittance at the northern rise, a dynamic loading depth of $R - R_\Psi$ = 300 km would be required for an isoviscous profile. The existence of a high-viscosity lithosphere does not appreciably change the modeled admittance spectrum. The presence of an asthenosphere (taken here to mean a

low-viscosity zone in the mid-mantle) can serve to decouple flow from the surface, and reduces the admittances. The effect of a lithosphere or asthenosphere is most pronounced at high degrees, when the length scale of flow is comparable to the thickness of the anomalous viscosity layer. The presence of a high viscosity layer at the base of the mantle decreases the admittances dramatically. For a viscosity more than a factor of two higher than the overlying mantle, a 100 mGal km^{-1} admittance at l=10 cannot be reproduced. A deep high viscosity layer effectively couples the driving load Ψ to the lower boundary rather than the surface, which allows the gravity from Ψ to counteract the gravity from topography. If the viscosity of the deep layer is decreased, on the other hand, admittances are increased slightly over the isoviscous case.

The range of admittance values and the imperfect correlation of gravity and topography over much of the surface (figure 3-2) indicate that the topography of Mercury cannot be compensated by a single mechanism; the observed gravity and topography can be better fit by assuming the existence of at least two superimposed compensation mechanisms (*Banerdt*, 1986; *Herrick and Phillips*, 1992; *James et al.*, 2013). This type of dual inversion has two constraints at each spherical harmonic degree and order: the model must match the observed gravity, and the radial stress on the surface must counteract the weight of topography. There are also two unknowns at each spherical harmonic degree and order: the coefficients for Moho relief and the coefficients for a dynamic load. The dual inversion for crustal thickness and dynamic flow pressure is shown in figure 3-9 for a crustal density ρ_c=3200 kg m^{-3}, a crust-mantle density contrast $\Delta\rho$=200 kg m^{-3}, a mean crustal thickness of 40 km, and a mantle load depth of 350 km. Since dynamic topography is associated with larger gravity anomalies than crustal isostasy, the inverted solution for dynamic flow pressure looks similar to Mercury's geoid. In contrast, the crustal thickness variations contribute more to topographic relief than to the gravity field, so the crustal thickness solution looks similar to Mercury's topography.

3.5.2 Two-layered viscous relaxation

Although the viscous flow models described previously are instructive, the nature of viscous flow inside Mercury will be different if compositional layering exists above the 400-km-deep liquid core boundary: any flow across a boundary with an intrinsic density difference will produce an additional load driving flow (see Appendix C). We will look at one particular scenario in which flow is driven by the relaxation of a perturbed FeS/silicate boundary (illustrated in figure 3-10). We assume a 100-km-thick layer of solid FeS below 300-km depth with a mantle/FeS density contrast of 1000 kg m^{-3} and an FeS/liquid core density contrast of 1300 kg m^{-3}. We assume a rigid lithosphere thickness of 200 km (in which viscosities are one hundredfold larger than lower mantle viscosities), and we use the *Smith et al.* (2012) uniform crust and mantle densities of 3200 kg m^{-3} and 3400 kg m^{-3}, respectively. The viscous relaxation of a single layer may be simply characterized as an exponential function with time, due to the fact that flow velocity is proportional to the interface displacements. Two-layered relaxation is more complicated, but the theory in Appendix C allows us to calculate the instantaneous radial velocities of the surface, the compositional layer, and the liquid core boundary. We use discrete time steps to calculate new interface amplitudes using these velocity solutions, and we use an adaptive time stepping algorithm to propagate the solution forward in time.

Our semi-analytical calculation begins with no surface topography and an FeS layer of laterally-varying thickness. We do this by prescribing harmonic relief at the mantle-FeS interface, along with similar relief of opposite sign at the FeS-liquid core interface (i.e. the interior is initially in a state of isostasy). When an initial FeS/silicate perturbation starts to relax, it causes surface topography to grow over regions of thickening FeS and to subside over regions of thinning FeS. After surface relief reaches maximum amplitude, continued flow will cause the topography to viscously relax. The duration of topographic uplift and the characteristic time of decay (defined to be the time at which topography relaxes to one tenth of its maximum height) are dependent on the viscosities of the FeS layer and the silicate lower mantle. The admittance and displacement kernels associated with two-layered relaxation vary with time, but these kernels eventually converge to the

values associated with chemically homogeneous models (figure 3-8), where the loading depth $R - R_\Psi$ equals the depth of the mantle-FeS interface.

In analytical solutions of viscous relaxation in an infinite halfspace, the longest wavelengths of surface relief relax most quickly (*Haskell*, 1936). On a sphere with a thin mantle, however, large aspect ratios of flow may allow viscous relaxation to persist over geological time even at the longest wavelengths (as shown in figure 3-11 for l=6). A viscosity of 10^{24} Pa-s in the lower mantle results in an uplift time of hundreds of millions of years and a relaxation time in the billions of years. It should be noted that this viscosity is still larger than the viscosity range of 10^{19}-10^{21} assumed by *Michel et al.* (2013). As discussed later in section 5.5, for the range of viscosity assumed by *Michel et al.* (2013), l=6 topographic features would effectively relax on timescales of 0.1-10 million years.

3.6 Discussion

3.6.1 Deep compensation of topography

The weight of topography on Mercury is likely supported by some combination of four compensation mechanisms: Moho relief, dynamic flow, flexure, and lateral density variations. The relative importance of the first three mechanisms is illustrated in figure 3-12, which shows ranges of topographic power plausibly produced by each mechanism. If H^c is the portion of topography compensated by Moho relief ("crustally-compensated topography"), we can define the power of crustally-compensated topography:

$$S_l^{cc} = \sum_{m=-l}^{l} (H_{lm}^c)^2 \tag{3.8}$$

Similarly, if H^d is the portion of topography compensated by dynamic flow ("dynamic topography") and H^f is the portion of topography supported by elastic flexure ("flexural topography"), then the respective power spectra are S_l^{dd} and S_l^{ff}. We can determine the expected ranges of these power spectra for reasonable parameter ranges, along with the power spectra for the associated geoids (figure 3-12). Topography compensated by the Moho is assumed to be between 0.5 and 1.1 times the power of topography; the magnitude

of dynamic loading is assumed to be between 0.01 and 1.0 times the load of topography, with a loading depth of 300 km; and the power range for flexurally-supported topography assumes top loading with λ=1.5-5 (as defined in Appendix B) on a plate of thickness $20 < T_e < 100$ km.

We see in figure 3-12 that crustal compensation of topography is expected to be prominent for almost all degrees less than l=30. However, the highest admittances shown in figure 3-4 are too large to plausibly result from crustal thickness variations (some apparent compensation depths are greater than 100 km). While flexural support and deep-seated flow are associated with high admittances, flexure does not contribute substantially to topography at the lowest spherical harmonic degrees for the parameter ranges given above. This leaves dynamic flow as the most likely compensation mechanism of the domical, high-admittance topographic swells.

3.6.2 Crustal thickness

The crustal thickness map in figure 3-9a marks an improvement over the crustal thickness map of *Smith et al.* (2012) in that it goes out to spherical harmonic degree 50 (Smith et al. used a degree and order 20 gravity field). The power of Mercury's crustal thickness (roughly proportional to S^{cc}, which is plotted in figure 3-12) is spectrally quite flat: while topography and crustal thickness on planets are typically red-shifted (*Turcotte*, 1987; *Wieczorek*, 2007) the power spectrum of S^{cc} has a relatively shallow exponential fit of $l^{-0.8}$. The cause of this shallow spectral slope remains an open question; since most of Mercury's crustal thickness variations result from volcanism and cratering, it is possible that the manifestation of these processes are somehow biased towards short length scales relative to similar processes on Venus, the Earth and Mars. Alternatively, subdued crustal thickness variations at long wavelengths may possibly result from lower crustal flow, although more work is needed to quantify this scenario.. A non-negativity constraint requires that the mean thickness be larger than 38 km. For a mantle that extends to 300-km depth, this means that the volume of crustal material is at least 14% of Mercury's silicate volume.

The quasi-linear rises are associated with crustal thickening, and are often sub-isostatic,

with crustal roots deeper than is necessary to support the weight of topography. In many cases the crust under these rises is more than twice as thick as crust in the surrounding terrain. The origin of the thickened crust is uncertain but may plausibly correspond to either tectonic shortening, high degrees of mantle melting, or ancient basin rims. Crustal thicknesses under the rises are much too large to be explained by radial contraction of no more than a few kilometers, so a tectonic origin of the rises may instead result from surface tractions over a convective downwelling. Alternatively, large volumes of melt may have resulted from the linear upwellings that are predicted by convection models (*King*, 2008; *Michel et al.*, 2013). Active upwellings would impose upward pressure on the surface and low-density residuum would be expected at the location of an extinct upwelling due to the high degrees of melting, so in any case we would expect to observe large admittances and good correlation of gravity and topography at the site of an upwelling (this does not generally appear to be the case in figure 3-2.) Finally, it is reasonable to assume that some long-wavelength structures are remnants of ancient impact basins given the ubiquity of large impacts during the period of heavy bombardment. Such an ancient origin for the quasi-linear rises may be confirmed or rejected by future measurements of crater floor tilts (cf. *Balcerski et al.*, 2012).

The thinnest crust is found at the center of Caloris basin, which is consistent with mantle excavation during the Caloris impact event. We also observe a "collar" of thickened crust surrounding the central thinned crust, a feature that is common in lunar basins (*Neumann et al.*, 1996). Crustal collars in impact basins are thought to form through the inward collapse of the transient cavity (*Melosh et al.*, 2013), so the 1000-km diameter of the collar in Caloris basin can be considered a lower bound on the transient cavity diameter.

3.6.3 Interpretation of admittance and coherence

We can quantitatively interpret the localized admittance and coherence spectra in terms of shallow and deep topographic compensation. If we represent the observed planetary shape as a superposition of crustally-compensated topography H^c and deeply-compensated topography H^d, the total topographic power can be expressed in terms of the power of H^c,

the power of H^d, and the cross-power of H^c and H^d:

$$S_l^{HH} = \sum_m \left(H_{lm}^c + H_{lm}^d\right)^2 = S_l^{cc} + S_l^{dd} + 2S_l^{cd}. \tag{3.9}$$

Gravity power and cross-power spectra can be represented similarly if the crustal admittance spectrum Z^c and the admittances for dynamic flow Z^d are known:

$$S_l^{GG} = \sum_m \left(Z_l^c H_{lm}^c + Z_l^d H_{lm}^d\right)^2 = \left(Z_l^c\right)^2 S_l^{cc} + \left(Z_l^d\right)^2 S_l^{dd} + 2Z_l^c Z_l^d S_l^{cd} \tag{3.10}$$

and

$$S_l^{HG} = \sum_m \left(H_{lm}^c + H_{lm}^d\right)\left(Z_l^c H_{lm}^c + Z_l^d H_{lm}^d\right) = Z_l^c S_l^{cc} + Z_l^d S_l^{dd} + \left(Z_l^c + Z_l^d\right) S_l^{cd}. \tag{3.11}$$

Equations 3-7, 3-8 and 3-9 can, along with the observed admittance spectrum and gravity/topography correlations, be used to find the power and cross-power of H^c and H^d:

$$\frac{1}{S_l^{HH}} \begin{bmatrix} S_l^{cc} \\ S_l^{dd} \\ S_l^{cd} \end{bmatrix} = \begin{bmatrix} 1 & 1 & 2 \\ \left(Z_l^c\right)^2 & \left(Z_l^d\right)^2 & 2Z_l^c Z_l^d \\ Z_l^c & Z_l^d & Z_l^c + Z_l^d \end{bmatrix}^{-1} \begin{bmatrix} 1 \\ \left(\frac{Z_l}{\gamma_l}\right)^2 \\ Z_l \end{bmatrix} \tag{3.12}$$

We can then calculate the ratio of deep topography power over crustal topography power, S_l^{dd}/S_l^{cc}, and the correlation of compensation sources, $S_l^{cd}(S_l^{cc}S_l^{dd})^{1/2}$ (see Table 3-2).

A majority of long-wavelength topography in the NVP is deeply supported. Ratios of S_l^{dd}/S_l^{cc} are lower but non-negligible in the Caloris plains and the HCT, suggesting that dynamic topography is present and partially obscured by crustal thickness variations. The spherical functions H^c and H^d are relatively uncorrelated in the NVP, but are negatively correlated in the Caloris plains and the HCT; in other words, thick crust is more likely to be associated with negative (downward) buoyancy in the mantle, and vice versa. The existence of positive mantle mass anomalies under the quasi-linear topographic rises is particularly

intriguing, and as explained in section 5.2 it is opposite of what would have been expected if the rises had formed over a convective upwelling.

3.6.4 What exactly is the deep mass anomaly?

As shown in figure 3-13, dynamic topography may be similar in amplitude to crustally-supported topography at low spherical harmonic degrees. The power of dynamic topography drops considerably at degrees higher than l=13,, so dynamic flow (or at least the surface expression thereof) exists mostly at Cartesian wavelengths larger than $2\pi R/\sqrt{l(l+1)} \approx$1100 km. The large amplitudes of dynamic topography as well as the bias of dynamic topography towards long wavelengths validates, in retrospect, our assumption that the high admittance topography results from dynamic flow rather than flexural support.

Although dynamic flow apparently exists and produces significant surface topography, we have not specified the source of the driving mass load Ψ. There are two likely possibilities: perturbations of an interface between layers of different density, or lateral density variations. In the two-layered flow scenario explored in section 4.2, this excess mass comes from relief on the interface between the mantle and the solid FeS layer, and about 5 km of interface relief is required to produce one kilometer of surface topography. We haven't identified the cause of this initial perturbation, but impact events and deposition/delamination of FeS are possibilities.

An alternative source of mass anomalies in Mercury's deep interior is lateral density variations that can result either from thermal expansion/contraction or from compositional variations. For lateral temperature variations of up to 300 °C, thermal density anomalies in the mantle may be expected to be on the order of $\Delta\rho = \alpha\Delta T\rho_0 = 30$ kg m^{-3}. Compositional variations may be of similar magnitude: if a primitive upper mantle is approximated as an assemblage of 90% forsterite (ρ = 3220 kg m^{-3}) and 10% pyrope (ρ = 3600 kg m^{-3}), a chemically depleted residuum of pure forsterite would have a density 38 kg m^{-3} lower than the primitive mantle. *Jordan* (1978) similarly concluded that density variations due to differing degrees of partial melting might be about $\pm$1% in the Earth. We can approximate the dynamic flow field due to a density anomaly distributed through the mantle by the

integrating the flow solutions for a range of loading depths, and this flow field can be incorporated into a dual inversion similar to the one shown in figure 3-9. Low mantle densities correlate well with the CIP (figure 3-14), which could signify chemical depletion associated with the basin-forming impact event or the subsequent volcanism (*Watters et al.*, 2009). The differential density of 40 kg m^{-3} over the entire depth of the mantle is at the high end of plausible density contrasts that might be expected due to either thermal or chemical heterogeneity, so we consider deep interface perturbation to be the most likely source of dynamic flow.

3.6.5 Timescales of relaxation

Figure 3-11 gives the relaxation timescales associated with mantle and FeS viscosities, and we see that a viscosity of more than 10^{23} Pa-s in the lower mantle is required in order to maintain surface topography over billions of years. If the actual mantle viscosities are lower, we may be confronted with a paradox: we observe long-lived, deeply-supported topography on Mercury even though relaxation of such topography should be relatively rapid. Mantle convection may be possible on Mercury at lower viscosities (*Michel et al.*, 2013), and such convection can produce significant amplitudes of dynamic topography under the right conditions, but it may not be reasonable to assume that mantle convection patterns can be stationary for billions of years. Additionally, the length scales of thermally-driven convection do not match the observed length scales of dynamic topography: convection cells in a 366-km-thick mantle have Cartesian wavelengths of 650-750 km, which correspond to spherical harmonic degrees 20-23 (*Michel et al.*, 2013).

As an alternative explanation for prolonged support of topography, we note that large aspect ratios of flow (i.e. a narrower range of depths over which flow occurs) and/or compositional layering in the mantle may significantly increase the timescales of viscous flow. Our flow calculations include an elastic shell that can grow with time, but the effect of a time-evolving elastic lithosphere had very little effect on the final topography (supporting $<1\%$ of final topography in all cases). A potentially more important effect, which we did not adequately model, was the effect of a growing lithosphere on the nature of mantle flow

in Mercury. The rigid lithosphere does not participate in viscous flow due to its high yield strength, and a young lithosphere will grow as it cools from above. This narrowing of depths over which flow occurs will restrict relaxation. Thus, it may be possible to "freeze" topographic swells in place (although this word is a misnomer: all flow is in the solid state, and no phase transitions occur). In a 1-D thermal diffusion problem with a diffusivity of κ = 10^{-6} m^2s^{-1}, the characteristic length scale of thermal diffusion $2\sqrt{\pi\kappa t}$ reaches 200 km at about 100 My. This timescale may be consistent with the time at which a long-wavelength topographic swell may have begun to subside (cf. figure 3-11).

Finally, we note that Mercury's viscosity profile is a function of mantle temperature and composition, both of which have likely changed over the course of Mercury's history. Secular cooling of Mercury is evidenced by the contractional faulting associated with a shrinking planetary radius (*Solomon*, 1976). The large volume of crustal material on Mercury (at least 14% of Mercury's silicate volume by our analysis) indicates extensive chemical depletion of the underlying mantle. The effect of such changes in temperature and composition depend on knowledge of Mercury's mantle composition, but these factors may plausibly cause an increase in mantle viscosity over Mercury's history. While our semi-analytical two-layered flow calculation successfully incorporates a time-varying elastic lithosphere, models with time-varying viscosity profiles were numerically unstable. Future studies of viscous flow under evolving conditions may require revised computational methods.

3.7 Conclusions

The large admittances (figures 3-4, 3-5, and 3-6) and the good correlation of gravity and topography (figure 3-7) associated with Mercury's northern rise and Budh-Sobkou rise below spherical harmonic degree 15 point to the existence of deep-seated dynamic flow and/or flexural top-loading. The large amplitudes of high-admittance topography as well as the tendency of such topography to be most pronounced at length scales greater than 1100 km favors the prominence of dynamic topography over flexurally-supported topography. Dynamic flow beneath the domical topographic swells is driven by mass deficits at 300-400-km depth that may result from either lateral density variations or from relief on a

compositional boundary, such as the interface between the mantle and the proposed solid FeS layer. We favor the latter interpretation given the amplitudes of the inferred anomalies.

Our two-layered flow model demonstrates a process by which topography can grow and be sustained over geological time scales, roughly matching the timeline inferred from ghost crater tilts. The duration of two-layered dynamic flow is only marginally sensitive to the viscosity of the lower FeS layer. A lower mantle viscosity of more than 10^{23} Pa-s is required in order to maintain long wavelength topography for billions of years, although the requisite viscosity may be lower if Mercury's silicate shell is compositionally stratified.

A dual inversion of gravity and topography produces a crustal thickness map, and this analysis places a lower bound of 38 km on the mean thickness. Quasi-linear rises are found to be associated with thickened crust, often more than double the crustal thickness in the surrounding terrain. Crustal thickness in the HCT is correlated with positive mass anomalies in the mantle, contrary to what may have been expected if the topographic rises had formed via extensive mantle melting. An analysis of regionally-localized admittance and coherence reveals that dynamic topography accounts for most of the l=10 topography in the NVP. Dynamic topography elsewhere on the planet is largely obscured by crustal thickness variations.

Table 3.1: Profiles of relative viscosity. Case #1: High viscosity at depth; Case #2: Isoviscous; Case #3: Low viscosity at depth.

Depths	**Case #1**	**Case #2**	**Case #3**
0 - 50 km	1	1	10
50 - 300 km	1	1	1
300 - 400 km	10	1	0.1

Table 3.2: Ratios and correlations of crustally-supported topography vs. deeply -supported topography.

	Spherical harmonic degree	S_l^{dd}/S_l^{cc}	**Correlation of** H^c **and** H^d
NVP	10	1.74	-0.34
	15	0.62	0.09
Caloris Plains	10	0.56	-0.55
	15	0.26	-0.39
HCT	10	0.32	-0.22
	15	0.19	-0.31

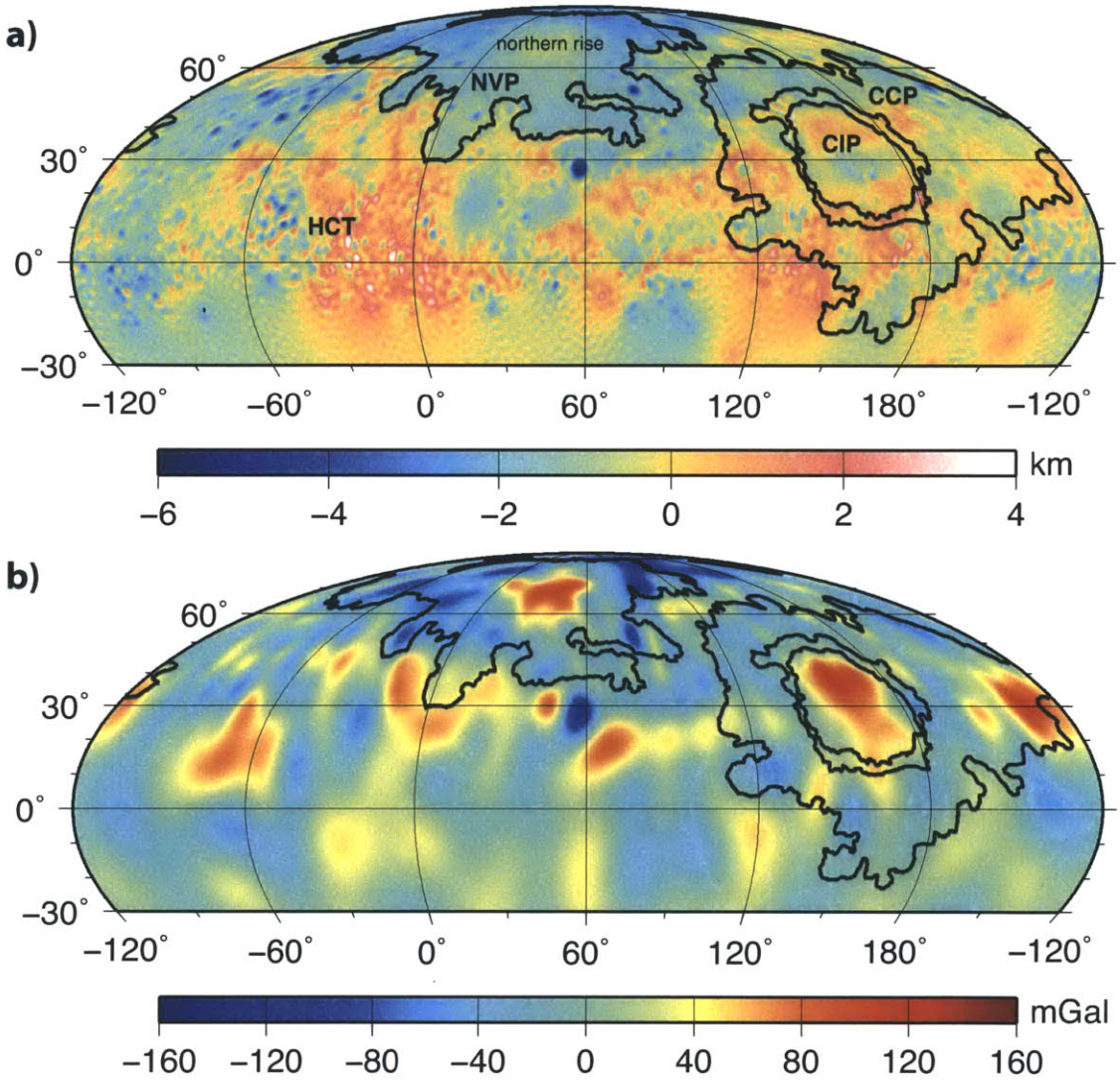

Figure 3-1: a) MLA topography and b) free air gravity recovered by MESSENGER. Labeled regions are: heavily cratered terrain (HCT), northern volcanic plains (NVP), the northern rise, Caloris interior plains (CIP), and circum-Caloris plains (CCP)

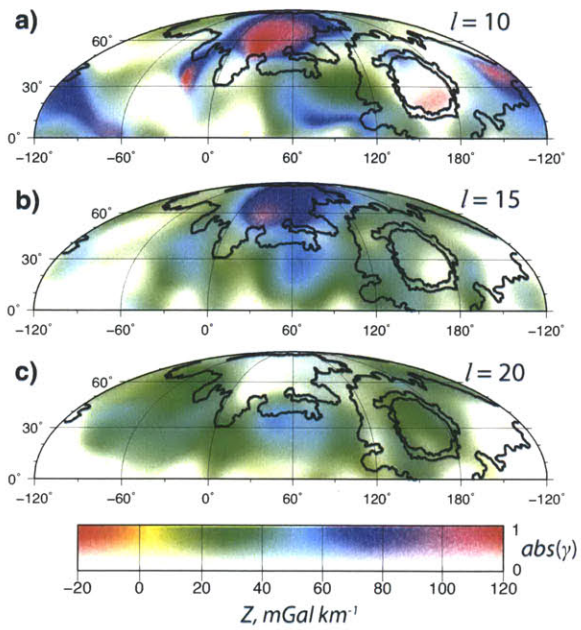

Figure 3-2: Single-taper admittance and coherence values for spherical harmonic degrees 10, 15, and 20.

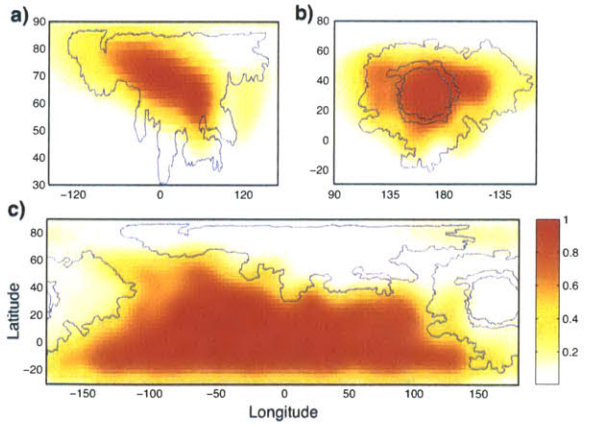

Figure 3-3: Normalized taper energy for a) the northern volcanic plains, b) the Caloris plains, and c) the heavily cratered terrain.

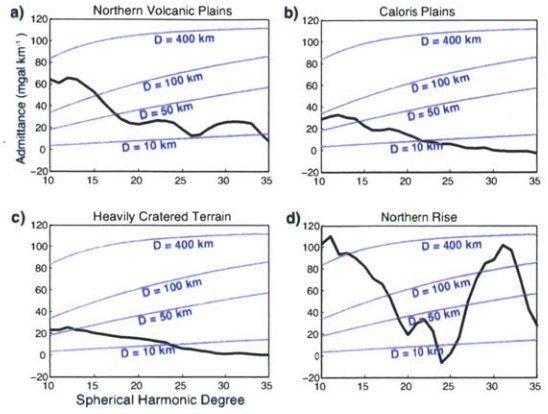

Figure 3-4: Observed admittances (black) with error ranges and theoretical admittances for Airy compensation depths (blue).

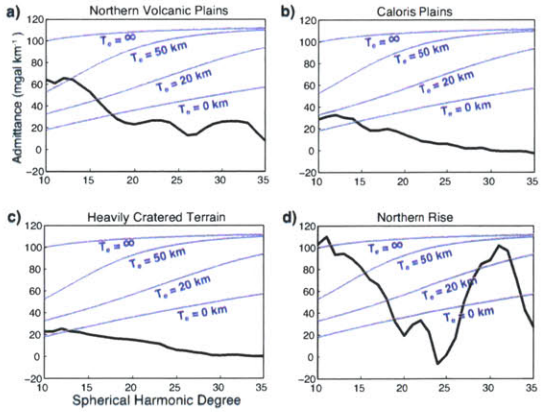

Figure 3-5: Observed admittances (black) with error ranges and theoretical top-loading admittances for various elastic plate thicknesses (blue).

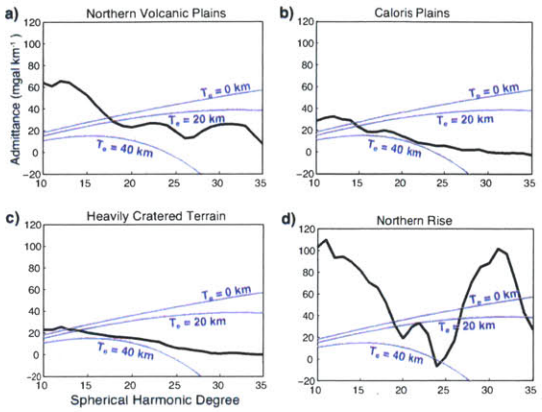

Figure 3-6: Observed admittances (black) with error ranges and theoretical bottom-loading admittances for various elastic plate thicknesses (blue).

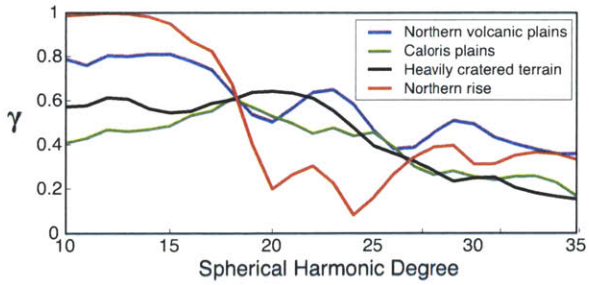

Figure 3-7: Correlation of gravity and topography.

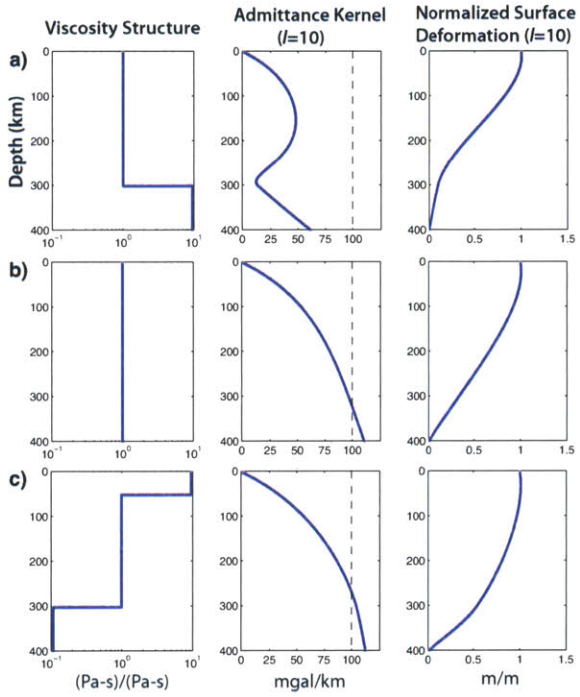

Figure 3-8: Admittance and surface displacement kernels for different viscosity profiles.

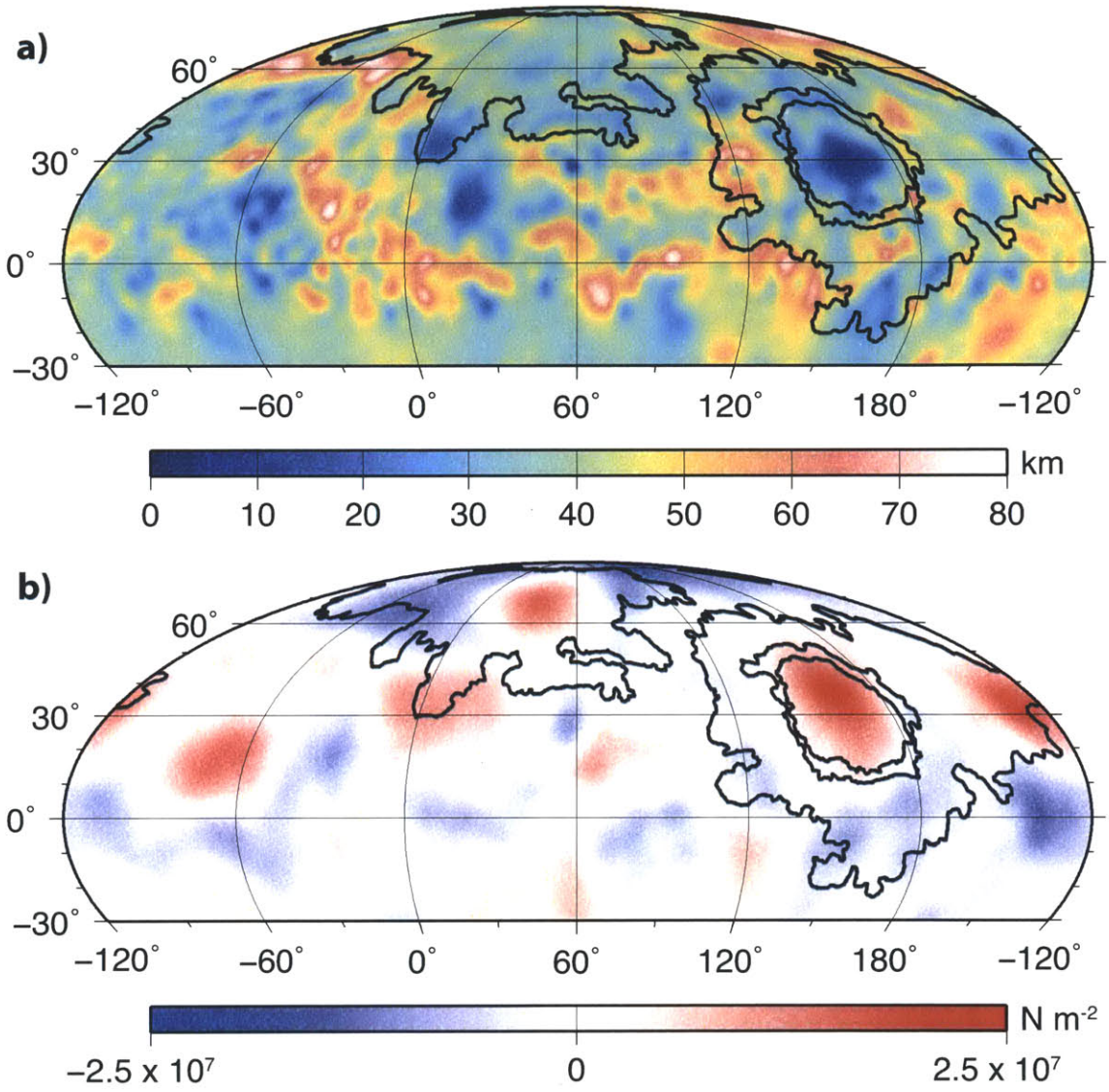

Figure 3-9: Two-layered model of topographic compensation: (a) crustal thickness variations, and (b) Surface pressure from dynamic flow (hot colors indicate upward pressure on the surface).

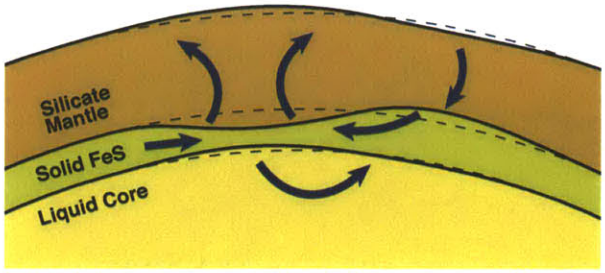

Figure 3-10: Cartoon of the layered relaxation problem in cross-section.

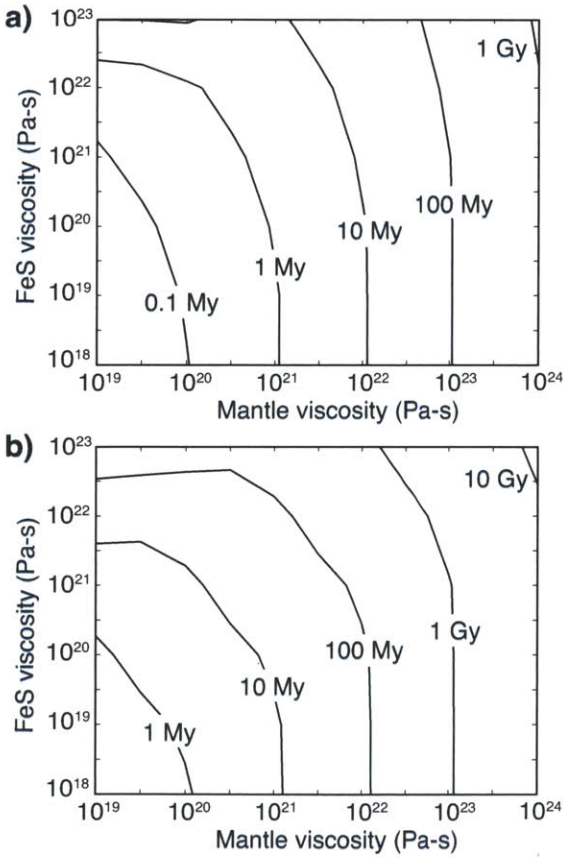

Figure 3-11: (a) Time of maximum topographic height, and (b) timescale of topographic relaxation.

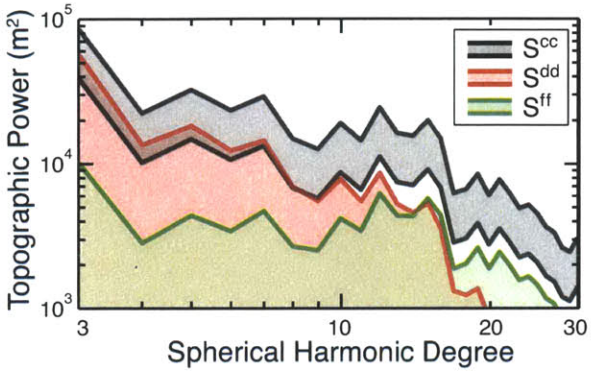

Figure 3-12: The *expected* ranges of topographic power resulting from crustal compensation (black), dynamic flow (red), and flexural support (green), assuming plausible parameter ranges (section 5.1).

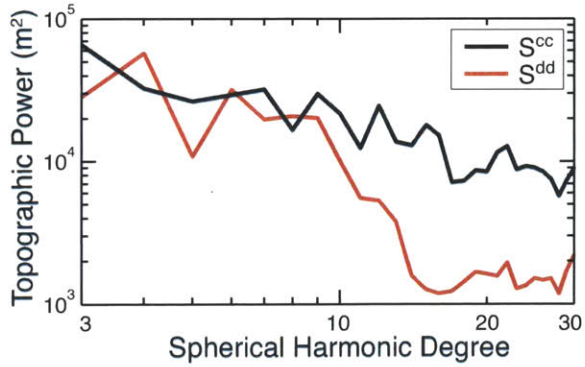

Figure 3-13: Power of crustal topography (black) and dynamic topography (red) resulting from a dual inversion of gravity and topography.

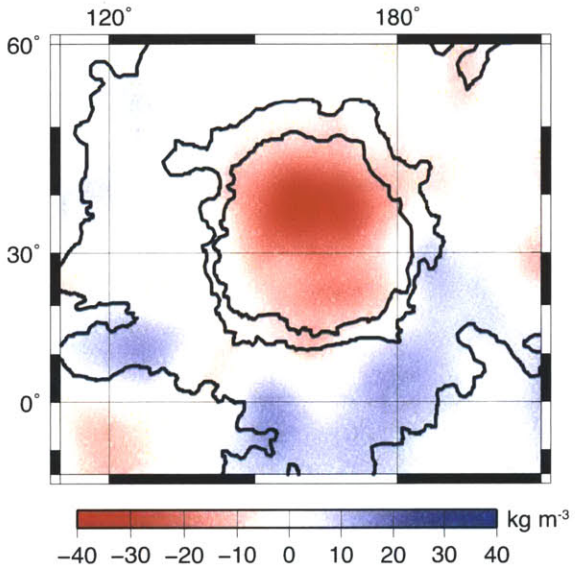

Figure 3-14: Mantle density anomaly in the vicinity of the inner and outer Caloris plains.

Chapter 4

Insights into Lunar Mare Stress States from GRAIL

4.1 Introduction

The type, orientation, spatial distribution and relative timing of tectonic faults reflect the evolution of stresses on the Moon. The state of stress on the Moon at a given time is determined by the physical properties of the elastic lithosphere and by the distribution of loads. Physical properties of the lithosphere are, in turn, dependent on the composition and thermal profile of the lunar interior, and either erupted volcanic material on the surface or relief on the crust-mantle interface can serve as an elastic load. All of these quantities are inter-related; efforts to understand the evolution of the Moon can approach lunar science from multiple angles. Geologic mapping efforts have identified sequences of mare flooding events (*Wilhelms and McCauley*, 1971; *Head et al.*, 1978; *Solomon and Head*, 1980) as well as faulting patterns (*Maxwell et al.*, 1975; *Watters and Johnson*, 2010; *Watters et al.*, 2012). Theoretical models can be constructed to predict stress distributions for a given load (*Brotchie and Sylvester*, 1969; *Solomon and Head*, 1979; *Banerdt et al.*, 1982; *Banerdt*, 1986).

Regions of elevated free-air gravity anomaly, as recovered by the Gravity Recovery and Interior Laboratory (GRAIL) (*Zuber et al.*, 2013a), are common in large lunar basins. Much of the lunar nearside is covered with dense volcanic flows (*Head*, 1976). These

optically dark regions, visible from Earth, are called "maria", the Latin word for "seas" (singular: mare; cf. Figure 1 of *Hiesinger et al.* (2011) for a map of mare extent). Samples returned from the maria by Apollo 11, 12, 14, 15 and 17, as well as by Luna 16, 20 and 24, were basaltic in composition (e.g., *Turkevich*, 1973), in contrast with the largely anorthositic highland crust (*Wood et al.*, 1970; *Metzger et al.*, 1974). Mass concentrations, or "mascons", were observed under several of the nearside maria prior to the Apollo missions (*Muller and Sjogren*, 1968). The gravity anomalies in the vicinity of these mascons typically have a bulls-eye pattern, with rings of low free-air gravity surrounding the high free-air gravity anomalies at the center of the basin. These negative gravity anomaly rings are interpreted to be sub-isostatic crust that helps to support the super-isostatic central region (*Neumann et al.*, 1996; *Andrews-Hanna et al.*, 2013a). The mascons likely form through the viscous and thermal evolution of an impact basin structure (*Melosh et al.*, 2013). After a large impact excavates crust from the basin, inward collapse of a transient cavity creates one or more collars of relatively thickened crust around the basin periphery. Through a combination of isostatic adjustment and thermal contraction, the center of the basin evolves into a state of super-isostasy, characterized by a mantle plug near the surface (*Neumann et al.*, 1996). A later crustal thickness model using gravity from discrete polyhedra had the same interpretation (*Hikida and Wieczorek*, 2007).

Although the Moon is largely tectonically inactive today, a number of compressional and extensional faults are preserved on the surface from early lunar history. Faulting occurs predominantly in the lunar maria, in part due to the connection between mare flooding and local stress states (*Watters and Johnson*, 2010). A number of events have affected stress states in the history of the large lunar maria, including: 1) the preexisting stress state associated with the basin-forming impact event, 2) successive stages of mare eruption, 3) stress release through fault slip, and 4) the thermal and viscous evolution of the lunar lithosphere. The type and spatial distribution of mare faulting provides a record of the stress states at various times in the Moon's history, and as such an analysis of lunar maria stress states constrains the chronology of lunar basin evolution. Of particular use in constraining the interior structure of the Moon is gravity data in conjunction with topography and compositional information. In this paper we use new GRAIL gravity data and LOLA altimetry data

to estimate the magnitude of elastic loads, and we use semi-analytical modeling to calculate the distribution of stresses resulting from these loads. We focus primarily on the maria associated with lunar near-side basins, since these surfaces are generally younger than the highlands (*Wilhelms*, 1987) and roughly correspond to simple axisymmetric loads. We compare the resulting stress distributions to the placement and orientation of lunar faults.

4.2 Gravity and topography

The gravity field of a planetary body affects the trajectory of an orbiting spacecraft, and the line-of-sight spacecraft accelerations measured by radio tracking can be used for the recovery of the gravity field. Lunar gravity fields were recovered using tracking data from some of the earliest orbital spacecraft, including Lunar Orbiter 1-5 (*Lorell and Sjogren*, 1968) and the Apollo 15 and 16 subsatellites (*Sjogren et al.*, 1974). These early lunar gravity data were combined with Clementine tracking data to produce the *GLGM-2* field (*Lemoine et al.*, 1997), and all of these data were combined with tracking of the Lunar Prospector spacecraft to produce the *LP100* gravity field (*Konopliv et al.*, 2001). These tracking data relied on a direct line of sight to the Earth, and consequently the modeled gravity fields from these spacecraft were poorly determined on the far side of the Moon. JAXA's Selenological and Engineering Explorer (SELENE) mission was able to reliably collect far-side gravity data using a relay satellite (*Namiki et al.*, 2009), and the SGM100h gravity field produced by this mission improved the correlation of gravity and topography over the previous gravity models (*Matsumoto et al.*, 2010). The recently concluded GRAIL mission used ranging measurements between twin satellites along with ranging from the Earth-based Deep Space Network to recover a gravity field of unprecedented resolution (*Zuber et al.*, 2013b). We use the *GRGM660PRIM* dataset, which used primary mission data from a 55-km mean orbital altitude to produce spherical harmonic coefficients out to spherical harmonic degree and order 660 (an effective block size of $\pi R/\sqrt{l(l+1)} = 8.2$ km) (*Lemoine et al.*, 2013). Power of the error coefficients surpasses the signal power above spherical harmonic degree 471, and the near-perfect correlation of gravity and topography at spherical harmonic degrees 150-350 speaks to the quality of the data up to these wavelengths. For the length-

scales relevant to lunar basins (wavelength $\approx$ 150-600 km), the ratio of signal power to error power is more than 10^5. Forthcoming gravity models that incorporate extended mission tracking at a mean altitude of 23 km will increase the gravity field resolution further, but primary mission data is of sufficient precision and resolution for the present study.

Some of the best constraints on lunar shape ("topography") come from orbital laser altimetry measurements. The laser altimeters on the payloads of the Apollo 15, 16 and 17 command modules (*Sjogren and Wollenhaupt*, 1973; *Kaula et al.*, 1974) measured spacecraft altitudes above the surface of the Moon over several dozen orbital tracks in the equatorial regions (latitudes inside $\pm 30\,^{\circ}$). Laser shots during these missions had 30-43 km along-track ground spacings and 30 m surface spot sizes. Lunar topography determined by these data had absolute radial uncertainties of over 100 meters due to orbital determination and gravity field uncertainty. Near-global altimetry measurements of the Moon (excluding the poles) were first collected by the Laser Image Detection and Ranging (LIDAR) system onboard the Clementine spacecraft (*Zuber et al.*, 1994). Similar laser altimetry campaigns by the Indian Space Research Organization's Chandrayaan-1 mission (*Kamalakar et al.*, 2005), the SELENE spacecraft (*Araki et al.*, 2009) and the Chinese National Space Administration's Chang'E-1 mission (*Li et al.*, 2010) improved the global coverage of topography. Lunar topography data is currently being collected by the Lunar Orbiter Laser Altimeter (LOLA) onboard the Lunar Reconnaissance Orbiter (LRO) (*Smith et al.*, 2010a), which has thus far accumulated more than six billion laser altimetry measurements in a five-spot pattern. Altimetry measurements by LOLA have an absolute horizontal position accuracy better than 100 meters, and ground-track crossovers (*Mazarico et al.*, 2012) have reduced radial position errors to less than one meter, approaching the nominal instrument precision of 10 cm (*Smith et al.*, 2010b). The *LOLA720_PA* lunar topography model, which we use in this paper, is based primarily on the LOLA altimetry measurements and gives spherical harmonic coefficients out to degree and order 720.

A visual comparison of gravity and topography shows that a number of mascons are bordered by topographic ridges in the maria, which we refer to as "circumferfential ridges" (the traced lines in Figure 4-1). *Neumann et al.* (2013) noted that these ridges are also border the regions of thin crust and uplifted mantle at basin interiors. The circumferential

ridges are interpreted to be contractional tectonic features (*Watters and Johnson*, 2010). While wrinkle ridges and extensional grabens are expected to arise as a result of flexural mare loading, the striking correlation of gravity and tectonics suggests that the mascons are directly or indirectly related to the stress state that caused these tectonic features.

4.3 Geological context

Theoretical models of stress distribution rely on the observable constraints provided by surface tectonics. A number of types of tectonic structures have been classified in the lunar maria (cf. *Watters and Johnson* (2010)). Contractional tectonic features are most commonly manifested in the maria as morphologically complex wrinkle ridges, which form through folding and thrust faulting of stratigraphic layers. Extension in the maria is accommodated through linear and arcuate rilles, which are long narrow depressions typically bounded on two sides by normal faults. Sinuous rilles found in the maria feature similar depressions but are likely to have formed from the collapse of ancient lava channels, and thus are not connected to the local stress state. In order to characterize the evolution of the stress state around a basin, we also need to determine how much of the elastic loading is associated with subsurface loading and how much is associated with mare fill. We therefore would like to know the thickness of the maria at the mascon basins. While gravity is a powerful tool for studying a planet's interior, interpretation of a gravity field is non-unique: a given gravity anomaly can be reproduced by any number of interior mass distributions (*Wieczorek*, 2007). This poses a problem particularly for interpreting the structure of mascon basins, as a high free-air gravity anomaly can be interchangeably modeled as a thick layer of dense mare, a super-isostatic mantle plug, or some combination thereof. In order to separate the effects of mare fill versus a mantle plug, we must rely on additional information from the geological context.

A number of studies have used crater populations to estimate the thickness of basalt flows in the maria. *Hiesinger et al.* (2002) points out that the rims of craters predating a mare flooding event may extrude at the surface if the craters diameters are large relative to the mare flow thickness, and they consequently used kinks in crater size-frequency dis-

tributions to infer representative values for basalt thickness in various maria. In such an analysis there is ambiguity as to whether the depth to the pre-mare basement or merely the depth to a previous basalt layer is being inferred. Other studies have constrained the thickness of the maria using craters that did or did not excavate basement rock beneath the basalt, such as the measurements of basalt thickness at Mare Humorum by *Budney and Lucey* (1998). *Thomson et al.* (2009) took this analysis one step further and investigated the distribution of low-Fe basement material in crater ejecta blankets at Mare Imbrium. The spatial extent of low-Fe material was used to estimate mare thickness relative to the crater depth, and thus *Thomson et al.* (2009) provided a number of precise thickness estimates along with upper bounds and lower bounds. Unfortunately, sparse data is a limitation for crater excavation analysis. Most of the data points provided for Mare Imbrium are located on the basin periphery, and only lower bounds on basalt thickness exist in the central and northern parts of the basin.

The final constraint we have on subsurface stratigraphy comes from the Apollo Lunar Sounder Experiment (ALSE) onboard the Apollo 17 orbital module (*Phillips et al.*, 1973). ALSE used the backscatter arrivals from 60-meter wavelength sounding to identify subsurface reflectors in Mare Serenitatis and Mare Crisium, which were interpreted to be interfaces between basalt layers (*Peeples et al.*, 1978). The ALSE track through Mare Serenitatis and the corresponding reflection profile is shown in Figure 4-2. *Sharpton and Head* (1982) reinterpreted the results of (*Peeples et al.*, 1978) and concluded that the lowermost horizon detected under Mare Serenitatis is the interface between the lowermost mare unit and the underlying basement material. The Lunar Radar Sounder (LRS) onboard SELENE performed a second round of radar-probing experiments in the lunar maria. The higher resolution of LRS measurements made it more sensitive to shallow crustal structure, and two subsurface reflectors were identified at 0.9 and 1.6 km depth in Mare Serenitatis. Detection of these stratigraphic boundaries via radar requires at least two meters of regolith, so periods of quiescence between successive flooding events must have been long enough for space weathering processes to produce this much regolith. This is consistent with the spread of 700 million years in the emplacement ages of these stratigraphic units (*Hiesinger et al.*, 2002).

4.4 Lunar stress states

4.4.1 Regimes of lunar faulting

According to theory by Anderson (*Anderson*, 1951), the style and orientation of faulting is dependent on the principal stress orientation. The principal stresses orientation is the reference frame in which no shear stresses, and the three principal stresses in this orientation are labeled σ_1, σ_2, and σ_3 from most positive to most negative (i.e. σ_1 is most tensile and σ_3 is most compressive). On the surface of a planet, the shear stresses $\sigma_{r\theta}$ and $\sigma_{r\phi}$ are zero, so one principal stress axis must be oriented in the vertical direction and the other two must lie in the plane perpendicular to the first. The vertical stress σ_{rr} is also equal to zero at the surface of the Moon, which has negligible atmospheric overburden.

Therefore, three basic scenarios may characterize the stress tensor at the surface of a planetary body. First, if both of the surface coplanar principal stresses are compressive (i.e. σ_2, $\sigma_3 < 0$), the predominant fault type is thrust faulting, which is characterized by convergent strain in the direction of σ_3 and a fault strike in the direction of σ_2. Thrust faulting on the Moon exists predominantly in the form of morphologically complex wrinkle ridges or in the form of lobate scarps. If both of the surface coplanar stresses are tensile (i.e. σ_1, $\sigma_2 > 0$), extensional faulting occurs. Extension is typically accommodated by normal faults, and these faults often occur in pairs so as to produce long linear or arcuate rilles. The remaining scenario, in which the surface coplanar principal stresses have opposing signs, is strike-slip faulting. While strike slip faults are common on the Earth, with prolific strike-slip faults such as the San Andreas Fault in California, strike slip faulting is noticeably absent on the Moon. This has been attributed to an oversimplification of the Anderson theory of faulting, and the greater surface curvature on the relatively smaller Moon (*Freed et al.*, 2001).

The fact that fault strikes indicate the orientation of principal stresses provides another clue with which we can investigate the history of the lunar stress state. For rotationally symmetric impact basins, we can further simplify the interpretation of the stress state by defining hoop stresses, which are oriented concentrically around the basin, and radial stresses, which are oriented in line with the center of the basin. Radial wrinkle ridges, concen-

tric wrinkle ridges, radial rilles and concentric rilles can be seen in many lunar basins, as shown in Figure 4-2 for southern Mare Serenitatis. While both radial and concentric wrinkle ridges point to a compressive environment, concentric wrinkle ridges result when radial stresses are most compressive, and radial wrinkle ridges indicate that hoop stresses were most compressive. The same applies for the tensile environment inferred from radial and concentric rilles.

4.4.2 Coulomb stress changes

The Mohr-Coulomb failure criterion for a given fault plane dictates that failure will occur when shear stress on the plane is sufficiently large:

$$\tau \geq s - f \cdot \sigma_n \tag{4.1}$$

where s is the intrinsic strength, σ_n is the normal stress on the fault plane, and f is the coefficient of friction. Coulomb stress change is a metric commonly used by the earthquake seismology community to provide information about the likelihood of fault slip associated with an evolving stress state (*Stein*, 1999). It is defined as the change in shear stress plus the coefficient of friction times the normal stress on a fault plane:

$$\Delta\sigma_c = \Delta\tau + f \cdot \Delta\sigma_n. \tag{4.2}$$

Positive normal stress here indicates compression, and a positive Coulomb stress change indicates that the fault has moved closer to satisfying the inequality in equation 4.1 (i.e., failure on the fault). Coulomb stress changes are most commonly used to quantify the change in stress state associated with earthquakes, and have proven to be a useful tool for predicting earthquake aftershocks (*Stein et al.*, 1997; *Freed*, 2005). On the Moon, we can use the Coulomb stress changes associated with incremental changes in the stress field as a tool for assessing the plausibility of faulting associated with an elastic load on the surface. All told, the present-day stress state can be represented as an incremental superposition of

stress contributions from many different events:

$$\sigma_{ijk}^{present} = \Delta\sigma_{ijk}^{basin} + \Delta\sigma_{ijk}^{mare,1} + ... + \Delta\sigma_{ijk}^{mare,n} + \Delta\sigma_{ijk}^{thermal} + \Delta\sigma_{ijk}^{faulting} \quad (4.3)$$

While we may be able to estimate one or more of these stress tensors, the stress state of the lunar surface ultimately depends on the cumulative history represented by all of the terms in this equation.

4.5 Stress calculations

4.5.1 Elastic load inferred from free-air gravity

We can infer the magnitude of an uncompensated load by comparing the observed free-air gravity anomaly to that produced by a state of crustal compensation (Appendix G). The inferred load, given by equation G.7, is a function of free-air gravity g, topography H, and spherical harmonic degree l. Equation G.7 is also dependent on knowledge of internal parameters, including the mean crustal thickness $R - R_W$, the crustal density ρ_c, and the crust-mantle density contrast $\Delta\rho$. The problem setup in Appendix A assumes a constant crustal density, and thus the uncompensated load is effectively located at the depth of the crust-mantle boundary (i.e. the depth of a super-isostatic mantle plug). This is in contrast to a load caused by dense mare fill, which would be primarily at the surface of the planet. As shown in Figure 4-3 for loading depths of 0, 10 and 30 km (black lines), the inferred amplitude of elastic loading is moderately dependent on the depth of loading, resulting in a factor of <2 ambiguity for a range of depths less than 30 km. A 10-km downward continuation of the gravity field from the surface to the crust-mantle interface increases the inferred mass load by 42% relative to a surface load at spherical harmonic degree 30. For the sake of simplicity we calculate the amplitude of elastic loading by interpreting gravity as a load acting at an intermediate depth of 10 km, regardless of whether the load originates from mare fill or from super-isostatic Moho relief.

As a first order approximation, the magnitude of an uncompensated load is proportional to the free-air gravity anomaly in the spatial domain (equation G.8). This approximation

is plotted in Figure 4-3 (sky-blue line), along with loads calculated using the more thorough expression given by equation G.7. In some applications it may be desirable to use equation G.8; in particular, it does not require a spherical harmonic transform, and it does not require assumptions about parameter values. However, we can see in Figure 4-3 that, due to self-gravitational effects, an elastic load calculated by simple scaling of the free-air gravity anomaly will overestimate the true amplitude of the load at low spherical harmonic degrees. Additionally, if the loading depth is greater than about 20 km, the true load will be underestimated at higher spherical harmonic degrees ($20<l<60$) by a Cartesian approximation.

Because of the upward continuation term, errors will become magnified in the solution at short wavelengths. As a result, estimates of deep loading using equation G.7 begin to diverge above spherical harmonic degree 90, about the same resolution to which a crustal thickness map can be reliably produced by gravity inversion (*Wieczorek*, 2013). Since we have also neglected finite-amplitude corrections for gravity (*Wieczorek and Phillips*, 1998), this will also cause interpretation of this analysis to become unreliable above spherical harmonic degree 90. Another caveat for inferring elastic loads from gravity is that the isostatic residual may not completely result from uncompensated topography alone. For example, the gravity anomaly associated with a deep mantle density anomaly in the lunar interior, such as that associated with depleted mantle residuum (e.g., *Phillips et al.*, 1990), may be mistakenly interpreted as evidence of a flexural load. The interpretation of free-air gravity will be especially tricky if deep mantle heterogeneities are associated with basin-forming impact events (e.g., *Watters et al.*, 2009)).

Figure 4-4 plots the azimuthally-averaged uncompensated loads associated with eight mascon basins, calculated using equation G.7 with $\rho_c = 2800$ kg m^{-3} and $\Delta\rho = 500$ kg m^{-3}. All of the mascon basins have positive central loads, indicating super-isostasy. The super-isostatic centers are surrounded by regions of sub-isostasy, typically at radial distances of around 200-400 km. Orientale basin stands out from the other basins, with a more strongly negative (i.e. upward buoyant) annular load around the basin periphery. This reflects the relatively low volume of mare infill, which contributes to the large, positive free-air gravity in other basins (*Melosh et al.*, 2013).

4.5.2 Axisymmetric profiles

The analysis of stress states in lunar basins is greatly simplified by assuming axisymmetric loads on a homogeneous elastic plate, which result in axisymmetric hoop and radial stresses. A pair of studies by *Solomon and Head* (1979, 1980) calculated stresses in this way using the elastic flexure formulation of *Brotchie and Sylvester* (1969). Elastic loads in the *Solomon and Head* (1979, 1980) studies were estimated using the geologically mapped distributions of as many as three mare units per basin. Mare thicknesses were estimated so as to match mascon amplitudes (e.g., *Sjogren et al.*, 1974) in a completely uncompensated loading scenario (c.f. equation 1 of *Brotchie and Sylvester* (1969)). We are in a position to improve on the results of *Solomon and Head* (1979, 1980) in a couple of ways. First, the *Brotchie and Sylvester* (1969) formulation is only valid when the width of an elastic load is much smaller than the radius of the sphere; the alternative formulations of *Turcotte et al.* (1981) and *Banerdt* (1986) are more suitable for the broad loads associated with lunar impact basins, and the numerical solutions produced therein more closely match the results of finite element studies (*Freed et al.*, 2001). Secondly, while *Solomon and Head* (1979, 1980) were only able to estimate incremental changes in loading associated with stages of mare infill, free-air gravity from GRAIL allows us to infer the distribution of actual present-day loads. Finally, the ages, stratigraphy and thicknesses of the maria have been more thoroughly characterized in the past few decades by various geological studies (e.g., *Budney and Lucey*, 1998; *Hiesinger et al.*, 2002; *Thomson et al.*, 2009; *Hiesinger et al.*, 2011).

The vertical flexural displacement of a spherical surface may be related to the applied load via a transform function (*Turcotte et al.*, 1981). The resulting vertical displacement of the elastic lithosphere can then be used to calculate the stresses resulting from mascon loading by using the theory in the appendices of *Banerdt* (1986). Although we will only show results for axisymmetric loads, this calculation applies for arbitrary loading distributions on a spherical surface. Using the basin loads shown in Figure 4-4, we can calculate the surficial radial and hoop stresses associated with the present-day load (plotted in Figure 4-5 for the mascon in Mare Serenitatis). The large stress amplitudes are not to be inter-

preted at face value, as much of the stress at the surface associated with bending will be relieved through fault slip (*McNutt*, 1984).

In order to interpret these stress calculations, we use the distributions of wrinkle ridges and concentric rilles mapped by *Solomon and Head* (1980). For basins with identifiable graben structures, constraints on elastic thickness are then determined by finding the range of stress models for which radial stresses are positive over the entire extent of graben formations. Five basins with basin-localized graben structures are listed in Table 4-1 along with the associated elastic thickness bounds. Elastic lithosphere thickness is not expected to remain uniform throughout lunar history: the thermal gradient under an impact basin grows shallower as both the basin and the Moon as a whole cool, and this causes the effective elastic lithosphere to thicken with time (*McNutt*, 1984). The timing of faulting constrains the evolution of the lunar stress state and the evolution of the elastic lithosphere. The ages of mare units modified by graben formation provides an upper bound on the associated graben ages. The mare age ranges as determined by crater size-frequency distributions (*Hiesinger et al.*, 2011) are listed in Table 4-1, along with the relative stratigraphic ages of the basins from *Wilhelms* (1987). Similar estimates of elastic thickness and timing associated with wrinkle ridge formations are listed in Table 4-2, and the ages of mare units modified by wrinkle ridges provide an upper bound on the age of the associated wrinkle ridges.

4.6 Discussion

4.6.1 Constraints on elastic lithosphere thickness

The upper bounds on elastic thickness in Table 4-1 for Imbrium, Serenitatis and Grimaldi basins are smaller than the associated lower bounds on elastic thickness provided in Table 4-2. These conflicting estimates can be resolved by invoking time-evolution of the elastic lithosphere thickness at these three basins, if not other basins. This is consistent with the observation that wrinkle ridges and late mare flooding events often modify graben structures in the basin maria (*Solomon and Head*, 1980). The relative predominance of concentric rilles early in lunar history and the relative abundance of wrinkle ridges formed

after ~3.6 Gya are also consistent with the development of a globally compressive stress environment from a volumetrically contracting Moon (*Solomon*, 1977; *Andrews-Hanna et al.*, 2013b) which may have suppressed extensional tectonics. Thus, the elastic thickness estimates provided by concentric rille distributions typically correspond to an earlier point in lunar history, while estimates from the distribution of wrinkle ridges are closer to the present-day elastic thickness.

The elastic thickness constraints given in Tables 4-1 and 4-2 are generally lower than the constraints given by *Solomon and Head* (1979, 1980), partly due to their use of a different numerical formulation and partly due to a different assumed load (we inferred a distribution of loading from GRAIL gravity while they assumed a load based on the lateral extent of mare deposits). Additionally, extensional stresses around the periphery of a load are larger when calculated using the formalism of *Brotchie and Sylvester* (1969) rather than that of *Banerdt* (1986): a calculation for Mare Serenitatis using the equations of *Brotchie and Sylvester* (1969) with a 50-km-thick lithosphere produced a maximum extensional stress of 150 MPa (which, again, assumes no stress relief via fault slip), while a similar calculation using the equations of *Banerdt* (1986) produced 50 MPa extensional stress. This reduction of modeled extensional stresses at basin peripheries means that the global compressional overprint required to suppress concentric rille formation is generally smaller than previously reported. The extent of global contraction has also been called into doubt by *Watters et al.* (2012), which used the Lunar Reconnaissance Orbiter Camera (LROC) to identify small extensional graben less than 50-My old at the northern end of Mare Nectaris and elsewhere. Such an example of extensional faulting is likely the result of local regional stresses overcoming the globally compressive stress environment.

Elastic thickness constraints from Tables 4-1 and 4-2 are visualized in Figure 4-6 for extensional tectonics (red) and contractional tectonics (green). It is clear in this Figure that a globally extensional stress environment began transitioning into a compressional environment before ~3.6 Gya, consistent with the estimate from *Solomon* (1977). There is a wide range of inferred elastic thicknesses, indicating that the lithosphere may have been significantly heterogeneous at the time of mare deposition. A general increase in elastic lithosphere thickness is also observed over the period of 3.9 to 2.2 billion years before the

present. This trend of lithospheric thickening is consistent with a cooling of the lithosphere under basins and across the Moon as a whole (*Kohlstedt et al.*, 1995; *Turcotte and Schubert*, 2002).

Before we can take historical elastic thickness estimates at face value, we must realize that a number of incremental contributions to the lunar surface stress state (as described in equation 4.3) remain largely unquantified. Consequently, present day stress states and loads determined by GRAIL may not be comparable to the loads at earlier points in the Moon's history. Successive stages of mare flooding may change the relative distribution of loading in a given basin, and *Solomon and Head* (1979, 1980) concluded that the early stages of mare fill in Serenitatis basin were more centrally concentrated than the present day fill. A more centrally-concentrated load would cause the stress curves in Figure 4-5 to shift closer to the axis of symmetry, which would result in larger estimates of elastic thickness at the times of concentric rille and wrinkle ridge formation. However, a thickening of the lithosphere with time at Serenitatis basin is observed even when we use the unit I and unit III mare loads from *Solomon and Head* (1980) to interpret concentric rilles and wrinkle ridges, respectively. We also do not know how fault slip may have relieved stresses in the large impact basins over time. If the amount of fault slip is known, the associated stress change can be theoretically calculated (*Okada*, 1985). Some faults pre-dating mare infill may not have a surface expression, but comparisons of stratigraphic layer variations can constrain the age of faulting relative to the timing of mare flooding events (*Ono et al.*, 2009). Finally, the global stress overprint associated with the late volumetric contraction of the Moon (*Solomon*, 1977) may cause us to overestimate elastic thicknesses after $\sim$3.6 Gya, because a downward shift of the stress curves in Figure 4-5 would result in compressive stresses at greater radial distances from a given basin center. We will postpone a full analysis of elastic thickness evolution at the mascon basins for a future paper in which all contributions to the temporal variability of loading are quantified.

4.6.2 Coulomb stress changes from mare infill

We can quantify the change in stress state associated with the incremental infilling of mare by using equation 4.2 with estimates of mare fill thickness. ALSE profiles are interpreted by *Sharpton and Head* (1982) to imply a thinning of the mare under the circumferential wrinkle ridges, associated with a pre-mare basin ring. Taking this to be the case, we plot the Coulomb stress change for Mare Serenitatis associated with the mare infill load in Figure 4-7. For all elastic thicknesses considered, the Coulomb stress change has a local maximum at the buried basin rim, and the absolute maximum Coulomb stress change occurs at the center of the basin for T_e <100 km. More comprehensive maps of mare thickness have been made, and we can use these to make maps of maximum Coulomb stress change as well. One such map is the Mare Imbrium basalt isopach estimated by *Thomson et al.* (2009), plotted in Figure 4-8a. Faults in our analysis are assumed to have a dip of 30 degrees and are assumed to slip in a reverse sense. Since fault strike also matters for the calculation, we find the fault strike that maximizes Coulomb stress change at each point on the map. Coulomb stress change above a threshold of 20 MPa for T_e=150 km is plotted in Figure 4-8b in pink, along with wrinkle ridge locations plotted in green (bold green indicate high-relief wrinkle ridges). A partial ring of high Coulomb stress change is roughly correlated with the circumferential ring of high-relief wrinkle ridges, although the calculated ring is much thicker than the observed fault distribution, and high Coulomb stress change is calculated at the center of the basin where faulting is not prevalent. Finally, we plot the Coulomb stress change associated with the GRAIL-inferred loading in Figure 4-8d, with GRAIL Bouguer gravity plotted in Figure 4-8c for comparison. The calculated ring of high Coulomb stress change matches the pattern of observed faulting very well in this case, although it falls slightly exterior to the high-relief ridges.

The Coulomb stress distributions plotted in Figures 4-7 and 4-8 indicate that if a pre-mare basin surface is unstressed or homogeneously stressed, we should expect the first mare faulting to occur in a narrow annulus above a buried basin ring and at the basin center. While we do observe faulting at the proposed locations of buried basin rings in Mare Imbrium and Mare Serenitatis (i.e. the circumferential ridges), the centers of these two

basins have a relatively small number wrinkle ridges. In order to understand this observation, it is important to remember that Coulomb stress change refers only to the incremental change in the stress state. The dearth of compressional tectonics may therefore result from a pre-mare stress state that is less compressional at the basin center than at the buried ring. If the post-mare stress state at the basin center was comparable to the stress state immediately to the interior of the buried basin ring, radial surface stresses may have been 15-30 MPa less compressive in the basin center than at the buried ring prior to mare loading (cf. Figure 4-7). Figure 4-5 ostensibly suggests that the radial stresses should be more compressive at basin centers, but the actual surface stresses will be much less than those suggested by Figure 4-5, which assumes an unfractured plate. Pre-mare faulting may be partially responsible for relieving surface stress in the pre-mare basement material, and these faults may be observable at Mare Imbrium with future GRAIL gradiometry analysis (cf. *Andrews-Hanna et al.* (2013b)).

Another ostensible incongruity is that hoop stresses should be more compressive than radial stresses almost everywhere in a basin (e.g., Figure 4-5). This would imply that we should primarily observe concentric rilles and radial wrinkle ridges (along with strike-slip faulting in some cases). Extensional rilles do in fact tend to have a concentric orientation around the basin, but many high-relief wrinkle ridges in the maria are concentric rather than radial. *Freed et al.* (2001) addressed this incongruity by showing that mare deposits with broadly uniform depth can produce radial stresses that are marginally more compressive than hoop stresses in places. However, our Coulomb stress change analysis shows that some of the first thrust faulting in the maria should occur in a narrow annulus over a buried basin ring, and if we except these circumferential wrinkle ridges in Mare Imbrium and Mare Serenitatis, concentric wrinkle ridges are no longer more prominent than radial ridges.

The region of uplifted mantle is approximately demarcated by high positive Bouguer gravity, which also roughly corresponds to the free-air gravity mascon due to the modest topographic variation in the maria. *Neumann et al.* (2013) noted that crustal thickness variations in multi-ringed basins appear to correspond to ring locations, which in turn correspond to higher Coulomb stress changes from mare loading. Therefore the circumferential wrinkle ridges are likely indirectly correlated with GRAIL gravity, as both the basin-localized

tectonics and the gravity anomalies are apparently connected to basin structure.

4.7 Conclusions

By expressing the GRAIL gravity dataset in terms of an uncompensated flexural load, we have characterized the stress states associated with present-day mascon loading. We revisited the calculations of *Solomon and Head* (1979, 1980) and found that their mathematical methodology caused them to modestly overestimate elastic thicknesses while also overestimating extensional stresses at basin peripheries. We also used published estimates of mare fill distribution to calculate the Coulomb stress change associated with mare loading. A local maximum Coulomb stress change occurs over the presumed location of an inner basin ring structure. The effect of such a structure is to localize faulting in a narrow annulus, and this type of faulting is especially apparent in the cirfumferential ridges of Mare Imbrium and Mare Serenitatis. If we ignore these circumferential wrinkle ridges, concentric faulting is no longer more prominent than radial faulting, and it is consequently not imperative for a loading model to produce radial stresses greater than the associated hoop stresses. This eliminates a minor paradox noted by previous lunar stress studies. Calculations based on existing basalt isopach maps only approximately predict the locations of faulting, and these mare thickness maps would be improved by including a more defined basin rim structure.

This study has placed constraints on the thermal and tectonic histories of the lunar nearside basins and maria. The chronologies for Mare Imbrium and Mare Serenitatis are roughly summarized as follows: 1) after the basin forming impact event, inward collapse of the transient cavity forms the major basin rims. 2) Mare basalt floods the basin in stages, spanning several hundreds of millions of years (*Ono et al.*, 2009). 3) Wrinkle ridges develop over buried basin rims, perhaps concurrently with concentric rilles at the basin exterior. 4) As the Moon volumetrically contracts (beginning sometime prior to 3.6 Gya), a compressive stress environment increasingly suppresses extensional tectonics. Wrinkle ridges form in the maria with orientations that are neither predominantly concentric nor predominantly radial. 5) Faults forming between 3.0 Gya and the present day are smaller (tens of kilometers), and correspond to local stress fields.

Table 4.1: Elastic lithosphere thickness estimates from radial distributions of linear and arcuate rilles. Mare age ranges are determined using crater size-frequency distributions (*Hiesinger et al.*, 2011).

Basin	**Rille extent (km)**	**Elastic thickness constraint (km)**	**Associated mare ages (Gy)**	**Basin age (*Wilhelms*, 1987)**
Orientale	200 - 300	None	N/A	Imbrian
Imbrium	400 - 640	0 - 50	2.4 - 3.6	Imbrian
Serenitatis	250 - 400	0 - 20	2.8 - 3.6	Nectarian
Humorum	200 - 400	0 - 18	3.0 - 3.5	Nectarian
Grimaldi	60 - 180	0 - 15	3.0 - 3.1	Pre-Nectarian

Table 4.2: Elastic lithosphere thickness estimates from radial distributions of wrinkle ridges. Mare age ranges are determined using crater size-frequency distributions (*Hiesinger et al.*, 2011), except for Mare Nectaris, which is dated using crater degradation states (*Boyce and Johnson*, 1978).

Basin	**Wrinkle ridge extent (km)**	**Elastic thickness constraint (km)**	**Associated mare ages (Gy)**	**Basin age (*Wilhelms*, 1987)**
Imbrium	0 - 450	>80	2.4 - 3.6	Imbrian
Serenitatis	0 - 300	>30	2.8 - 3.6	Nectarian
Humorum	30 - 180	>10	3.0 - 3.5	Nectarian
Nectaris	0 - 160	None	3.6 - 3.7*	Nectarian
Crisium	0 - 220	>25	3.5 - 3.7	Nectarian
Smythii	40 - 120	>10	N/A	Pre-Nectarian
Grimaldi	30 - 80	>30	3.0 - 3.1	Pre-Nectarian

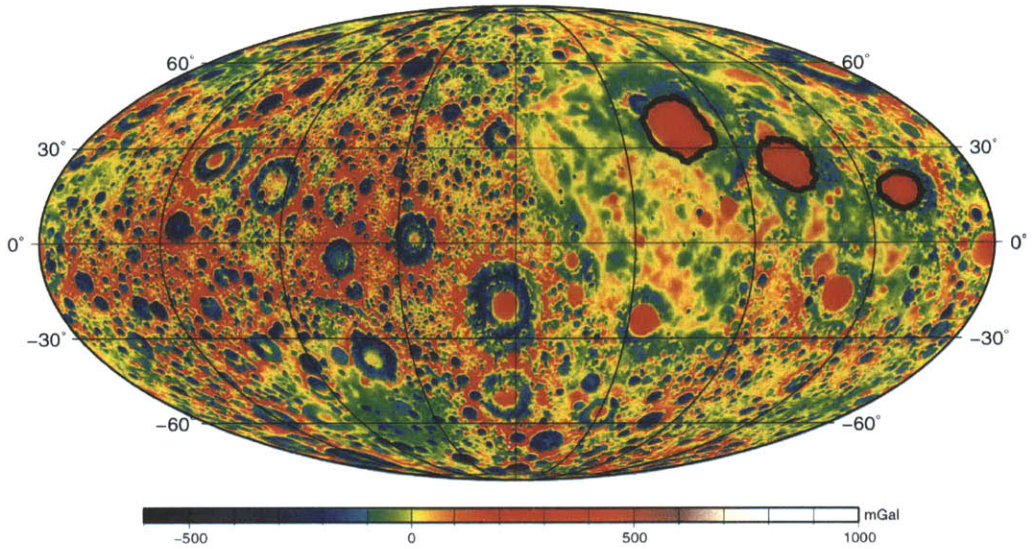

Figure 4-1: An equal-area Mollweide projection of the *GRGM660PRIM* free-air gravity anomaly as measured by GRAIL, with 0.25 ° spatial resolution. The left side of the map corresponds to the lunar far-side, and the right side corresponds to the near-side (longitudes span from -270 ° to 90 °). Bold black lines mark the location of high-relief wrinkle ridges within Imbrium, Serenitatis, and Crisium maria.

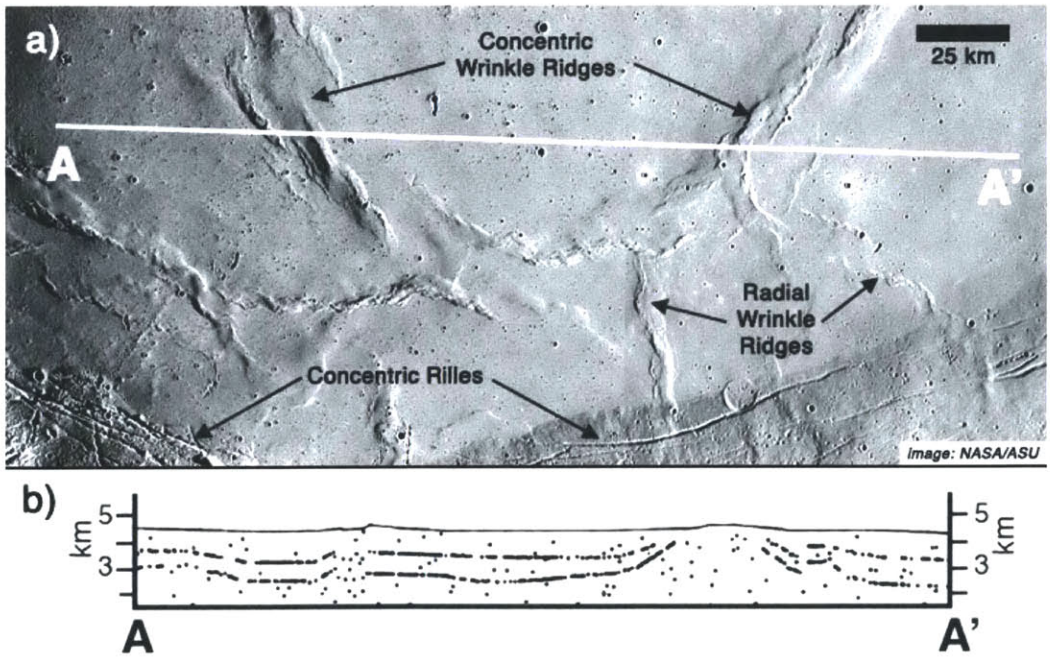

Figure 4-2: a) Faults in the southern portion of Mare Serenitatis, and b) an ALSE profile.

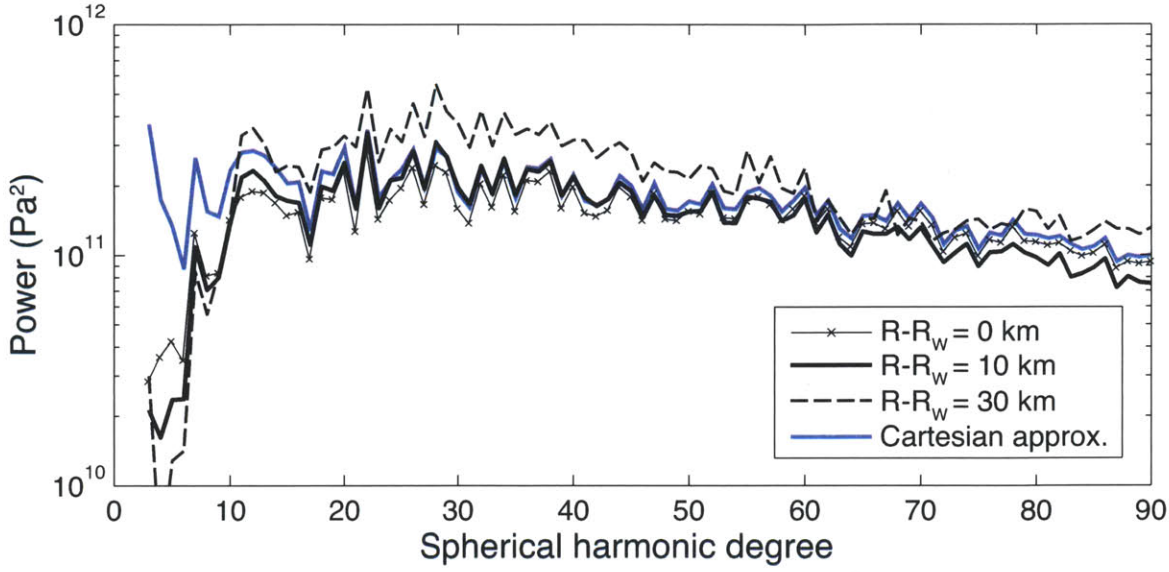

Figure 4-3: Global power of elastic loading as inferred from free-air gravity.

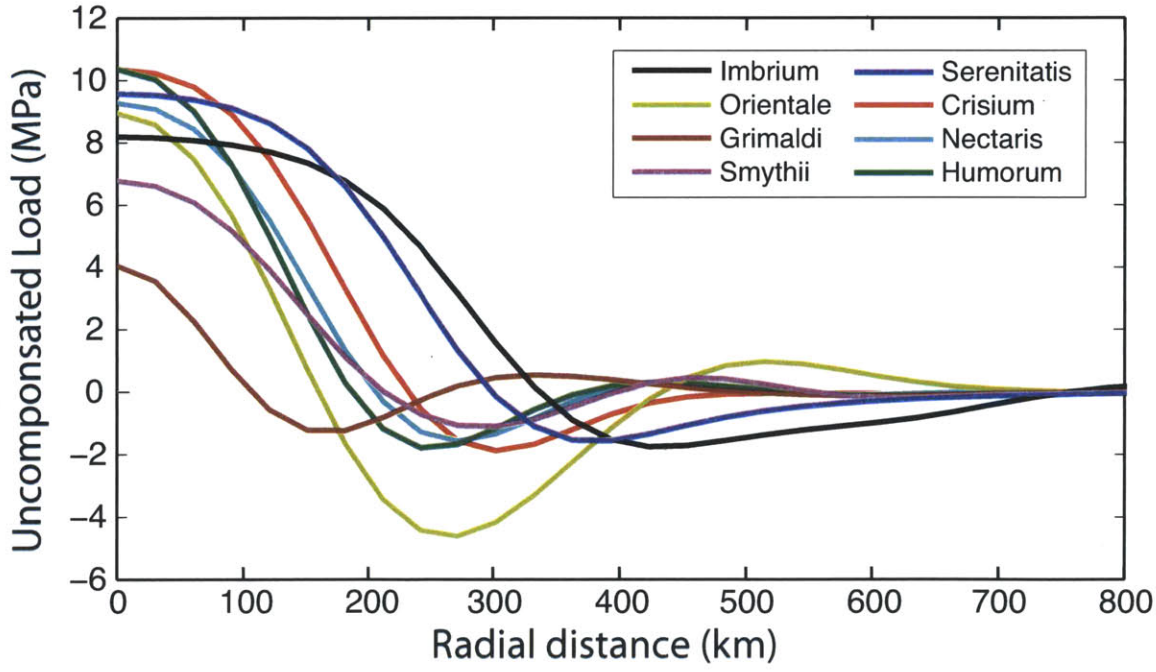

Figure 4-4: Azimuthally-averaged elastic loads for eight nearside basins.

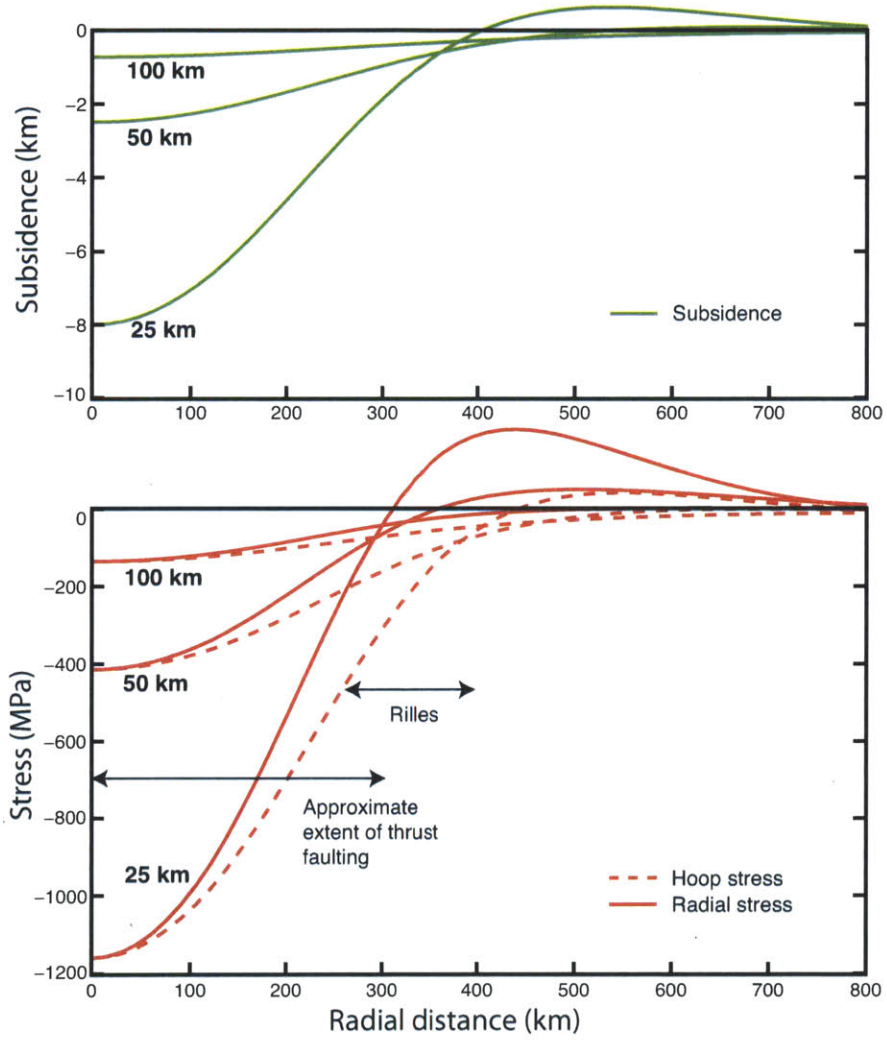

Figure 4-5: Radial stresses and hoop stresses associated with elastic loading at Serenitatis basin for effective elastic thicknesses of T_e = 25, 50, and 100 km.

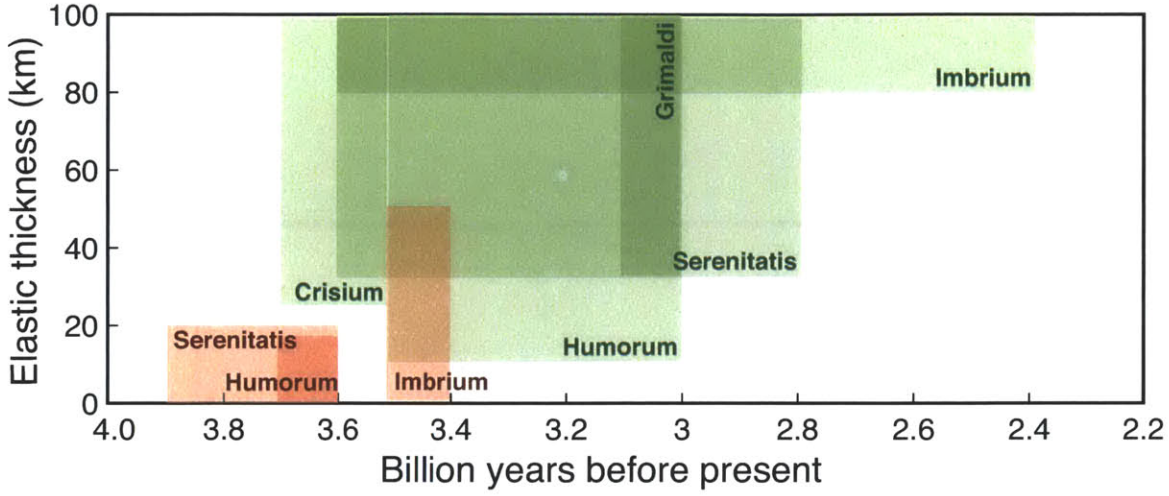

Figure 4-6: Elastic thickness constraints vs. age of the associated mare units, based on concentric rille distributions (red) and wrinkle ridge distributions (green).

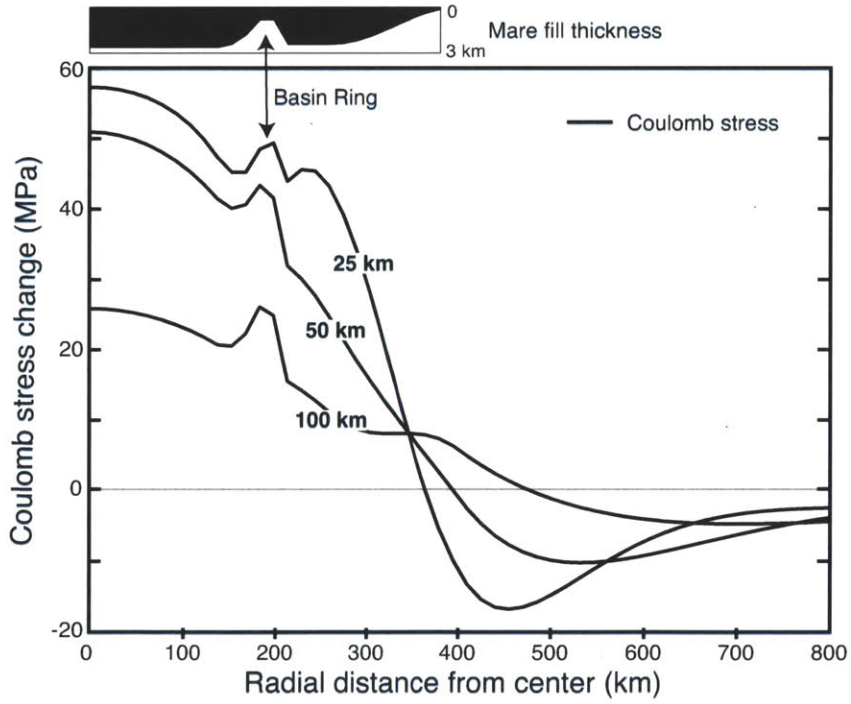

Figure 4-7: Coulomb stress change for thrust faulting associated with mare emplacement, with effective elastic thicknesses of T_e = 25, 50, and 100 km.

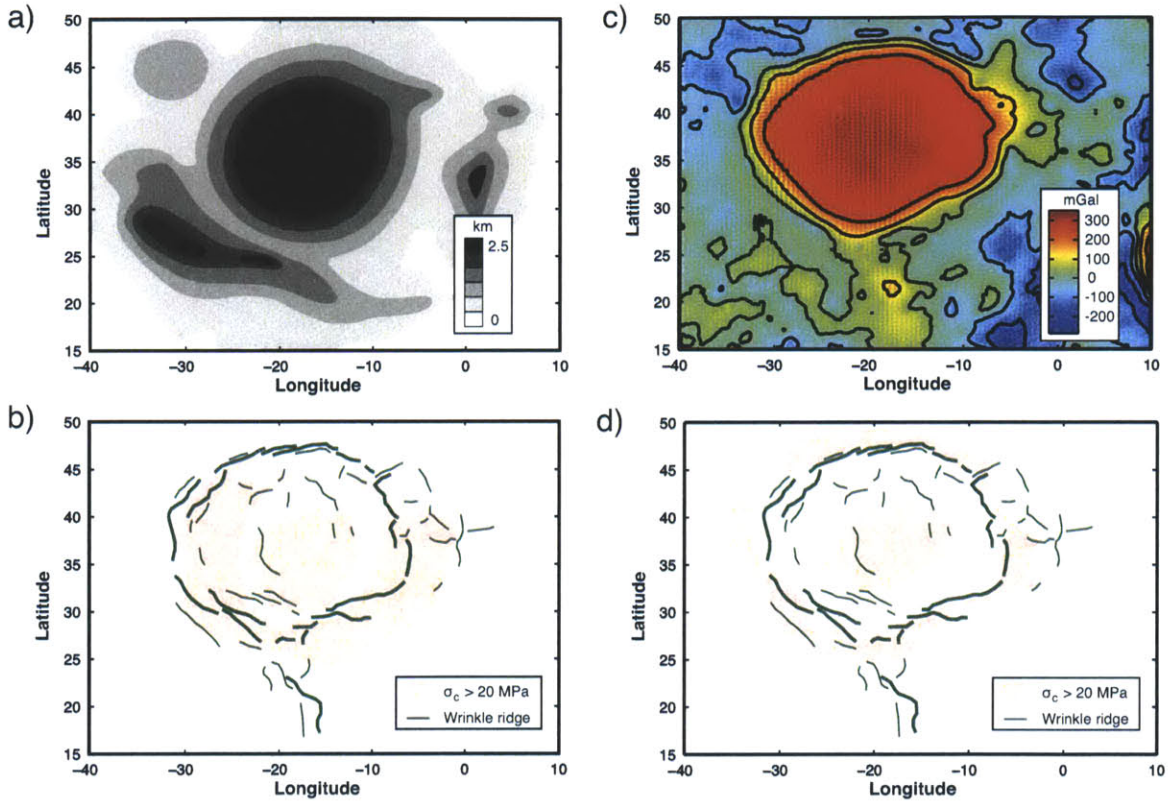

Figure 4-8: a) Mare Imbrium fill thickness from *Thomson et al.* (2009), b) Coulomb stress change due to elastic loading associated with the *Thomson et al.* (2009) model, c) GRAIL Bouguer gravity, d) Coulomb stress change from the assumption that the GRAIL-inferred loading is caused by uncompensated mare fill alone.

Chapter 5

Conclusions and Future Work

The analysis of elastic loads in chapter 4 utilized the free-air gravity anomaly from GRAIL, but it did not fully take advantage of the gravity field at its highest resolution. At spherical harmonic degrees higher than about 100, the observed gravity field primarily samples the distribution of mass shallower than the crust-mantle interface (*Wieczorek*, 2013). At the highest spherical harmonic degrees (greater than about l=200), the observed admittance function can be used to infer crustal density (cf. Figures 5-8 and 5-9 of *Evans* (2013)). This analysis requires corrections for finite-amplitude topographic relief (*Wieczorek and Phillips*, 1998).

Figure 1 shows the first four Slepian tapers with L=60 bandwidth (*Dahlen and Simons*, 2008), localized to Mare Crisium (the outline of Mare Crisium is defined by the basalt unit in the geological map of *Wilhelms and McCauley* (1971)). For the given bandwidth, only these four tapers have better than 99% localization within the desired region. Given that the amplitude of topography immediately exterior to the mare is much larger than the topographic variation within the mare, any spatial leakage of the Slepian taper may bias the admittance analysis, even for 99% localization. Therefore it will be useful to calculate admittances and correlations of gravity and topography with spatio-spectral tapers of higher bandwidth. However, this will be computationally intensive: the eigenvalue/eigenvector analysis required to create Figure 5-1 took about 16 hours to run on a laptop. With higher Slepian bandwidths, we may be able to localize gravity and topography to individual volcanic units (such as those mapped by *Wilhelms and McCauley* (1971). These observations

of mare density could be compared with elemental abundances from Lunar Prospector to constrain the compositions of the mare units, which would give us information about the source regions from which the magmas were derived.

Further analysis of basin-localized tectonics and stress states remains to be done. The stress calculations of Chapter 4 used a thin-shell approximation for the Moon's elastic lithosphere (*Banerdt*, 1986), but stresses in a moderately thick elastic lithosphere may also be calculated with semi-analytical theory (*Banerdt et al.*, 1982). Such an analysis may allow us to further distinguish between loads associated with the crust-mantle interface and the loads from mare infill.

Finally, future work related to lunar stress states will incorporate geological observations to quantify the time-varying elastic load associated with mare loading. As a result of the breadth of available lunar data and the sophistication of mathematical techniques that have been developed over the past several decades, there is more analysis that can be done. Some of our plans for future work include: estimating the geological strain across lunar faults from Apollo and LROC camera imagery; considering how the stress relaxation associated with fault slip affects regional stress distributions and radial vs. concentric orientations of faulting (this can be analytically calculated using the theory of *Okada* (1985)); incorporating the outputs of hydrocode basin simulations; and including arbitrary stress states (including shearing loads, which may arise from fully 3D models of impact basin formation). Mapping of mare thickness and density will improve the interpretation of the Moon's thermal evolution as well, by more thoroughly quantifying the size and shape of temporal loads. Finally, the question of whether interior basin faults are obscured by mare flooding may be addressed by GRAIL gradiometry, which has been moderately successful at identifying subsurface fault structures (*Andrews-Hanna et al.*, 2013b). Each new analysis of the Moon's tectonic and gravity structure gives us an ever-improving picture of how this planetary body formed and evolved to the present day.

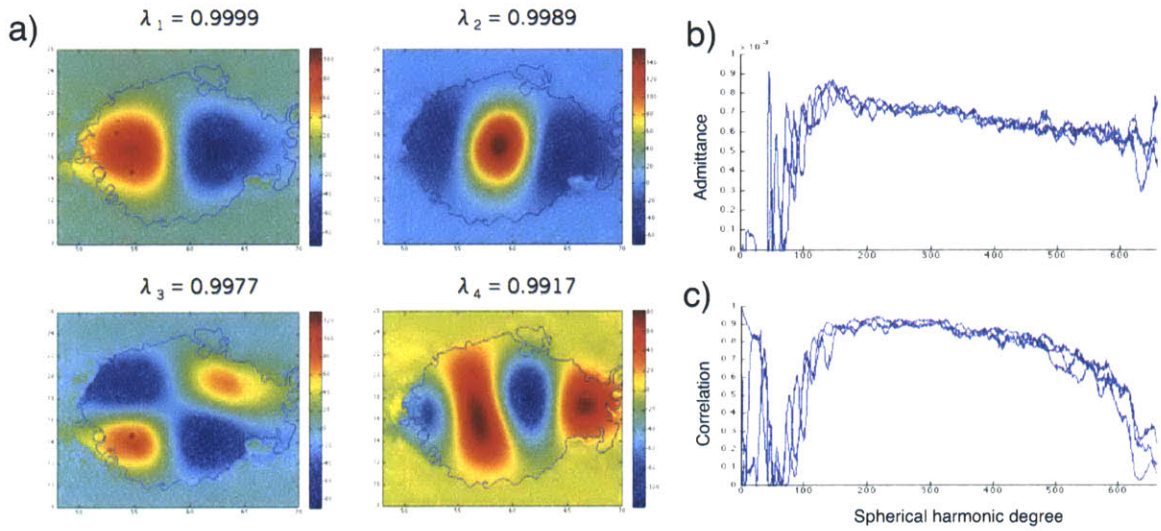

Figure 5-1: a) Energy of a multi-taper spatio-spectral localization at Mare Crisium, b) Calculated admittance and coherence.

Appendix A

Gravitational potentials from finite-amplitude interface relief

Wieczorek and Phillips (1998) derived the static potential perturbations $U(\Omega)$ in a sphere at radius r produced by an interface $B(\Omega)$ with a density contrast $\Delta\rho_B$ at radius R_B:

$$U_{lm}(r) = \begin{cases} \frac{4\pi G R_B^2}{2l+1} \left(\frac{R_B}{r}\right)^{l+1} \sum_{n=1}^{l=3} \frac{{}^nB_{lm}\Delta\rho_B}{R_B^n n!} \frac{\prod_{j=1}^{n}(l+4-j)}{l+3} & r > R_B + \max(B) \\ \frac{4\pi G R_B^2}{2l+1} \left(\frac{r}{R_B}\right)^{l} \sum_{n=1}^{\infty} \frac{{}^nB_{lm}\Delta\rho_B}{R_B^n n!} \frac{\prod_{j=1}^{n}(l+j-3)}{l-2} & r < R_B + \min(B) \end{cases} \quad \text{(A.1)}$$

Equation (A1) accounts for finite amplitude relief on B by incorporating powers of topography, which must be numerically calculated:

$${}^nB_{lm} = \frac{1}{4\pi} \iint_{\Omega} B^n(\Omega) \cdot Y_{lm}(\Omega) d\Omega \quad \text{(A.2)}$$

The higher order summation terms in equation (A1) fall off rapidly with increasing n. For the relief amplitudes encountered on Venus it is sufficient to truncate the summation at $n = 3$, although with the exception of topography and Moho relief at Maxwell Montes, finite amplitude corrections are mostly unnecessary. When interface relief is small, the summation terms for $n > 1$ are negligible and we can re-write equation (A1) in terms of the equipotential perturbation $N^B(\Omega, r)$ for upward- and downward-continuation:

$$N_{lm}^{B}(r) = \begin{cases} \frac{4\pi G R_B^2}{g_r(2l+1)} \left(\frac{R_B}{r}\right)^{l+1} \Delta\rho_B B_{lm} & r \geq R_B \\ \frac{4\pi G R_B^2}{g_r(2l+1)} \left(\frac{r}{R_B}\right)^{l} \Delta\rho_B B_{lm} & r < R_B \end{cases} \tag{A.3}$$

where g_r is the gravitational acceleration at radius r.

If topography H and Moho relief W have finite amplitudes, we can calculate the geoid correction N^{finite}:

$$N_{lm}^{finite} = \frac{4\pi G R^2}{g(2l+1)} \sum_{n=2}^{l+3} \left[{}^{n}H_{lm}\rho_c + {}^{n}W_{lm}\Delta\rho \left(\frac{R_W}{R}\right)^{l+3-n} \right] \frac{\prod_{j=1}^{n}(l+4-j)}{(l+3R^n n!}. \tag{A.4}$$

Appendix B

Propagator Matrices and Dynamic Response Kernels

Incompressible Newtonian flow in a spherical shell can be analytically calculated by propagating velocity and stress boundary conditions through the interior of the body. Following the methodology of *Hager and Clayton* (1989), we define a vector of velocity and stress variables in terms of the reference viscosity μ_0 and radial position r:

$$\mathbf{u}_{lm}(r) = \begin{bmatrix} v^r_{lm}(r) \\ v^\theta_{lm}(r) \\ (\tau^{rr}_{lm}(r) + \rho_r g_r N^r_{lm}) \frac{r}{\mu_0} \\ \tau^{r\theta}_{lm}(r) \frac{r}{\mu_0} \end{bmatrix}. \tag{B.1}$$

$v^r_{lm}(r)$ and $v^\theta_{lm}(r)$ are radial and poloidal velocity coefficients, respectively. $\tau^{rr}_{lm}(r)$ and $\tau^r_{lm}(r)$ are normal stress and poloidal shear stress coefficients. Other parameters are the local density ρ_r, the local gravitational acceleration g_r, and the local gravitational equipotential surface N^r_{lm}. With the introduction of a new variable $\upsilon = ln(r/R)$, the problem of Stokes flow in a sphere can be posed as a first-order differential equation:

$$\frac{d\mathbf{u}}{d\upsilon} = \mathbf{A}\mathbf{u} + \mathbf{a} \tag{B.2}$$

where

$$\mathbf{A} = \begin{bmatrix} -2 & l & 0 & 0 \\ -1 & 1 & 0 & \mu^{-1} \\ 12\mu & -6l\mu & 1 & l \\ -6\mu & (4l-2)\mu & -1 & -2 \end{bmatrix} \tag{B.3}$$

and

$$\mathbf{a} = \begin{bmatrix} 0 \\ 0 \\ g_r r^2 \delta\rho_{lm}(r)/\mu_0 \\ 0 \end{bmatrix}. \tag{B.4}$$

Here, μ is viscosity normalized by the reference viscosity and $\delta\rho_{lm}$ represents the anomalous density distribution. Solutions to equation B.2 can be represented with propagator matrices of the form:

$$\mathbf{P}_{RR_0} = \exp\left[\mathbf{A} \cdot ln(-R_0/R)\right]. \tag{B.5}$$

The matrix $\mathbf{P}_{RR_0}$ propagates the vector $\mathbf{u}$ at radius R_0 to the planetary radius R. We can consider the simplified case in which viscosity is a step-wise function of radius and anomalous density is replaced by discrete sheet masses Ψ^j_{lm} (with units of kg m^{-2}). The solution to equation B.2 can then be represented by equating the surface boundary condition to the upward-propagated boundary conditions of $J+1$ interior interfaces:

$$\mathbf{u}(R) = \mathbf{P}_{RR_0}\mathbf{u}(R_0) + \sum_{j=1}^{J} \mathbf{P}_{RR_j}\mathbf{a}_j \tag{B.6}$$

and

$$\mathbf{a} = \begin{bmatrix} 0 \\ 0 \\ r_j g_{r_j} \Psi^j_{lm}/\mu_0 \\ 0 \end{bmatrix}. \tag{B.7}$$

The formulation of propagator matrices makes it simple to construct an n-layered model in which viscosity varies radially in a step-wise sense:

$$\mathbf{P}_{RR_0} = \mathbf{P}_{RR_{n-1}} \cdot \mathbf{P}_{R_{n-1}R_{n-2}} \cdots \mathbf{P}_{R_2R_1} \cdot \mathbf{P}_{R_1R_0}. \tag{B.8}$$

In this way we can represent an arbitrary radially symmetric distribution of viscosity in the planet's interior.

The equations of flow must be constrained by boundary conditions at the surface and at the core-mantle boundary. With a free slip condition for the liquid core boundary at $r = R_C$ and a no-slip condition at the surface of the planet, we can write the system of equations for flow driven by a single mass sheet Ψ at $r = R_\Psi$:

$$\begin{bmatrix} 0 \\ 0 \\ -\rho_m g \left(H_{lm}^{dyn} - N_{lm}^{dyn} \right) - p_{lm} \\ \tau_{lm}^{r\theta}(R) \end{bmatrix} = \mathbf{P}_{RR_C} \begin{bmatrix} 0 \\ \frac{\mu_0}{R} v_{lm}^{\theta}(R_C) \\ \frac{R_C}{R} \Delta\rho_{core} g_C C_{lm} \\ 0 \end{bmatrix} + \mathbf{P}_{RR_\Psi} \begin{bmatrix} 0 \\ 0 \\ \frac{R_\Psi g_\Psi}{R} \Psi_{lm} \\ 0 \end{bmatrix}. \tag{B.9}$$

where g_Ψ and g_C are the gravitational accelerations at radii $r = R_\Psi$ and R_C. The propagator matrices $\mathbf{P}_{RR_C}$ and $\mathbf{P}_{RR_\Psi}$ represent propagation of internal boundary conditions from the core to the surface and from the loading depth to the surface, respectively. The surface boundary condition includes a flexural term p that is reminiscent of a bottom-loading flexure scenario (see appendix C for discussion). This system of four equations has four unknowns: surface relief H_{lm}^{dyn}, surface poloidal shear stress $\tau_{lm}^{r\theta}(R)$, core-mantle boundary relief C_{lm}, and liquid core poloidal velocity $v_{lm}^{\theta}(R_C)$. Alternative boundary conditions can also be explored; for example, a free-slip boundary condition at the surface and a no-slip boundary condition at the CMB would be modeled by the following system of equations:

$$\begin{bmatrix} 0 \\ \frac{\mu_0}{R} v^{\theta}_{lm}(R) \\ -\rho_m g \left(H^{dyn}_{lm} - N^{dyn}_{lm} \right) - p_{lm} \\ 0 \end{bmatrix} = \mathbf{P}_{RR_C} \begin{bmatrix} 0 \\ 0 \\ \frac{R_C}{R} \Delta\rho_{core} g_C C_{lm} \\ \tau^{r\theta}_{lm}(R_C) \end{bmatrix} + \mathbf{P}_{RR_\Psi} \begin{bmatrix} 0 \\ 0 \\ \frac{R_\Psi g_\Psi}{R} \Psi_{lm} \\ 0 \end{bmatrix}. \tag{B.10}$$

where surface poloidal velocity $v^{\theta}_{lm}(R)$ and CMB poloidal shear stress $\tau^{r\theta}_{lm}(R_C)$ are the new free variables.

Once the equations of flow have been solved for the free variables, we can develop a few degree-dependent kernels that are related to the geoid and surface topography. Following the terminology of *Richards and Hager* (1984), the first kernel is defined as the total geoid anomaly at the surface scaled by the internal mass perturbation:

$$G^{dyn}_l = \frac{N^{dyn}_{lm}}{\Psi_{lm}} \tag{B.11}$$

where the portion of geoid height produced by dynamic flow N^{dyn} is known implicitly via the summed contributions of the three interfaces:

$$N^{dyn}_{lm} = \frac{4\pi GR}{g(2l+1)} \left[\rho_m H^{dyn}_{lm} + \left(\frac{R_\Psi}{R} \right)^{l+2} \Psi_{lm} + \Delta\rho_{core} \left(\frac{R_C}{R} \right)^{l+2} C_{lm} \right]. \tag{B.12}$$

The equivalent kernel for Airy isostatic compensation of non-finite amplitude topography at the Moho can be calculated using equations 2.6 and 2.7:

$$G^{Airy}_l = \frac{4\pi GR}{g(2l+1)} \left[-\left(\frac{R_W}{R} \right)^2 + \left(\frac{R_W}{R} \right)^{l+2} \right] \tag{B.13}$$

An alternative kernel preferred by some authors (e.g. *Herrick and Phillips* (1992)) is the potential kernel:

$$K^{dyn}_l = \frac{N^{dyn}_{lm}}{N^{\Psi}_{lm}} \tag{B.14}$$

where N_{lm}^{Ψ} is the static geoid contribution from the sheet mass Ψ:

$$N_{lm}^{dyn} = \frac{4\pi GR}{g(2l+1)} \left(\frac{R_{\Psi}}{R} \right)^{l+2} \Psi_{lm}. \tag{B.15}$$

The second kernel is the gravitational admittance associated with dynamic flow:

$$Z_l^{dyn} = \frac{N_{lm}^{dyn}}{H_{lm}^{dyn}}. \tag{B.16}$$

When dealing with self-gravitation, it is sometimes convenient to use an adjusted admittance function for which the denominator is the topography in excess of the associated geoid:

$$\bar{Z}_l^{dyn} = \frac{N_{lm}^{dyn}}{H_{lm}^{dyn} - N_{lm}^{dyn}} = \left(\frac{1}{Z_l^{dyn}} - 1 \right). \tag{B.17}$$

The third kernel signifies surface displacements normalized by the mantle mass load:

$$D_l^{dyn} = \frac{H_{lm}^{dyn}}{\Psi_{lm}} = \frac{G_l^{dyn}}{Z_l^{dyn}}. \tag{B.18}$$

We can use kernels to relate an unknown mantle load to the dynamic components of the geoid and geoid-corrected topography:

$$N_{lm}^{dyn} = G_l^{dyn} \Psi_{lm}, \tag{B.19}$$

and

$$\bar{H}_{lm}^{dyn} = \frac{G_l^{dyn}}{\bar{Z}_l^{dyn}} \Psi_{lm}. \tag{B.20}$$

Appendix C

An Elastic Lithosphere that Resists Dynamic Flow

The elastic response of a planet's lithosphere to loading can be modeled as a thin spherical shell. A load $p(\Omega)$ acting on a shell can be related to the flexure of the shell from its undeformed configuration $F(\Omega)$ (*Turcotte et al.*, 1981):

$$\left(D\nabla^6 + 4D\nabla^4 + ET_eR^2\nabla^2 + ET_eR^2\right) F(\Omega) = R^4\left(\nabla^2 + 1 - \nu\right) p(\Omega). \tag{C.1}$$

Similar to the dynamic flow analysis of appendix B, this formulation neglects toroidal flexure terms and assumes laterally homogeneous material parameters. We can write a solution to this equation by first defining two non-dimensional parameters:

$$c_l^1 = \frac{-l^3(l+1)^3 + 4l^2(l+1)^2}{-l(l+1) + 1 - \nu} \tag{C.2}$$

and

$$c_l^2 = \frac{-l(l+1) + 2}{-l(l+1) + 1 - \nu}. \tag{C.3}$$

We can then write solutions to equation in terms of spherical harmonic coefficients:

$$e_l F_{lm} = p_{lm} \tag{C.4}$$

where the amplitude of flexure is linearly related to the elastic loading by a degree-dependent term e_l:

$$e_l = \frac{D}{R^4} c_l^1 + \frac{ET_e}{R^2} c_l^2. \tag{C.5}$$

The first term in equation C.5 is associated with bending stresses, which are relevant at higher degrees, and the second term is associated with membrane stresses.

If the flexural displacement F is defined to be the component of topography associated with dynamic flow (i.e. $F = H^{dyn}$), then equation C.4 can be inserted into the dynamic flow equations B.9. We can rearrange B.9 and solve the four equations ($i = 1 : 4$) using an arbitrarily unitary mantle mass load:

$$\begin{aligned}
&\mathbf{P^{i2}_{RR_C}} \frac{\mu_0}{R} v^{\theta}_{lm}(R_C) \\
&+ \left[\mathbf{P}^{i3}_{RR_C} g_C \frac{R_C}{R} - \delta_{i3} \frac{4\pi G}{2l+1} \rho_m R \left(\frac{R_C}{R} \right)^{l+2} \right] \Delta\rho_{core} C_{lm} \\
&+ \delta_{i3} \left[\rho_m g - \frac{4\pi G}{2l+1} R {\rho_m}^2 + e_l \right] H^{dyn}_{lm} \\
&+ \delta_{i4} \tau^{r\theta}_{lm}(R) \\
&= -\mathbf{P}^{i3}_{RR_\Psi} \frac{R_\Psi g_\Psi}{R} + \delta_{i3} \frac{4\pi G}{2l+1} \rho_m R \left(\frac{R_\Psi}{R} \right)^{l+2}
\end{aligned} \tag{C.6}$$

where the Kronecker delta, δ_{ij}, equals one if $i = j$ and equals zero otherwise. Solutions for the four free variables can then be used to develop the kernels in appendix B.

Appendix D

Data and uncertainty quantification

The sine and cosine coefficients for a spherical harmonic expansion can be represented in a single vector $\mathbf{c}$. The covariance matrix of $\mathbf{c}$ is $\mathbf{\Sigma} = \mathbf{Q\Lambda Q}^{-1}$, where $\mathbf{Q}$ is the matrix of covariance eigenvectors and $\mathbf{\Lambda}$ is the diagonal matrix of covariance eigenvalues. We want to generate a vector of random errors $\mathbf{x}$ associated with the spherical harmonic coefficients. The multivariate normal distribution for a given error vector $\mathbf{x}$ of length k is:

$$f_{\mathbf{x}} = \frac{1}{(2\pi)^{\frac{k}{2}} |\mathbf{\Sigma}|^{\frac{1}{2}}} \exp\left(-\frac{1}{2}\mathbf{x}^{\mathbf{T}}\mathbf{\Sigma}^{-1}\mathbf{x}\right) \tag{D.1}$$

For the sake of simplicity, we define a vector $\mathbf{y}$ related to $\mathbf{x}$ through a linear transformation:

$$\mathbf{y} \equiv \mathbf{Q}^{\mathbf{T}}\mathbf{x}. \tag{D.2}$$

We can then define the multivariate normal distribution of a vector y in terms of the eigenvalue matrix :

$$f_{\mathbf{y}} = \frac{1}{(2\pi)^{\frac{k}{2}} |\mathbf{\Lambda}|^{\frac{1}{2}}} \exp\left(-\frac{1}{2}\mathbf{y}^{\mathbf{T}}\mathbf{\Lambda}^{-1}\mathbf{y}\right). \tag{D.3}$$

Since Λ is a diagonal matrix, we can further decompose the density function in terms of the covariance matrix eigenvalues λ_n:

$$f_{\mathbf{y}} = \prod_{n=1}^{k} f_n \tag{D.4}$$

where

$$f_n = (2\pi\lambda_n)^{-\frac{1}{2}} \exp\left(-\frac{\mathbf{y}_n^2}{2\lambda_n}\right). \tag{D.5}$$

The cumulative distribution function (CDF) for a single variable is:

$$\Phi_n = \int_{-\infty}^{\mathbf{y}_n} f_n \partial \mathbf{y}_n = \frac{1}{2}\left[1 + erf\left(\frac{\mathbf{y}_n}{\sqrt{2\lambda_n}}\right)\right] \tag{D.6}$$

For a series of k random CDF values selected on the interval $\Phi_n \in (0, 1)$, the values of $\mathbf{y}_n$ needed to reproduce that CDF are:

$$\mathbf{y}_n = \sqrt{2\lambda_n} erf^{-1}\left(2\Phi_n - 1\right). \tag{D.7}$$

The vector $\mathbf{y}$ can then be transformed back into the original coordinates:

$$\mathbf{x} = \mathbf{Q}\mathbf{y}. \tag{D.8}$$

This is a random realization of spherical harmonic error, and a noisy set of spherical harmonic functions can be calculated:

$$\mathbf{c}_{noisy} = \mathbf{c} + \mathbf{x}. \tag{D.9}$$

Appendix E

Theoretical admittances

We are interested in determining the gravitational perturbations caused by flexural loading on an elastic shell, and how those perturbations scale to the height of topography. Flexural loads can exist above the elastic lithosphere, below the elastic lithosphere, or in some combination of top and bottom loading. In order to quantify the loading state, we introduce a loading parameter λ signifying the ratio of top loading to bottom loading:

$$\lambda = -\left(\frac{R}{R_\sigma}\right)^2 \frac{\rho_c \left(H_{lm} - F_{lm}\right)}{\sigma_{lm}}. \tag{E.1}$$

The bottom load at radius R_σ can then be expressed in terms of the planetary radius R, topography H, flexure F, and the loading ratio λ:

$$\sigma_{lm} = -\frac{\rho_c}{\lambda}\left(\frac{R}{R_\sigma}\right)^2 \left(H_{lm} - F_{lm}\right). \tag{E.2}$$

See figure E-1 for an illustration of the problem setup. The equation relating a load p to an elastic deflection F is given by *Turcotte et al.* (1981):

$$\left(D\nabla^6 + 4D\nabla^4 + ET_eR^2\nabla^2 + 2ET_eR^2\right) F(\Omega) = R^4\left(\nabla^2 + 1 - \nu\right) p(\Omega). \tag{E.3}$$

This formulation neglects toroidal flexure terms and assumes laterally homogeneous material parameters. We can write a solution to equation E.3 by first defining two non-

dimensional parameters:

$$k_l^1 = \frac{-l^3(l+1)^3 + 4l^2(l+1)^2}{-l(l+1) + 1 - \nu} \tag{E.4}$$

and

$$k_l^2 = \frac{-l(l+1) + 2}{-l(l+1) + 1 - \nu}. \tag{E.5}$$

The parameter k^1 corresponds to bending stresses, and the parameter k^2 corresponds to membrane stresses. Solutions to equation E.3 can be written in terms of spherical harmonic coefficients:

$$\left(\frac{D}{R^4}k_l^1 + \frac{ET_e}{R^2}k_l^2\right) F_{lm} = p_{lm} \tag{E.6}$$

We can alternatively write a flexure equation with a non-dimensional flexure parameter E_l which relates the amplitude of flexure to the uncompensated portion of topography:

$$E_l F_{lm} = -H_{lm}^{uncompensated} \tag{E.7}$$

where E_l is defined in terms of the flexural parameters in equations E.4 and E.5:

$$E_l = \frac{D}{\rho_c g R^4}k_l^1 + \frac{ET_e}{\rho_c g R^2}k_l^2 \tag{E.8}$$

We equate this flexural load to an Airy isostatic residual:

$$(H_{lm} - N_{lm}) + \frac{\Delta\rho}{\rho_c}\left(\frac{R_W}{R}\right)^2 (F_{lm} - N'_{lm}) + \left(\frac{R_\sigma}{R}\right)^2 \sigma_{lm} = -E_l F_{lm}. \tag{E.9}$$

In order to account for self-gravitation, we include expressions for the local equipotential surfaces at the surface and the crust-mantle boundary, respectively:

$$N_{lm} = \frac{4\pi R^3}{M(2l+1)} \left[\rho_c H_{lm} + \left(\frac{R_W}{R} \right)^{l+2} \Delta\rho F_{lm} + \left(\frac{R_\sigma}{R} \right)^{l+2} \sigma_{lm} \right] \tag{E.10}$$

and

$$N'_{lm} = \frac{4\pi R^3}{M(2l+1)} \left[\left(\frac{R_W}{R} \right)^{l} \rho_c H_{lm} + \frac{R_W}{R} \Delta\rho F_{lm} + \left(\frac{R_\sigma}{R_W} \right)^{l+2} \sigma_{lm} \right] \tag{E.11}$$

.

Equation E.9 can be rearranged to find the ratio of gravity over topography, g_{lm}/H_{lm}, i.e. the admittance function for flexural loading on a self-gravitating sphere:

$$Z_l = \frac{g_{lm}}{H_{lm}} = 4\pi\rho_c G \frac{l+1}{2l+1} \left[1 - \left(\frac{R_W}{R} \right)^{l} \frac{(1 - SG_l^1)\, C_l + (R_\sigma/R_W)^l\, E_l + BL_l^1}{(1 - SG_l^2)\, C_l + \lambda E_l + BL_l^2} \right]. \tag{E.12}$$

This equation makes use of a parameter C_l, two self-gravitational terms and two terms associated with bottom loading:

$$C_l = \left(\frac{R_\sigma}{R_W} \right)^{l} + \lambda \frac{\Delta\rho}{\rho_c} \left(\frac{R_W}{R} \right)^{2} \tag{E.13}$$

$$SG_l^1 = \frac{4\pi\rho_c R^3}{M(2l+1)} \left[1 + \frac{\Delta\rho}{\rho_c} \left(\frac{R_W}{R} \right)^{l+2} \right] \tag{E.14}$$

$$SG_l^2 = \frac{4\pi\rho_c R^3}{M(2l+1)} \left[\left(\frac{R_W}{R} \right)^{l} + \frac{\Delta\rho}{\rho_c} \frac{R_W}{R} \right] \tag{E.15}$$

$$BL_l^1 = \frac{\Delta\rho}{\rho_c} \left(\frac{R_W}{R} \right)^{2} \left[\left(\frac{R_\sigma}{R_W} \right)^{l} - 1 \right] \tag{E.16}$$

and

$$BL_l^2 = 1 - \left(\frac{R_\sigma}{R_W}\right)^l . \tag{E.17}$$

The bottom loading terms E.16 and E.17 arise when the bottom loading depth does not equal the depth of the crust-mantle interface.

Equation E.12 can be used for any ratio of top loading to bottom loading, but we can quantify the special cases of pure top and bottom loading. Bottom loading corresponds to a ratio $\lambda = 0$, and the resulting admittance spectrum is found by modifying equation E.12:

$$Z_l(\lambda = 0) = 4\pi\rho_c G \frac{l+1}{2l+1}\left[1 - \left(\frac{R_\sigma}{R}\right)^l \frac{1 - SG_l^1 + E_l + (R_W/R_\sigma)^l BL_l^1}{1 - SG_l^2\,(R_\sigma/R_W)^l}\right]. \tag{E.18}$$

Similarly, we can calculate the admittance spectrum for a pure top-loading scenario (in which λ^{-1} approaches zero):

$$\lim_{\lambda\to\infty} Z_l = 4\pi\rho_c G \frac{l+1}{2l+1}\left[1 - \left(\frac{R_W}{R}\right)^l \frac{1 - SG_l^1}{1 - SG_l^2 + \frac{\rho_c}{\Delta\rho}(R/R_W)^2 E_l}\right] \tag{E.19}$$

Considering the case $E_l = 0$ and $R_\sigma = R_W$, we find the admittance function for Airy isostasy, corrected for self-gravitation:

$$Z_l\left(\begin{array}{c} E_l = 0 \\ R_\sigma = R_W \end{array}\right) = 4\pi\rho_c G \frac{l+1}{2l+1}\left[1 - \left(\frac{R_W}{R}\right)^l \frac{1 - SG_l^1}{1 - SG_l^2}\right]. \tag{E.20}$$

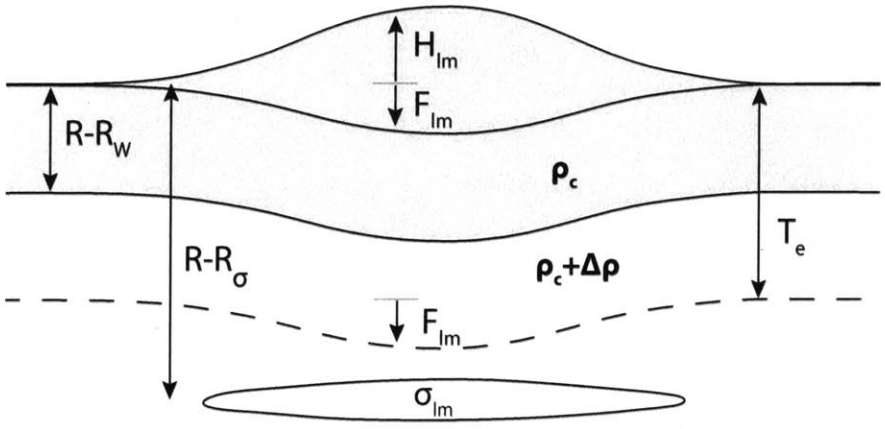

Figure E-1: Set-up of the flexural loading problem.

Appendix F

Two-layered dynamic flow

Dynamic flow in a viscous sphere can by analytically calculated by propagating velocity and stress boundary conditions through the interior (*Hager and Clayton*, 1989). In addition to surface topography H and liquid core boundary relief C, we can imagine that there is an additional boundary D at radius R_D with an intrinsic density contrast $\Delta\rho_D$. The presence of such an interface alters the nature of steady-state flow in Mercury's interior: each increment of flow across D changes the radial load driving flow. Two-layered dynamic flow at a given spherical harmonic degree is governed by a system of four equations:

$$\begin{bmatrix} {}^*v_r(R) \\ {}^*v_\theta(R) \\ -{}^*\tau_{rr}(R) \\ -{}^*\tau_{r\theta}(R) \end{bmatrix} = \mathbf{P}_{RR_C} \begin{bmatrix} {}^*v_r(R_C) \\ {}^*v_\theta(R_C) \\ {}^*\tau_{rr}(R_C) \\ {}^*\tau_{r\theta}(R_C) \end{bmatrix} + \mathbf{P}_{RR_D} \begin{bmatrix} 0 \\ 0 \\ {}^*\tau_{rr}(R_D) \\ 0 \end{bmatrix}. \tag{F.1}$$

The propagator matrices $\mathbf{P}_{RR_C}$ and $\mathbf{P}_{RR_D}$ contain information about the viscosity profile of Mercury (see Appendix B for more information). Spherical harmonic coefficients have been dropped from each variable for the sake of concise notation. Additionally, all velocities and stresses are understood to be non-dimensionalized as follows:

$$v = {}^*v\frac{g\rho R^2}{\mu_0}, \tag{F.2}$$

$$\tau = {}^*\tau g \rho R, \tag{F.3}$$

The radial stress at radius R is equal to the weight of displaced topography plus the pressure applied by elastic flexure:

$${}^*\tau_{rr}(R) = \frac{H - N}{R} + \frac{p}{\rho_m g R} \tag{F.4}$$

The radial stresses at radii R_C and R_D can similarly be calculated:

$${}^*\tau_{rr}(R_C) = \frac{\Delta\rho_C g_C R_C}{\rho_m g R^2}(C - N_C) \tag{F.5}$$

$${}^*\tau_{rr}(R_D) = \frac{\Delta\rho_D g_D R_D}{\rho_m g R^2}(D - N_D) \tag{F.6}$$

The equipotential surfaces at radii R, R_C, and R_D are, respectively:

$$N = \frac{4\pi G R}{g(2l+1)}\left[\rho_m H + \left(\frac{R_C}{R}\right)^{l+2}\Delta\rho_C C + \left(\frac{R_D}{R}\right)^{l+2}\Delta\rho_D D\right] \tag{F.7}$$

$$N_C = \frac{4\pi G R}{g(2l+1)}\left[\left(\frac{R_C}{R}\right)^{l-1}\rho_m H + \Delta\rho_C C + \left(\frac{R_D}{R}\right)^{l-1}\Delta\rho_D D\right] \tag{F.8}$$

$$N_D = \frac{4\pi G R}{g(2l+1)}\left[\left(\frac{R_D}{R}\right)^{l-1}\rho_m H + \left(\frac{R_C}{R_D}\right)^{l+2}\Delta\rho_C C + \Delta\rho_D D\right] \tag{F.9}$$

Since the radial stresses are calculated in equations F.4-F.6, we are left with six unknowns in four equations. In order to find solutions, we must first constrain two more parameters. We chose to do this by assuming no lateral velocities at the surface and no shear stresses at the liquid core boundary.

Radial velocity solutions are used to calculate radial displacements at each interface. Velocities at radii R and R_C are variables in equation F.1, and the radial velocity at R_D can be calculated with another propagator matrix:

$$^*v_r(R_D) = \mathbf{P}^{11}_{R_D R_C} {}^*v_r(R_C) + \mathbf{P}^{12}_{R_D R_C} {}^*v_\theta(R_C) + \mathbf{P}^{13}_{R_D R_C} {}^*\tau_{rr}(R_C). \tag{F.10}$$

We can then step the solution forward in time and modify the interface amplitudes:

$$\Delta H = {}^*v_r(R)\Delta t \tag{F.11}$$

$$\Delta C = {}^*v_r(R_C)\Delta t \tag{F.12}$$

$$\Delta D = {}^*v_r(R_D)\Delta t \tag{F.13}$$

We march forward in time using a dynamic time stepping scheme: if the maximum interface change is less than 0.5% then we increase Δt by a factor of 2; if the maximum interface change is larger than 10% we decrease Δt by a factor of 8. The incremental elastic response at a time step is a function of the elastic thickness (*Turcotte et al.*, 1981):

$$\Delta p = \Delta H \left(\frac{ET_e(t)^3}{12R^4(1-\nu^2)} k_l^1 + \frac{ET_e(t)}{R^2} k_l^2 \right) \tag{F.14}$$

where the parameters k_l^1 and k_l^2 are defined in Appendix E.

Appendix G

Elastic loads inferred from free-air gravity

Since free air gravity includes contributions from both isosatically compensated topography and uncompensated topography, we must separate these two contributions in order to reliably infer flexural loads on the surface.

The magnitude of the downward net load σ caused by uncompensated topography is dependent on topography, on the crust-mantle interface relief, and the associated equipotential reliefs:

$$\sigma = (H_{lm} - N_{lm})\,\rho_c g_0 + (W_{lm} - N'_{lm})\,\Delta\rho g_0 \left(\frac{R_W}{R}\right)^2. \tag{G.1}$$

Neglecting finite-amplitude corrections, crust-mantle interface relief W equals a downward-continuation of the Bouguer geoid:

$$W_{lm} = \frac{1}{\Delta\rho}\frac{M(2l+1)}{4\pi R^3}\left(\frac{R}{R_W}\right)^{l+2} N_{Bouguer,lm} \tag{G.2}$$

where

$$N_{Bouguer,lm} = N_{lm} - \frac{4\pi R^3}{M(2l+1)}\rho_c H_{lm}. \tag{G.3}$$

The equipotential surface at the crust-mantle interface is affected by surface topography

and by crust-mantle interface relief:

$$N'_{lm} = \frac{4\pi R^3}{M(2l+1)} \left[\left(\frac{R_W}{R} \right)^l \rho_c H_{lm} + \Delta\rho W_{lm} \right]. \tag{G.4}$$

Free-air gravity acceleration at the surface can be related to the geoid via spherical harmonic transform:

$$g_{lm} = \frac{g_0}{R}(l+1)N_{lm}. \tag{G.5}$$

We can further simplify our analysis by defining the average planetary density:

$$\overline{\rho} = \frac{3}{4}\frac{M}{pi R^3}. \tag{G.6}$$

Dropping second-order terms, we can combine the preceding equations to provide an expression for the flexural load inferred from topography and free-air gravity:

$$\sigma_{lm} = \left[\left[\frac{1}{3} R\overline{\rho} - \left(\Delta\rho + \left(\frac{Rw}{R} \right)^l \rho_c \right) \frac{R}{l+1} \right] g_{lm} - \left[1 - \left(\frac{R_W}{R} \right)^l \right] \rho_c g_0 H_{lm} \right] \left(\frac{R}{R_W} \right)^l. \tag{G.7}$$

If we set $R_W = R$ and ignore terms with spherical harmonic degree l, we can give a first-order approximation for the load in the spatial domain:

$$\sigma(\Omega) = \frac{1}{3} R\overline{\rho} g(\Omega) \tag{G.8}$$

Bibliography

Anderson, E. M. (1951), *The Dynamics of Faulting*, Oliver & Boyd, Edinburgh.

Anderson, F. S. and S. E. Smrekar (2006), Global mapping of crustal and lithospheric thickness on Venus, *J. Geophys. Res.*, 111, E08006, doi:10.1029/2004JE002395.

Anderson, J. D., G. Colombo, P. B. Esposito, E. L. Lau, and G. B. Trager (1987), The Mass, Gravity Field, and Ephemeris of Mercury, *Icarus*, 71, 337-349.

Andrews-Hanna, J. C. (2013), The origin of the non-mare mascon gravity anomalies in lunar basins, *Icarus*, 222, 159-168.

Andrews-Hanna, J. C., S. W. Asmar, J. W. Head III, W. S. Kiefer, A. S. Konopliv, F. G. Lemoine, I. Matsuyama, E. Mazarico, P. J. McGovern, H. J. Melosh, G. A. Neumann, F. Nimmo, R. J. Phillips, D. E. Smith, S. C. Solomon, G. J. Taylor, M. A. Wieczorek, J. G. Williams, and M. T. Zuber (2013), Ancient Igneous Intrusions and Early Expansion of the Moon Revealed by GRAIL Gravity Gradiometry, *Science*, 339, 675-679, doi:10.1126/science.1231753.

Araki, H., A. Tazawa, H. Noda, Y. Ishihara, S. Goossens, S. Sasaki, N. Kawano, I. Kamiya, H. Otake, J. Oberst, and C. Shum (2009), Lunar Global Shape and Polar Topography Derived from Kaguya-LALT Laser Altimetry, *Science*, 323, 897-900, doi:10.1126/science.1164146.

Balcerski, J. A., S. A. Hauck, P. Sun, II, C. Klimczak, P. K. Byrne, A. J. Dombard, O. S. Barnouin, M. T. Zuber, R. J. Phillips, and S. C. Solomon (2012), Tilted crater floors: Recording the history of Mercury's longwavelength deformation, *Lunar Planet. Sci.*, 43, abstract 1850.

Banerdt, W. B., R. J. Phillips, N. H. Sleep, and R. S. Saunders (1982), Thick shell tectonics on one-plate planets: Applications to Mars, *J. Geophys. Res.*, 87, 9723-9733.

Banerdt, W. B. (1986), Support of long-wavelength loads on Venus and implications for internal structure, *J. Geophys. Res.*, 91, 403-419.

Belleguic, V., P Lognonne, and M. Wieczorek (2005), Constraints on the Martian lithosphere from gravity and topography data, *J. Geophys. Res.*, 110, E11005, doi:10.1029/2005JE002437.

Bilotti, F. and J. Suppe (1999), The global distribution of wrinkle ridges on Venus, *Icarus*, 139, 137-157.

Bindschadler, D. L., G. Schubert, and W. M. Kaula (1992), Coldspots and hotspots: global tectonics and mantle dynamics of Venus, *J. Geophys. Res.*, 97, 13495-13532.

Boyce, J. M. and D. A. Johnson (1978), Ages of flow units in the far eastern maria and implications for basin-filling history, *Proc. Lunar Planet. Sci. Conf.*, 9, 3275-3283.

Brotchie, J. F. and R. Silvester (1969), On Crustal Flexure, *J. Geophys. Res.*, 74, 5240-5252.

Brown, S. M. and L. T. Elkins-Tanton (2009), Compositions of Mercury's earliest crust from magma ocean models, *Earth Planet. Sci. Let.*, 286, 446-455.

Budney, C. J. and P. G. Lucey (1998), Basalt thickness in Mare Humorum: The crater excavation method, *J. Geophys. Res.*, 103, 16,855-16,870.

Byrne, P. K., C. Klimczak, D.A. Williams, D. M. Hurwitz, S. C. Solomon, J. W. Head, F. Preusker, and J. Oberst (2013), An assemblage of lava flow features on Mercury, *J. Geophys. Res. Planets*, 118, 1303-1322, doi:10.1002/jgre.20052.

Cavanaugh, J. F., J. C. Smith, X. Sun, A. E. Bartels, L. Ramos-Izquierdo, D. J. Krebs, J. F. McGarry, R. Trunzo, A. M. Novo-Gradac, J. L. Britt, J. Karsh, R. B. Katz, A. T. Lukemire, R. Szymkiewicz, D. L. Berry, J. P. Swinski, G. A. Neumann, M. T. Zuber, and D. E. Smith (2007), The Mercury Laser Altimeter Instrument for the MESSENGER Mission, *Space Sci. Rev.*, 131, 451-479, doi: 10.1007/s11214-007-9273-4.

Chapman, C. R. (1988). Mercury: Introduction to an end-member planet. *Mercury*, 1-23.

Charlier, B., T. L. Grove, and M. T. Zuber (2013), Phase equilibria of ultramafic compositions on Mercury and the origin of the compositional dichotomy, *Earth and Planet. Sci. Let.*, 363, 50-60.

Dahlen, F. A. and F. J. Simons (2008), Spectral estimation on a sphere in geophysics and cosmology, *Geophys. J. Int.*, 174, 774-807, doi:10.1111/j.1365-246.

Denevi, B. W., M. S. Robinson, S. C. Solomon, S. L. Murchie, D. T. Blewett, D. L. Domingue, T. J. McCoy, C. M. Ernst, J. W. Head, T. R. Watters, and N. L. Chabot (2009), The Evolution of Mercury's Crust: A Global Perspective from MESSENGER, *Science*, 324, 613-618, doi:10.1126/science.1172226.

Denevi, B. W., C. M. Ernst, H. M. Meyer, M. S. Robinson, S. L. Murchie, J. L. Whitten, J. W. Head, T. R. Watters, S. C. Solomon, L. R. Ostrach, C. R. Chapman, P. K. Byrne, C. Klimczak, and P. N. Peplowski (2013), The distribution and origin of smooth plains on Mercury, *J. Geophys. Res. Planets*, 118, 891-907, doi:10.1002/jgre.20075.

Evans, A. J (2013), Ph.D. thesis, Massachusetts Institute of Technology.

Evans, L. G., P. N. Peplowski, E. A. Rhodes, D. J. Lawrence, T. J. McCoy, L. R. Nittler, S. C. Solomon, A. L. Sprague, K. R. Stockstill-Cahill, R. D. Starr, S. Z. Weider, W. V. Boynton, D. K. Hamara, and J. O. Goldsten (2012), Major-element abundances on the surface of Mercury: Results from the MESSENGER Gamma-Ray Spectrometer, *J. Geophys. Res.*, 117, E00L07, doi:10.1029/2012JE004178.

Fegley, B., Jr. (2004), Venus, Chapter 21. pp. 487-507, in: *Meteorites, Comets, and Planets* (ed. A.M. Davis) Vol. 1 *Treatise on Geochemistry* (Turekian, K.K. and Holland, H.D., eds.) Elsevier-Pergamon, Oxford.

Ford, P. G. and G. H. Pettengill (1992), Venus topography and kilometer-scale slopes, *J. Geophys. Res. 97*, 13,103-13,114.

Forsyth, D. W. (1985), Subsurface Loading and Estimates of the Flexural Rigidity of Continental Lithosphere, *J. Geophys. Res.*, 90, 12623-12632.

Freed, A. M., H. J. Melosh, and S. C. Solomon (2001), Tectonics of mascon loading: Resolution of the strike-slip paradox, *J. Geophys. Res.*, 106, E9, 20,603-20,620.

Freed, A. M. (2005), Earthquake Triggering by Static, Dynamic and Postseismic Stress Transfer, *Annu. Rev. Earth Planet Sci.*, 33, 335-367, doi:10.1146/annurev.earth.33.092203.122505.

Grimm, R. E. and S. C. Solomon (1988), Viscous relaxation of impact crater relief on Venus: constraints on crustal thickness and thermal gradient, *J. Geophys. Res.*, 93, 11911-11929.

Grimm, R. E. (1994), Recent deformation rates on Venus, *J. Geophys. Res.*, 99, 23163-23171.

Grimm, R. E. (1997), The Crust of Venus, pp. 1205-1244. In *Venus II: Geology, Geophysics, Atmosphere, and Solar Wind Environment* (ed. S.W. Bougher, D.M. Hunten, and R.J. Philips) Tucson, AZ : University of Arizona Press.

Hager, B. H. and R. W. Clayton (1989), Constraints on the structure of mantle convection using seismic observations, flow models, and the geoid, in: *Mantle Convection; plate tectonics and global dynamics*, R. W. Peltier (ed.), Gordon and Breach Science Publishers, New York, 657-763.

Haskell, N. A. (1936), The motion of a viscous fluid under a surface load, II, *Physics*, 7, 56-61.

Hauck, S. A., II. J.-L. Margot, S. C. Solomon, R. J. Phillips, C. L. Johnson, F. G. Lemoine, E. Mazarico, T. J. McCoy, S. Padovan, S. J. Peale, M. E. Perry, D. E. Smith, and M. T. Zuber (2013), The curious case of Mercury's internal structure, *J. Geophys. Res. Planets*, 118, doi:10.1002/jgre.20091.

Haxby, W. F. and D. L. Turcotte (1978), On isostatic geoid anomalies, *J. Geophys. Res.*, 83, 5473-5478.

Head, J. W. III (1976), Lunar Volcanism in Space and Time, *Rev. Geophys. Space Phys.*, 14, 265-300.

Head III, J. W., J. B. Adams, T. B. McCord, C. Pieters, and S. Zisk (1978), Regional stratigraphy and geologic history of Mare Crisium, in: *Mare Crisium*, the view from Luna 24, Merrill, R. B. and J. J. Papike, editors, Pergamon Press, NY, 43-74.

Head, J. W., C. R. Chapman, D. L. Domingue, S. E. Hawkins III, W. E. McClintock, S. L. Murchie, L. M. Prockter, M. S. Robinson, R. G. Strom, T. R. Watters (2007), The Geology of Mercury: The View Prior to the MESSENGER Mission, *Space Sci. Rev.*, 131, 41-84, doi:10.1007/s11214-007-9263-6.

Head, J. W., C. R. Chapman, R. G. Strom, C. I. Fassett, B. W. Denevi, D. T. Blewett, C. M. Ernst, T. R. Watters, S. C. Solomon, S. L. Muchie, L. M. Prockter, N. L. Chabot, J. J. Gillis-Davis, J. L. Whitten, T. A. Goudge, D. M. H. Baker, D. M. Hurwitz, L. R. Ostrach, Z. Xiao, W. J. Merline, L. Kerber, J. L. Dickson, J. Oberst, P. K. Byrne, C. Klimczak, and L. R. Nittler (2011), Flood Volcanism in the Northern High Latitudes of Mercury Revealed by MESSENGER, *Science*, 333, 1853-1856.

Herrick, R. R. and R. J. Phillips (1992), Geological correlations with the interior density structure of Venus, *J. Geophys. Res.*, 97, 16,017-16,034.

Herrick, R. R. (1994), The resurfacing history of Venus, *Geology*, 22, 703-706.

Hiesinger, H., J. W. Head III, U. Wolf, R. Jaumann, and G. Neukum (2002), Lunar mare basalt flow units: Thicknesses determined from crater size-frequency distributions, *Geophys. Res. Let.*, 29, doi:10.1029/2002GL014847.

Hiesinger, H., J. W. Head III, U. Wolf, R. Jaumann, and G. Neukum (2011), Ages and stratigraphy of lunar mare basalts: a synthesis, *GSA Special Papers*, 477, doi:10.1130/2011.2477(01).

Hikida, H. and M. A. Wieczorek (2007), Crustal thickness of the Moon: New constraints from gravity inversions using polyhedral shape models, *Icarus*, 192, 150-166.

Ito, K. and G. C. Kennedy (1971), An experimental study of the basalt-garnet granulite-eclogite transition, *Geophys. Mono.*, 14, 303-314.

Ivanov, M. A. and J. W. Head (1996), Tessera terrain on Venus: a survey of the global distribution, characteristics, and relation to the surrounding units from Magellan data, *J. Geophys. Res.*, 101, 14861-14908.

James, P. B., M. T. Zuber and R. J. Phillips (2013), Crustal thickness and support of topography on Venus, *J. Geophys. Res.*, 118, doi:10.1029/2012JE004237.

Jordan, T. H. (1978), Composition and development of the continental tectosphere, *Nature*, 274, 544-548.

Kamalakar, J. A., K. V. S. Bhaskar, A. S. Laxmi Prasad, R. Ranjith, K. A. Lohar, R. Venketeswaran, and T. K. Alex (2005), Lunar ranging instrument for Chandrayaan-1, *J. Earth Syst. Sci.*, 114, 725-731.

Kaula, W. K. (1966), *Theory of Satellite Geodesy*, 124 pp., Blaidsel, Waltham, MA.

Kaula, W. M., G. Schubert, R. E. Lingenfelter, W. L. Sjogren, and W. R. Wollenhaupt (1974), Apollo laser altimetry and inferences as to lunar structure, *Proc. Fifth Lunar Conference*, 3, 3049-3058.

Kaula, W. K., and R. J. Phillips (1981), Quantitative Tests for Plate Tectonics on Venus, *Geophys. Res. Let.*, 8, 1187-1190.

Kiefer, W. S., and B. H. Hager (1991), A mantle plume model for the equatorial highlands of Venus, *J. Geophys. Res.*, 96, 20947-20966.

King, S. D. (2008), Pattern of lobate scarps on Mercury's surface reproduced by a model of mantle convection, *Nature Geoscience*, 1, 229-232, doi:10.1038/ngeo152.

Klimczak, C., T. R. Watters, C. M. Ernst, A. M. Freed, P. K. Byrne, S. C. Solomon, D. M. Blair, and J. W. Head (2012), Deformation associated with ghost craters and basins in volcanic smooth plains on Mercury: Strain analysis and implications for plains evolution, *J. Geophys. Res.*, 117, E00L03, doi:10.1029/2012JE004100.

Kohlstedt, D. L., B. Evans, and S. J. Mackwell (1995), Strength of the lithosphere: Constraints imposed by laboratory experiments, *J. Geophys. Res.*, 100, B9, 17,587-17,602.

Konopliv, A. S., W. B. Banerdt, and W. L. Sjogren (1999), Venus gravity: 180th degree and order model, *Icarus*, 139, 3-18.

Konopliv, A. S., S. W. Asmar, E. Carranza, W. L. Sjogren, and D. N. Yuan (2001), Recent Gravity Models as a Result of the Lunar Prospector Mission, *Icarus*, 150, 1-18, doi:10.1006/icar.2000.6573.

Kucinskas, A. B. and D. L. Turcotte (1994), Isostatic compensation of equatorial highlands on Venus, *Icarus*, 112, Issue 1, 104-116.

Kucinskas, A. B., D. L. Turcotte and J. Arkani-Hamed (1996), Isostatic compensation of Ishtar Terra, Venus, *J. Geophys. Res.*, 101, 4725-4736.

Lambeck, K. (1976), Lateral density anomalies in the upper mantle, *J. Geophys. Res.*, 81, 6333-6340.

Lemoine, F. G. R., D. E. Smith, M. T. Zuber, G. A. Neumann, and D. D. Rowlands (1997), A 70th degree lunar gravity model (GLGM-2) from Clementine and other tracking data, *J. Geophys. Res.*, 102, E7, 16,339-16,359.

Lemoine, F. G., S. Goossens, T. J. Sabaka, J. B. Nicholas, E. Mazarico, D. D. Rowlands, B. D. Loomis, D. S. Chinn, D. S. Caprette, G. A. Neumann, D. E. Smith, and M. T. Zuber (2013), High-degree gravity models from GRAIL primary mission data, *J. Geophys. Res.*, 118, 1676-1698, doi:10.1002/jgre.20118.

Li, C., X. Ren, J. Liu, X. Zou, L. Mu, J. Wang, R. Shu, Y. Zou, H. Zhang, C. Lu, J. Liu, W. Zuo, Y. Su, W. Wen, W. Bian, M. Wang, C. Xu, D. Kong, X, Wang, F. Want, L. Geng, Z. Zhang, L. Zheng, X. Zhu, J. Li, and Z. Ouyang (2010), Laser altimetry data of Chang'E-1 and the global lunar DEM model, *Science China Earth Sci.*, 53, 1582-1593, doi:10.1007/s11430-010-4020-1.

Lorell, J. and W. L. Sjogren (1968), Lunar Gravity: Preliminary Estimates from Lunar Orbiter, *Science*, 159, 625-627.

Mackwell, S. J., M. E. Zimmerman and D. L. Kohlstedt (1998), High-temperature deformation of dry diabase with application to tectonics on Venus, *J. Geophys. Res.*, 103, 975-984.

Margot, J. L., S. J. Peale, R. F. Jurgens, M. A. Slade, and I. V. Holin (2007), Large Longitude Libration of Mercury Reveals a Molten Core, *Science*, 316, 710-714.

Margot, J.-L., S. J. Peale, S. C. Solomon, S. A. Hauck II, F. D. Ghigo, R. F. Jurgens, M. Yseboodt, J. D. Giorgini, S. Padovan, and D. B. Campbell (2012), Mercury's moment of inertia from spin and gravity data, *J. Geophys. Res.*, 117, E00L09, doi:10.1029/2012JE004161.

Matsumoto, K., S. Goossens, Y. Ishihara, Q. Liu, F. Kikuchi, T. Iwata, N. Namiki, H. Noda, H. Hanada, N. Kawano, F. G. Lemoine, and D. D. Rowlands (2010), An improved lunar gravity field model from SELENE and historical tracking data: Revealing the farside gravity features, *J. Geophys. Res.*, 115, E06007, doi:10.1029/2009JE003499.

Maxwell, T. A., F. El-Baz, S. H. Ward (1975), Distribution, Morphology, and Origin of Ridges and Arches in Mare Serenitatis, *GSA Bulletin*, 86, 1273-1278.

Mazarico, E., D. D. Rowlands, G. A. Neumann, D. E. Smith, M. H. Torrence, F. G. Lemoine, and M. T. Zuber (2012), Orbit determination of the Lunar Reconnaissance Orbiter, *J. Geod.*, 86, 193-207.

McGovern, P. J., S. C. Solomon, D. E. Smith, M. T. Zuber, M. Simons, M. A. Wieczorek, R. J. Phillips, G. A. Neumann, O. Aharonson, and J. W. Head (2002), Localized gravity/topography admittance and correlation spectra on Mars: Implications for regional and global evolution, *J. Geophys. Res.*, 107, 5136, doi:10.1029/2002JE001854.

McKenzie, D., P. G. Ford, C. Johnson, B. Parsons, D. Sandwell, S. Saunders, and S. C. Solomon (1992), Features on Venus Generated by Plate Boundary Processes, *J. Geophys. Res.*, 97, 13533-13544.

McKenzie, D. (1994), The relationship between topography and gravity on Earth and Venus, *Icarus*, 112, 55-88.

McKenzie, D. and F. Nimmo (1997), Elastic Thickness Estimates for Venus from Line of Sight Accelerations, *Icarus*, 130, 198-216.

McKenzie, D. (2003), Estimating T_e in the presence of internal loads, *J. Geophys. Res.*, 108, 2438-2458, doi:10.1029/2002JB001766.

McNutt, M. K. (1984), Lithospheric Flexure and Thermal Anomalies, *J. Geophys. Res.*, 89, 11180-11194.

Melosh, H. J., A. M. Freed, B. C. Johnson, D. M. Blair, J. C. Andrews-Hanna, G. A. Neumann, R. J. Phillips, D. E. Smith, S. C. Solomon, M. A. Wieczorek, M. T. Zuber (2013), The Origin of Lunar Mascon Basins, *Science*, 340, 1552-1555, doi:10.1126/science.1235768.

Metzger, A. E., J. I. Trombka, R. C. Reedy, and J. R. Arnold (1974), Element concentrations from lunar orbital gamma-ray measurements, *Proc. of the Fifth Lunar Conf.*, 2, 1067-1078.

Michel, N. C., S. A. Hauck II, S. C. Solomon, R. J. Phillips, J. H. Roberts, and M. T. Zuber (2013), Thermal evolution of Mercury as constrained by MESSENGER observations, *J. Geophys. Res. Planets*, 118, 1033-1044, doi:10.1002/jgre.20049.

Muller, P. M. and W. L. Sjogren (1968), Lunar Mass Concentrations, *Science*, 161, 680-684

Murchie, S. L., T. R. Watters, M. S. Robinson, J. W. Head, R. G. Strom, C. R. Chapman, S. C. Solomon, W. E. McClintock, L. M. Prockter, D. L. Domingue, and D. T. Blewett (2008), Geology of the Caloris Basin, Mercury, A View from MESSENGER, *Science*, 321, 73-76, doi: 10.1126/science.1159261.

Namiki, N. and S. C. Solomon (1993), The gabbro-eclogite phase transition and the elevation of mountain belts on Venus, *J. Geophys. Res.*, 98, 15025-15031.

Namiki, N., T. Iwata, K. Matsumoto, H. Hanada, H. Noda, S. Goossens, M. Ogawa, N. Kawano, K. Asari, S. Tsuruta, Y. Ishihara, Q. Liu, F. Kikuchi, T. Ishikawa, S. Sasaki, C. Aoshima, K. Kurosawa, S. Sugita, and T. Takano (2009), Farside Gravity Field of the Moon from Four-Way Doppler Measurements of SELENE (Kaguya), *Science*, 323, 900-905.

Neumann, G. A., M. T. Zuber, D. E. Smith, and F. G. Lemoine (1996), The lunar crust: Global structure and signature of major basins, *J. Geophys. Res.*, 101, 16841-16843.

Neumann, G. A., M. T. Zuber, M. A. Wieczorek, P. J. McGovern, F. G. Lemoine and D. E. Smith (2004), Crustal structure of Mars from gravity and topography, *J. Geophys. Res.*, 109, E08002, doi:10/1029/2004JE002262.

Neumann, G. A., M. T. Zuber, D. E. Smith, M. A. Wieczorek, J. W. Head, D. M. H. Baker, F. G. Lemoine, T. J. Sabaka, E. Mazarico, S. Goossens, S. C. Solomon, H. J. Melosh, R. J. Phillips, S. W. Asmar, A. S. Konopliv, J. G. Williams, M. M. Sori, K. Miljkovic, and J. C. Andrews-Hanna (2013), Lunar Impact Basins Revealed by the Gravity Recovery and Interior Laboratory (GRAIL) Mission, in prep.

Nittler, L. R., R. D. Starr, S. Z. Weider, T. J. McCoy, W. V. Boynton, D. S. Ebel, C. M. Ernst, L. G. Evans, J. O. Goldsten, D. K. Hamara, D. J. Lawrence, R. L. McNutt Jr., C. E. Schlemm II, S. C. Solomon, and A. L. Sprague (2011), The Major-Element Composition of Mercury's Surface from MESSENGER X-ray Spectrometer, *Science*, 333, 1847-1850, doi:10.1126/science.1211567.

Oberst, J., F. Preusker, R. J. Phillips, T. R. Watters, J. W. Head, M. T. Zuber, S. C. Solomon (2010), The morphology of Mercury's Caloris basin, as seen in MESSENGER stereo topographic models, *Icarus*, 209, 230-238.

Okada, Y. (1985), Surface deformation due to shear and tensile faults in a half-space, *Bulletin of the Seismological Society of America*, 75, 1135-1154.

Ono, T., A. Kumamoto, H. Nakagawa, Y. Yamaguchi, S. Oshigami, A. Yamaji, T. Kobayashi, Y. Kasahara, and H. Oya (2009), Lunar Radar Sounder Observations of Subsurface Maria of the Moon, *Science*, 323, 909-912.

Pauer, M., K. Fleming, and O. Čadek (2006), Modeling the dynamic component of the geoid and topography of Venus, *J. Geophys. Res.*, 111, E11012, doi:10.1029/2005JE002511

Peeples, W. J., W. R. Sill, T. W. May, S. H. Ward, R. J. Phillips, R. L. Jordan, E. A. Abbott, and T. J. Killpack (1978), Orbital Radar Evidence for Lunar Subsurface Layering in Maria Serenitatis and Crisium, *J. Geophys. Res.*, 83, 3459-3468.

Peplowski, P. N., E. A. Rhodes, D. K. Hamara, D. J. Lawrence, L. G. Evans, L. R. Nittler, and S. C. Solomon (2012), Aluminum abundance on the surface of Mercury: Application of a new background-reduction technique for the analysis of gamma-ray spectroscopy data, *J. Geophys. Res.*, 117, E00L10, doi:10.1029/2012JE004181.

Pettengill, G. H., P. G. Ford, W. T. K. Johnson, R. K. Raney and L. A. Soderblom (1991), Magellan: radar performance and data products, *Science*, 252, 260-265.

Pettengill, G. H., P. G. Ford and R. J. Wilt (1992), Venus surface radiothermal emission as observed by Magellan, *J. Geophys. Res.*, 97, 13091-13102.

Phillips, R. J., G. F. Adams, W. E. Brown Jr., R. E. Eggleton, P. Jackson, R. Jordan, W. J. Peeples, L. J. Porcello, J. Ryu, G. Schaber, W. R. Sill, T. W. Thompson, S. H. Ward, and J. S. Zelenka (1973), The Apollo 17 Lunar Sounder, *Proc. Fourth Lunar Sci. Conf.*, 3, 2821-2831.

Phillips, R. J. (1986), A mechanism for tectonic deformation on Venus, *Geophys. Res. Let.*, 13, 1141-1144.

Phillips, R. J., N. H. Sleep and W. B. Banerdt (1990), Permanent uplift in magmatic systems with application to the Tharsis region of Mars, *J. Geophys. Res.*, 95, 5089-5100.

Phillips, R. J., and V. L. Hansen (1994), Tectonic and magmatic evolution of Venus, *Annu. Rev. Earth Planet. Sci.*, 22, 597-654.

Phillips, R. J. and V. L. Hansen (1998), Geological evolution of Venus: rises, plains, plumes, and plateaus, *Science*, 279, 1492-1497.

Richards, M. A. and B. H. Hager (1984), Geoid anomalies in a dynamic Earth, *J. Geophys. Res.*, 89, 5987-6002.

Rudnick, R.L. and G. Gao (2005), Venus, Chapter 21. pp. 1-64, in: *Meteorites, Comets, and Planets* (e.d. R.L. Rudnick) Vol. 1 Treatise on Geochemistry (ed. K.K. Turekian and H.D. Holland) Elsevier-Pergamon, Oxford.

Sandwell, D. T. and G. Schubert (1992), Flexural Ridges, Trenches, and Outer Rises Around Coronae on Venus, *J. Geophys. Res.*, 97, 16069-16083.

Santo, A. G., R. E. Gold, R. L. McNutt, Jr., S. C. Solomon, C. J. Ercol, R. W. Farquhar, T. J. Hartka, J. E. Jenkins, J. V. McAdams, L. E. Mosher, D. F. Persons, D. A. Artis, R. S. Bokulic, R. F. Conde, G. Dakermanji, M. E. Goss, Jr., D. R. Haley, K. J. Heeres, R. H. Maurer, R. C. Moore, E. H. Rodberg, T. G. Stern, S. R. Wiley, B. G. Williams, C. L. Yen, M. R. Peterson (2001), The MESSENGER mission to Mercury: spacecraft and mission design, *Planet. Space Sci.*, 49, 1481-1500.

Schubert G., D. Bercovici, and G. A. Glatzmaier (1990), Mantle dynamics in Mars and Venus: influence of an immobile lithosphere on three-dimensional mantle convection, *J. Geophys. Res.*, 95, 14105-14129.

Sharpton, V. L. and J. W. Head III (1982), Stratigraphy and Structural Evolution of Southern Mare Serenitatis: A Reinterpretation Based on Apollo Lunar Sounder Experiment Data, *J. Geophys. Res.*, 87, B13, 10,983-10,998.

Simons, M., B. H. Hager and S. C. Solomon (1994), Global variations in the geoid/topography admittance of Venus, *Science*, 264, 799-803.

Simons, M., B. H. Hager and S. C. Solomon (1997), Localization of gravity and topography: constraints on the tectonics and mantle dynamics of Venus, *Geophys. J. Int.*, 131, 24-44.

Sjogren, W. L. and W. R. Wollenhaupt (1973), Lunar Shape via the Apollo Laser Altimeter, *Science*, 179, 275-278.

Sjogren, W. L., R. N. Wimberly, and W. R. Wollenhaupt (1974), Lunar gravity via the Apollo 15 and 16 subsattelites, in: *The Moon*, 9, pp. 115-128.

Smith, D. E., M. T. Zuber, S. C. Solomon, R. J. Phillips, J. W. Head, J. B. Garvin, W. B. Banerdt, D. O. Muhleman, G. H. Pettengill, G. A. Neumann, F. G. Lemoine, J. B. Abshire, O. Aharonson, C. D. Brown, S. A. Hauck, A. B. Ivanov, P. J. McGovern, H. J. Zwally, T. C. Duxbury (1999), The Global Topography of Mars and Implications for Surface Evolution, *Science*, 284, 1495-1503.

Smith, D.E., M. T. Zuber, G. A. Neumann, F. G. Lemoine, E. Mazarico, M. H. Torrence, J. F. McGarry, D. D. Rowlands, J. W. Head III, T. H. Duxbury, O. Aharonson, P. G. Lucey, M. S. Robinson, O. S. Barnouin, J. F. Cavanaugh, X. Sun, P. Liiva, D. Mao, J. C. Smith, and A. E. Bartels (2010), Initial observations from the Lunar Orbiter Laser Altimeter (LOLA). *Geophys. Res. Lett.*, 37, L18204, doi:10.1029/2010GL043751.

Smith, D. E., M. T. Zuber, G. B. Jackson, J. F. Cavanaugh, G. A. Neumann, H. Riris, X. Sun, R. S. Zellar, C. Coltharp, J. Connelly, R. B. Katz, I. Kleyner, P. Liiva, A. Matuszeski, E. M. Mazarico, J. F. McGarry, A.-M. Novo-Gradac, M. N. Ott, C. Peters, L. A. Ramos-Izquierdo, L. Ramsey, D. D. Rowlands, S. Schmidt, V. S. Scott III, G. B. Shaw, J. C. Smith, J.-P. Swinski, M. H. Torrence, G. Unger, A. W. Yu, and T. W. Zagwodzki (2010), The Lunar Orbiter Laser Altimeter Investigation on the Lunar Reconnaissance Orbiter Mission, *Space Sci. Rev.*, 150, 209-241, doi:10.1007/s11214-009-9512-y.

Smith, D.E., M.T. Zuber, R.J. Phillips, S.C. Solomon, S.A. Hauck, II, F.G. Lemoine, E. Mazarico, G.A. Neumann, S.J. Peale, J.-L. Margot, C.L. Johnson, M.H. Torrence, M.E. Perry, D.D. Rowlands, S. Goossens, A.H. Taylor, Gravity field and internal structure of Mercury from MESSENGER *Science*, 335, doi:10.1126/science.1218809, 2012.

Smrekar, S. E. and R. J. Phillips (1991), Venusian Highlands: Geoid to topography ratios and their implications, *Earth Planet. Sci. Let.*, 107, 582-597.

Smrekar, S. E., E. R. Stofan, N. Mueller, A. Treiman, L. Elkins-Tanton, J. Helbert, G. Piccioni, P. Drossart (2010), Recent hotspot volcanism on Venus from VIRTIS emissivity data, *Science*, 328, 605-608.

Solomon, S. C. (1976), Some Aspects of Core Formation in Mercury, *Icarus*, 28, 509-521.

Solomon, S. C. (1977), The Relationship between Crustal Tectonics and Internal Evolution in the Moon and Mercury, *Phys. Earth Planet. Int.*, 15, 135-145.

Solomon, S. C. and J. W. Head (1979), Vertical Movement in Mare Basins: Relation to Mare Emplacement, Basin Tectonics, and Lunar Thermal History, *J. Geophys. Res.*, 84, 1667-1682.

Solomon, S. C. and J. W. Head (1980), Lunar Mascon Basins: Lava Filling, Tectonics, and Evolution of the Lithosphere, *Rev. Geophys. Space Phys.*, 18, 107-141.

Solomon, S. C., R. P. Comer, and J. W. Head (1982), The Evolution of Impact Basins: Viscous Relaxation of Topographic Relief, *J. Geophys. Res.*, 97, 3975-3992.

Solomon, S. C., S. E. Smrekar, D. L. Bindschadler, R. E. Grimm, W. M. Kaula, G. E. McGill, R. J. Phillips, R. S. Saunders, G. Schubert, S. W. Squires, and E. R. Stofan (1992), Venus Tectonics: An Overview of Magellan Observations, *J. Geophys. Res.*, 97, 13199-13255.

Spudis, P. D. and J. E. Guest (1988), Stratigraphy and geologic history of Mercury, in: *Mercury*, edited by F. Vilas, C. R. Chapman, M. S. Matthews, pp. 118-164, Univ. of Ariz. Press, Tucson.

Srinivasan, D. K., M. E. Perry, K. B. Fielhauer, D. E. Smith, and M. T. Zuber (2007), The Radio Frequency Subsystem and Radio Science on the MESSENGER Mission, *Space Sci. Rev.*, 131, 557-571, doi: 10.1007/s11214-007-9270-7.

Stein, R. S., A. A. Barka, and J. H. Dieterich (1997), Progressive failure on the North Anatolian fault since 1939 by earthquake stress triggering, *Geophys. J. Int.*, 128, 594-604.

Stein, R. S. (1999), The role of stress transfer in earthquake occurrence, *Nature*, 402, 605-609.

Surkov, Y. A., V. L. Barsukov, L. P. Moskalyeva, V. P. Kharyukova, and A. L. Kemurdzhian (1984), New data on the composition, structure, and properties of Venus rock obtained by Venera 13 and Venera 14, *J. Geophys. Res.*, 89, B393-B402.

Thomson, B. J., E. B. Grosfils, D. Ben J. Bussey, and P. D. Spudis (2009), A new technique for estimating the thickness of mare basalts in Imbrium Basin, *Geophys. Res. Lett.*, 36, L12201, doi:10.1029/2009GL037600.

Turcotte, D.L., R. J. Willemann, W. F. Haxby, and J. Norberry (1981), Role of membrane stresses in the support of planetary topography, *J. Geophys. Res.*, 86, 3951-3959.

Turcotte, D. L. (1987), A fractal interpretation of topography and geoid spectra on the Earth, Moon, Venus, and Mars, *J. Geophys. Res.*, 92, E597-E601.

Turcotte, D. L. and G. Schubert (2002), *Geodynamics*, Cambridge University Press.

Turkevich, A. L. (1973), The Chemical Composition of the Lunar Surface, *Accounts of Chemical Res.*, 6, 81-89.

Watters, W. A. F., M. T. Zuber and B. H. Hager (2009), Thermal perturbations caused by large impacts and consequences for mantle convection, *J. Geophys. Res.*, 114, E02001, doi:10.1029/2007JE002964.

Watters, T. R. and C. L. Johnson (2010), Lunar tectonics, Chapter 4, pp. 121-182, in: *Planetary Tectonics*, T. R. Watters and R. A. Schultz, editors, Cambridge University Press, Cambridge, UK.

Watters, T. R., M. S. Robinson, M. E. Banks, T. Tran, and B. W. Denevi (2012), Recent extensional tectonics on the Moon revealed by the Lunar Reconnaissance Orbiter Camera, *Nature Geoscience*, doi:10.1038/NGEO1387.

Watts, A. B. (2001), *Isostasy and Flexure of the Lithosphere*, Cambridge Univ. Press, Cambridge, UK.

Weider, S. Z., L. R. Nittler, R. D. Starr, T. J. McCoy, K. R. Stockstill-Cahill, P. K. Byrne, B. W. Denevi, J. W. Head, and S. C. Solomon (2012), Chemical heterogeneity on Mercury's surface revealed by the MESSENGER X-Ray Spectrometer, *J. Geophys. Res.*, 117, E00L05, doi:10.1029/2012JE004153.

Weider S. Z. and L. R. Nittler (2013), The Surface Composition of Mercury as Seen From MESSENGER, *CosmoELEMENTS*, April 2013, 90-91.

Wieczorek, M. A. and R. J. Phillips (1997), The structure and compensation of the Lunar highland crust, *J. Geophys. Res.*, 102, 10933-10943.

Wieczorek, M. A. and R. J. Phillips (1998), Potential anomalies on a sphere: applications to the thickness of the Lunar crust, *J. Geophys. Res.*, 103, 1715-1724.

Wieczorek, M. A., M. T. Zuber, and R. J. Phillips (2001), The role of magma buoyancy on the eruption of lunar basalts, *EPSL*, 185, 71-83.

Wieczorek, M. A. and M. T. Zuber (2004), Thickness of the Martian crust: Improved constraints from geoid-to-topography ratios, *J. Geophys. Res.*, 109, E01009, doi:10.1029/2003JE002153.

Wieczorek, M. A. (2007), Gravity and topography of the terrestrial planets, *Treatise on Geophysics*, 10, 1650208, doi:10.1016/B978-044452748-6/00156-5.

Wieczorek, M. A. and F. J. Simons (2007), Minimum Variance Multitaper Spectral Estimation on the Sphere, *Journal of Fourier Analysis and Applications*, 13, 665-692.

Wieczorek, M. A., G. A. Neumann, F. Nimmo, W. S. Kiefer, G. J. Taylor, H. J. Melosh, R. J. Phillips, S. C. Solomon, J. C. Andrews-Hanna, S. W. Asmar, A. S. Konopliv, F. G. Lemoine, D. E. Smith, M. M. Watkins, J. G. Williams, and M. T. Zuber (2013), The Crust of the Moon as Seen by GRAIL, *Science*, 338, 671-675, doi:10.1126/science.1231530.

Wilhelms, D. E., and J. F. McCauley (1971), Geologic map of the near side of the Moon, US Geological Survey, Flagstaff, AZ.

Wilhelms, D. E. (1987), The Geologic History of the Moon, U.S. Geol. Surv. Spec. Pap. 1348, 302 pp.

Wood, J. A., J. S. Dickey, Jr., U. B. Marvin, and B. N. Powell (1970), Lunar anorthosites and a geophysical model of the moon, *Proc. of the Apollo 11 Lunar Sci. Conf.*, 1, 965-988.

Zuber, M. T. (1987), Constraints on the lithospheric structure of Venus from mechanical models and tectonic surface features, *J. Geophys. Res.*, 92, E541-E551.

Zuber, M. T., D. E. Smith, F. G. Lemoine and G. A. Neumann (1994), The shape and internal structure of the Moon from the Clementine mission, *Science*, 266, 1839-1843.

Zuber, M. T., S. C. Solomon, R. J. Phillips, D. E. Smith, G. L. Tyler, O. Aharonson, G. Balmino, W. B. Banerdt, J. W. Head, F. G. Lemoine, P. J. McGovern, G. A. Neumann, D. D. Rowlands and S. Zhong (2000), Internal structure and early thermal evolution of Mars from Mars Global Surveyor topography and gravity, *Science*, 287, 1788-1793.

Zuber, M. T., D. E. Smith, R. J. Phillips, S. C. Solomon, G. A. Neumann, S. A. Hauck, II, S. J. Peale, O. S. Barnouin, J. W. Head, C. L. Johnson, F. G. Lemoine, E. Mazarico, X. Sun, M. H. Torrence, A. M. Freed, C. Klimczak, J.-L. Margot, J. Oberst, M. E. Perry, R. L. McNutt, Jr., J. A. Balcerski, N. Michel, M. J. Talpe and D. Yang (2012), Topography of the northern hemisphere of Mercury from MESSENGER laser altimetry, *Science*, 335, 217-220, doi:10.1126/science.1218805.

Zuber, M. T., D. E. Smith, M. W. Watkins, S. W. Asmar, A. S. Konopliv, F. G. Lemoine, H. J. Melosh, G. A. Neumann, R. J. Phillips, S. C. Solomon, M. A. Wieczorek, J. G. Williams, S. J. Goossens, G. Kruizinga, E. Mazarico, R. S. Park, D.-N. Yuan (2013), Gravity Field of the Moon from the Gravity Recovery and Interior Laboratory (GRAIL) Mission, *Science*, 339, 668-671, doi:10.1126/science.1231507.

Zuber, M., D. Smith, D. Lehman, T. Hoffman, S. Asmar, and M. Watkins (2013), Gravity Recovery and Interior Laboratory (GRAIL): Mapping the lunar interior from crust to core, *Space Sci. Rev.*, 1-22, doi:10.1007/s11214-012-9952-7.